

# Early Stages of Zeolite Growth

A DISSERTATION  
SUBMITTED TO THE FACULTY OF THE GRADUATE SCHOOL  
OF THE UNIVERSITY OF MINNESOTA  
BY

Sandeep Kumar

IN PARTIAL FULFILLMENT OF THE REQUIREMENTS  
FOR THE DEGREE OF  
DOCTOR OF PHILOSOPHY

Professor Michael Tsapatsis, Adviser; Professor Lee Penn, Co-Adviser

August 2010

© Sandeep Kumar 2010

## Acknowledgements

I would like to extend my sincere appreciation to Professors Michael Tsapatsis and Lee Penn for their guidance and support. I have been deeply indebted to them for the opportunity to work in their research groups. I would also like to thank Professors Andreas Stein and Alon McCormick for reading my dissertation, and Professor Frank S Bates for serving on my final examining committee. I want to express my gratitude to all of those who supported me in any respect during the completion of the graduate degree.

## **Dedication**

This dissertation is dedicated to my parents.

## Abstract

Zeolites are crystalline nonporous aluminosilicates with important applications in separation, purification, and adsorption of liquid and gaseous molecules. However, an ability to tailor the zeolite microstructure, such as particle size/shape and pore-size, to make it benign for specific application requires control over nucleation and particle growth processes. But, the nucleation and crystallization mechanisms of zeolites are not fully understood.

In this context, the synthesis of an all-silica zeolite with MFI-type framework has been studied extensively as a model system. Throughout chapters 2, 4 and 5, MFI growth process has been investigated by small-angle x-ray scattering (SAXS) and transmission electron microscopy (TEM). Of fundamental importance is the role of nanoparticles ( $\sim 5$  nm), which are present in the precursor sol, in MFI nucleation and crystallization. Formation of amorphous aggregates and their internal restructuring are concluded as essential steps in MFI nucleation. Early stage zeolite particles have disordered and less crystalline regions within, which indicates the role of structurally distributed population of nanoparticles in growth. Faceting occurs after the depletion of nanoparticles. The chapter 6 presents growth studies in silica sols prepared by using a dimer of tertaprylpylammonium (TPA) and reports that MFI nucleation and crystallization are delayed with a more pronounced delay in crystal growth.

## Table of Contents

List of Figures.....	v
Chapter 1: Background.....	1
Chapter 2: Aggregative Growth of MFI.....	11
Chapter 3: High-Resolution Cryo-TEM of Nanozeolites.....	29
Chapter 4: A Structural Resolution Cryo-TEM Study of the Early Stages of MFI Growth .....	41
Chapter 5: MFI Nucleation and Crystallization in Silica Sols.....	51
Chapter 6: MFI Growth by Using Monomers and Dimers of TPAOH.....	64
Chapter 7: Concluding Remarks.....	80
Bibliography.....	83
Appendix A: Defects in dC5-MFI.....	88
Appendix B: Other Work Done at the University of Minnesota.....	93

## List of Figures

Figure 1.1: Schematic representation of MFI framework structure.....	2
Figure 1.2: Silica solubility limit as a function of pH based on the prediction by Rimer et al. The prediction is based on experiments with TPA-silica-water systems.....	4
Figure 1.3: Clear sol compositions considered in previous reports and those in the present study.....	5
Figure 1.4: (a) SAXS and SANS data for the solution with molar composition 20SiO <sub>2</sub> :9TPAOH:9500H <sub>2</sub> O with PDDFs in (b). (c) A schematic showing silica-core/TPA-shell structure of PNs.....	6
Figure 1.5: Schematic illustration of the mechanism proposed for nanoparticles evolution and crystal growth by aggregation. An HRTEM image of MFI crystal oriented along b-axis is shown (reproduced from the published report). MFI crystal comprises of two slightly misoriented domains (indicated by two arrows). A set of parallel lines are drawn to illustrate this misorientation between two domains.....	8
Figure 2.1: (a) Simulated HRTEM images along a-, b- and c-axis, respectively. The crystal structure of MFI is also overlapped for clarity of contrast in simulated images. The diffraction patterns for each zone axes are shown below each simulated image. Images are simulated at Scherzer defocus ( $\Delta f_{Sch} = 62$ nm) and sample thickness ~5 nm. (b) thickness-defocus map for MFI along straight channels (b-axis). Each unit cell (~2 nm along b-axis) was divided into 8 slices. (c) An experimental HRTEM image of a MFI crystal oriented along b-axis revealing 10MR straight channels surrounded by two 6MR and eight 5MR. This MFI crystal was grown using dC5 (dimer of TPA with 5 carbons linked in-between) as SDA. All simulation results are for 300 kV Tecnai F 30 ( $C_s = 1.2$ mm).....	14
Figure 2.2: (a) SAXS Measurements from M1 with increasing time steps: immediately after TEOS hydrolysis (t1), after 30 days at room temperature (t2), and 30 days at room temperature followed by 2 h (t3), 3 h (t4), and 6 h at 90 °C (t5). The onset of secondary particle formation in M1 is shown to occur during the first 2 h at 90 °C. (b) M1 prior to aging was also characterized by cryo-TEM.....	18
Figure 2.3: HRTEM images of MFI crystals from sol heat-treated for 52 h at 90 °C. Rounded protrusions of approximately 5 nm size are shown by arrowheads in (a) and (c). (d) A schematic of characteristic hexagonal-prismatic morphology of TPA-MFI.....	19
Figure 2.4: A HRTEM image of MFI crystal with FFT inset of sol heat-treated for 52 h at 90 °C.....	20
Figure 2.5: HRTEM images ((a) and (b)) of the first evidence of crystallinity in sol after heat-treatment for 2 h at 90 °C. MFI crystals in (a) is oriented either along a- or b-axis whereas it is tilted away from the major zone axis in (b); FFTs are shown in insets. TEM images are reproduced on the right; white lines serve to highlight the crystal perimeter.....	22
Figure 2.6: HRTEM images of MFI crystals present in sol after heat-treatment for 3 h at 90 °C; FFTs are shown in insets. Crystal in (a) is oriented along [111]-axis while it is oriented either along a- or b-axis in (b) .....	23
Figure 2.7: HRTEM images showing MFI crystals formed after heat treatment for 6 h at 90 °C. ....	24
Figure 2.8: HRTEM images of MFI crystals present in sol after heat treatment for 6 h at 90 °C; FFTs are shown in insets.....	24
Figure 2.9: HRTEM images showing intergrown MFI crystals present in sol after heat-treatment for 52 h at 90 °C. Pairs of white arrows show the crystallographic orientation of the two regions. ....	26

Figure 3.1: A representative cryo-TEM image of a MFI crystallite embedded in vitreous TPA-silica sol aged for 242 days (pH~ 11.5). Dot-like contrast is due to the presence of precursor nanoparticles. Magnified image of the crystallite is shown in bottom-right and FFT is shown in the top-right.....	33
Figure 3.2: (a) A representative cryo-TEM image of 14×18 nm sized MFI crystal. Spots in inset FFT correspond to 11 Å. (b) Cryo-TEM image indicating MFI particles to be single-crystalline.....	34
Figure 3.3: A representative cryo-TEM image of sample A with inset FFT is shown. The first ring of spots corresponds to $d_{hkl} \sim 3.7\text{--}3.9$ Å. The spots marked as M and N correspond to 2.6 and 2.2 Å, respectively.....	36
Figure 3.4: (a) A cryo-TEM image with (b) FFT of sample B. (c) Crystallization of hexagonal ice occurs after about 500 s, which then propagates very fast as shown in (e). FFT corresponding to (c) and (e) are shown in (d) and (f), respectively.....	37
Figure 3.5: Cryo-TEM image of sample C was acquired after the exposure to the electron beam for ~8 minutes. Two features noted as 1 and 2 are further shown in (b) and (c). Image with FFT inset in (b) shows a [0001]-oriented single-crystalline $I_h$ . A square area is magnified to reveal $\{10\bar{1}0\}$ -type lattice fringes. The central part of the region 2 is magnified in (c); two sets of $\{10\bar{1}0\}$ -type planes intersect each other at 40°.....	38
Figure 3.6: A cryo-TEM image of sample D with a square region magnified in the bottom. The FFT inset from the square region consist a ring of spots corresponding to 3.7 Å. There is a set of spots (marked by P) which may correspond to MFI-type framework (d-spacing ~9.6 Å). .....	39
Figure 4.1: SAXS scattering profiles from TPA-silica sols after various times at room temperature.....	45
Figure 4.2: (a) A representative cryo-TEM image of the sol kept for 200 days at room temperature. A magnified image of a representative aggregate with FFT inset is shown in (b). (c) A cryo-TEM image of sol after 220 days; a high-resolution cryo-TEM image of a representative crystal with FFT inset is shown in (d). A cryo-TEM image of dialyzed sol after 220 days is shown in (e). A conventional (non-cryogenic) TEM image of a dry crystal isolated from the dialyzed sol is shown in (f) .....	47
Figure 4.3: SAXS patterns from the original and dialyzed sols after 220 days at room temperature. ....	49
Figure 5.1: TEM image of the materials obtained on a TEM grid by depositing from (a) TPA-silica sol and (b) the same sol after the dialysis procedure. ....	52
Figure 5.2: 20 nm sized MFI crystals observed by (a) cryo-TEM and (b) TEM. ....	57
Figure 5.3: Cryo-TEM images of TPA-silica sols heat-treated at 40 °C for (a) 6d-PS, (b) 10d-PS, (c) 13d-PS and (d) 21d-PS. ....	59
Figure 5.4: TEM images of TPA-silica sols heated at 40 °C for (a) 9d-DS, (b) 11d-DS and (c) 15d-DS. (d) A plot showing the average size of particles as a function of heating time. ....	59
Figure 5.5: Representative cryo-TEM images of room temperature aged TPA-silica sols for (a) 390d-PS and (b) 390d-DS. SAXS patterns are shown in the insets. Corresponding high-resolution cryo-TEM images are shown in (c) and (d), respectively. Frost particles are marked by arrows in (b). ....	61
Figure 5.6: TEM images of TPA-silica sols heated at 50 °C for (a) 17d-PS and (b) 17d-DS. PSDs are shown in the insets. (c) N2 adsorption-desorption isotherms for the powder obtained from the 17d-CDP and 17d-DS. ....	62

Figure 6.1: A representative TEM image of dC6-MFI crystals synthesized at 175 °C aged for 2 days. The crystal have acquired the characteristic boat-like morphology.....	67
Figure 6.2: (a) SAXS patterns and (b) corresponding PDDFs just after TEOS hydrolysis for TPA-, dC6- and TPA/dC6-silica sols. Corresponding cryo-TEM images are shown in (c)–(e), respectively. The scale bar is same for (c)–(e) .....	69
Figure 6.3: (a) SAXS patterns for TPA-silica sols until 137 days of aging. PDDFs of 0, 1 and 9 d are shown in (b).....	71
Figure 6.4: TEM images of (a) 9d-DS, (b) 17d-DS, (c) 22d-DS, (d) 86d-DS and (e) 200d-DS. The marked crystal (by arrowhead) in (b) is magnified in the inset to reveal the surface roughness. Some intergrown crystals are shown by white arrows in (b) and (c). .....	72
Figure 6.5: (a) SAXS follow up for dC6-silica sol. PDDFs for 0, 1 and 9 days heated sols are shown in (b). A cryo-TEM image of dC6-silica for 9d-PS is shown in (c). .....	74
Figure 6.6: TEM images of (a) 22d-DS, (b) 39d-DS, and (c) 86d-DS. A cryo-TEM image of 86d-PS is shown in (d); frost particles are shown by arrows. .....	75
Figure 6.7: (a)TEM images of 250d-CDP. A HRTEM image is shown in(b) .....	76
Figure 6.8: (a) SAXS follow up for TPA/dC6-silica sol. PDDFs for 0, 1 and 9 d are shown in (b). .....	77
Figure 6.9: TEM images of (a) 39d-DS, (c) 86d-DS, (e) 200d-DS and (f) 250d-CDP, and cryo-TEM image of (b) 39d-PS and (d) 86d-PS. .....	78
Figure 7.1: A schematic illustrating the MFI growth mechanism with added new elements: i). formation of amorphous aggregates and intra-aggregate rearrangement to trigger MFI nucleation, ii) crystal faceting in the absence of nanoparticles, and iii) crystal-crystal aggregation. .....	81
Figure A.1: A representative TEM image showing characteristic morphology of dC5-MFI. Electron-diffraction pattern from the clean region of the crystal (marked by an arrow) is shown in the inset.....	89
Figure A.2: TEM micrographs ((a) and (b)) show coherent interfaces; schematics are shown in right. FFTs are shown as insets with the schematics. The spots, shown in italics in FFT of (a), have their origin in region A. ‘A’ consists a coincidence boundary (rotation angle ~53° with the b-axis as the axis of rotation).....	90
Figure A.3: A HRTEM image, with FFT inset, shows an interface with facets along (200) and (101).....	91
Figure A.4: A HRTEM image, with FFT inset, showing an interface. A probable schematic of the facets are shown at right. ....	91
Figure B.1. (a) A representative cryo-TEM image showing a tertiary particle in solution after 8 days of heating. (b) A High-resolution cryo-TEM image showing crystalline order in the particle. The inset FFT shows spots with d-spacing of about 1.1 nm.....	93
Figure B.2: HRTEM images of (a) MCM-22(P), (b) MCM-22(PS-RT), (c) deswollen MCM-22(P) obtained by acidification of MCM-22(PS-RT), and (d-f) MCM-22(PS-80). Room-temperature and 80 °C swollen precursors are noted as PS-RT and PS-80.....	94
Figure B.3:TEM images showing MFI particles synthesized in 40 nm 3DOM carbon.....	95

Figure B.4: (a) A spherical MFI crystal templated by one macropore. The inset shows the electron diffraction from the particle. (b) A MFI crystal showing the influence of confinement on the characteristic coffin-like MFI morphology. The a-facet marked by the arrowhead is enlarged.....95

---

## BACKGROUND

### 1.1 Zeolites: An Introduction

Zeolites are crystalline hydrated aluminosilicates with periodic arrangement of nanopores (4-13 Å in diameter). Zeolite frameworks are composed of networks of corner sharing  $\text{SiO}_4$  and  $\text{AlO}_4$  tetrahedra in which a net unit negative charge is associated with each  $\text{AlO}_4$  tetrahedron.<sup>1,2</sup> This charge is counterbalanced by a positive inorganic or organic ion, which can also be tailored to manipulate zeolite chemistry. Uniform distribution of crystallographically defined nanopores with molecular recognition ability of up to ~1 Å, and the presence of easily ion-exchangeable loosely bound framework counterions, make zeolites very useful materials for catalysis, separation, adsorption, and ion-exchange. Due to their unique properties, zeolites have also been reported to be promising materials as low dielectric constant (low-k) insulators for next generation computer chips,<sup>3</sup> sensor,<sup>4</sup> corrosion-resistant coating<sup>3</sup>, medicine<sup>5</sup> and for applications related to green chemistry.<sup>6</sup> Zeolites are precisely defined by four main characteristics: i) the corner sharing  $\text{SiO}_4$  and  $\text{AlO}_4$  framework, ii) the pore network, and the presence of iii) water and iv) cations. But the concept of zeolites can be expanded to oxide molecular sieves,<sup>7</sup> metal organic frameworks (MOFs),<sup>8,9</sup> porous carbon<sup>10</sup> and titanosilicates (ETS-10 and ETS-4).<sup>11</sup> Zeolites can be classified into three categories based on Si/Al ratio: low-silica ( $1 \leq \text{Si}/\text{Al} < 2$ ), intermediate-silica ( $2 < \text{Si}/\text{Al} \leq 5$ ) and high-silica zeolites ( $\text{Si}/\text{Al} > 5$ ).

The structure commission of the International Zeolite Association (IZA)<sup>12</sup> assigns a three-letter code to each framework structure. For example, ZSM-5 (Zeolite Socony Mobil-5) has MFI-type framework structure, which is defined by a 10 member-ring (MR) pore network with straight channels along the b-axis (pore-size =  $0.54 \times 0.56$  nm) and sinusoidal channels along the a-axis (pore-size =  $0.51 \times 0.55$  nm) as shown in Figure 1.1. Crystallographically, the MFI framework is defined by an orthorhombic crystal structure

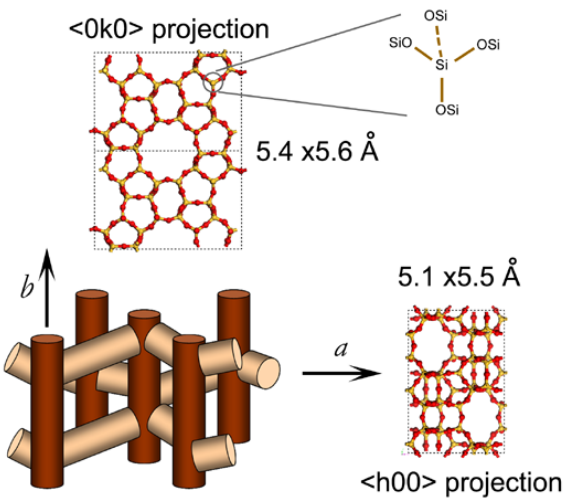


**Figure 1.1: Schematic representation of MFI framework structure.**

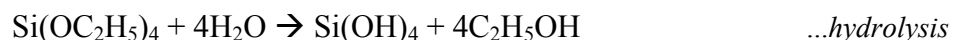
with unit-cell parameter:  $a = 20.09 \text{ \AA}$ ,  $b = 19.738 \text{ \AA}$  and  $c = 13.142 \text{ \AA}$ . ZSM-5 can be made highly acidic by having protons ( $\text{H}^+$ ) as the counter cations, which make it a very suitable heterogeneous catalyst for hydrocarbon isomerization (such as isomerization of *m*-xylene to *p*-xylene) in petrochemical industries. MFI framework allows *p*-xylene (kinetic diameter  $\sim 0.58 \text{ nm}$ ) to diffuse through but excludes *o*- and *m*-xylene (kinetic diameter  $\sim 0.68 \text{ nm}$ ). The present report is focused on Al-free ZSM-5, which is also known as silicalite-1.<sup>13</sup> The motivation behind choosing this as a model zeolite is i) the robustness of its synthesis in the presence of organic quaternary ammonium ions (such as tetraprolylammonium (TPA)), ii) relative simplicity due to the presence of only  $\text{SiO}_4$  tetrahedra in the framework, and iii) its industrially relevant shape/selective properties.<sup>13</sup>

Conventionally, zeolite crystals are synthesized in the size range of 500 to 1000s nm. However, there has been an increasing interest in the synthesis of nanozeolites (<50 nm).<sup>14</sup> Smaller sized zeolite particles have reduced diffusion lengths and high specific surface areas, which can drastically improve catalytic performance. Nano-sized zeolites

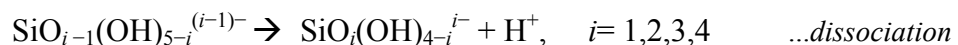
are also vital for the synthesis of zeolite-polymer nanocomposites and thin zeolite membranes (thickness under the micrometer range).<sup>14</sup> The Tsapatsis group has developed a procedure to make oriented membrane starting from zeolite seed particles followed by *in plane* secondary growth.<sup>15</sup> The smaller the seeds, thinner the membrane and better is the membrane performance. However, the synthesis of nanozeolites at high-yield requires control over nucleation and growth. But, the *nucleation and crystallization mechanism of zeolites* are not fully understood, and so tailoring the zeolite microstructures, such as particle size and morphology, pore-size, and framework types, to make zeolite useful for specific applications is still a long lasting goal of zeolite scientists.<sup>14,16</sup>

## 1.2 TPA-Silica-Water: A Model System

The nucleation and growth of silicalite-1 (referred to as MFI from here onwards) in the three component, TPA-silica-water, system has received considerable attention as a model system for the nucleation and growth studies in solution.<sup>17-20</sup> Such phenomena are of fundamental and practical significance for the synthesis of not only zeolites but a variety of other templated porous materials.<sup>21-23</sup> The clear sols are made from a silica source, most frequently tetraethylorthosilicate (TEOS), TPAOH, and water. TPAOH is also known as structure directing agent (SDA) as it acts as a template in MFI synthesis. As silica source is added to the highly basic solution (pH~11–13), it hydrolyzes to form silicic acid, Si(OH)<sub>4</sub>, as per the following reaction.



Silicic acid then participates in a series of reactions involving silanol dissociation and silica condensation to form soluble species of various charges, *i*, and sizes, *n* (*n* < 20).<sup>24</sup>



As silica content exceeds the silica solubility limit (addition of silica is shown by the arrow in Figure 1.2), a monodisperse population of precursor nanoparticles (PNs), with size 3-5 nm in diameter, forms spontaneously.<sup>2</sup> The nanoparticle formation can be represented by condensation reaction with size an order of magnitude larger than the oligomeric species ( $n > 200$ ).<sup>25</sup> The size of these PNs depends on the synthesis conditions such as pH of the solution and temperature but is independent of silica concentration.<sup>26</sup> With increasing silica content, the number concentration of PNs increases. The nanoparticles have net negative charge due to hydroxyl groups on the surface; the electrostatic repulsion between them makes them colloidally stable in solution. Upon aging at room temperature to up to  $< 200$  °C, nanoparticles containing sols yield zeolite crystals.

A debate has revolved around the direct role, or lack thereof, of the PNs in the growth of MFI crystals in TPA-silica sols for more than a decade. Researchers differ in their ideas about the relationship of these nanoparticles to the nuclei and building units of MFI.

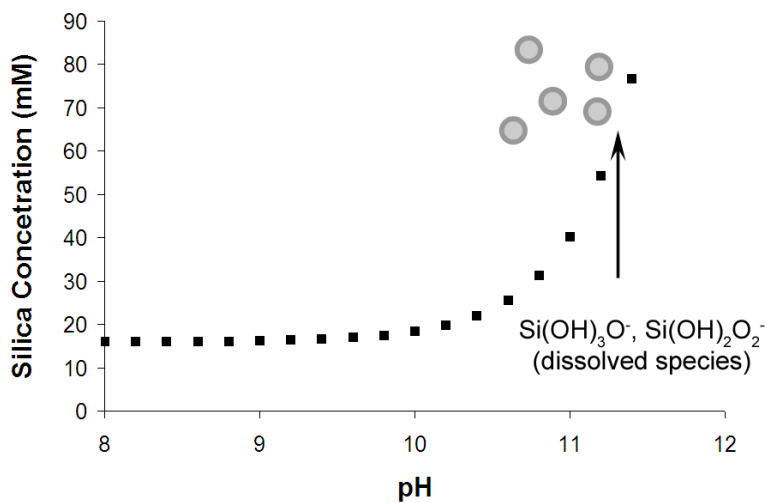


**Figure 1.2:** Silica solubility limit as a function of pH based on the prediction by Rimer et al.<sup>27</sup> The prediction is based on experiments with TPA-silica-water systems.

To meet this end, the nucleation and growth behavior of MFI has been studied at multiple temperatures and compositions.<sup>2,17,18,28-31</sup> Figure 1.3 shows a ternary diagram highlighting a sampling of sol compositions studied by other researchers<sup>2,17,28-31</sup> as well as those considered in the present work. A variety of characterization techniques such as small angle x-ray scattering (SAXS),<sup>28,32</sup> dynamic light scattering (DLS),<sup>33</sup> nuclear magnetic resonance (NMR) spectroscopy,<sup>34,35</sup> and transmission electron microscopy (TEM)<sup>18,36,37</sup> have been employed to examine MFI nucleation and crystallization. According to one hypothesis, the nanoparticles are colloidally stable amorphous species that do not directly participate in the growth of MFI. Schoeman postulated that the growth mechanism may be best described via the addition of low molecular weight species, most likely the monomer to the growing crystals.<sup>20</sup> One hypothesis is based on the assumption that PNs contribute to the zeolitic crystal growth and their addition to the growing crystal is the rate limiting step<sup>19</sup>. The research group at Leuven<sup>38-40</sup> has reported that specific silica oligomers condense to form nanoslabs with the MFI framework, which act as building blocks and directly attach to form MFI crystals. In fact, these nanoslabs have been claimed to be of precise sizes, 1.3 nm × 4 nm × 4 nm, with nine channel intersections per

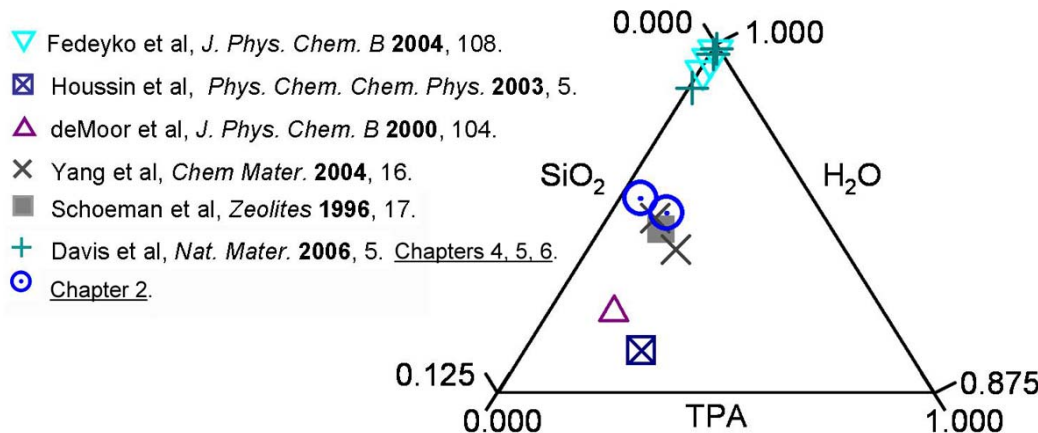
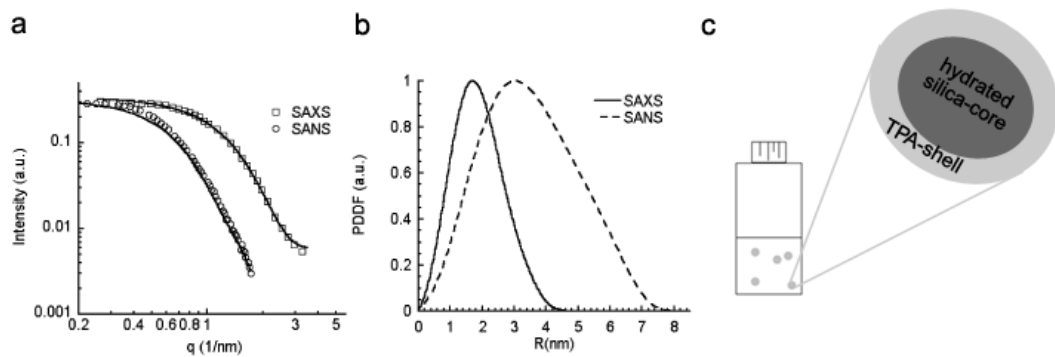


Figure 1.3: Clear sol compositions considered in previous reports and those in the present study.

particle, each containing a TPA ion.<sup>41</sup>

In 2004, researchers from the University of Delaware group reported a hydrated-silica-core/TPA-shell structure of these PNs based on SAXS and small-angle neutron scattering (SANS) experiments on a TPA-silica sol with the molar composition 40SiO<sub>2</sub>:9TPAOH:9500H<sub>2</sub>O:80EtOH.<sup>29</sup> SAXS and SANS patterns with pair-distance distribution functions (PDDFs) revealed a stark difference in the particle size (Figures 1.4(a)–(b)). For homogenous particles, PDDF gives us real space information and the plots indicate that the nanoparticle diameter is ~4.6 nm by SAXS but ~8.0 nm by SANS. The x-rays are scattered primarily by silica whereas neutrons are scattered by both silica and TPA ions. The particle's core-size was reported to be nearly independent of the size of tetraalkylammonium (TAA) cation and suggested that electrostatic force is the key element that controls their size and stability in the solution. In 2006, the group at the University of Minnesota proposed a mechanism of MFI growth in TPA-silica-water system describing the evolution of PNs to MFI nuclei and crystal growth by oriented aggregation of evolving nanoparticles.<sup>17</sup>



**Figure 1.4:** (a) SAXS and SANS data for the solution with molar composition 20SiO<sub>2</sub>:9TPAOH:9500H<sub>2</sub>O with PDDFs in (b).<sup>29</sup> (c) A schematic showing silica-core/TPA-shell structure of PNs.

### 1.3 Work Done at the University of Minnesota

A schematic of the proposed pathway is shown in Figure 1.5.<sup>17</sup> In the schematic, “A” denotes the precursor nanoparticles with disordered hydrated silica-core/TPA-shell structure. These species do not contribute to the aggregative growth. Rather, “A” species evolve through  $m$  intermediates, “B<sub>1</sub>” to “B<sub>m</sub>”, with structures increasingly similar to MFI nuclei, which are denoted as “C<sub>1</sub>”. Particles “A” along with the intermediate (“B<sub>1</sub>” to “B<sub>m</sub>”) can dissolve with a rate that is fast compared with the evolution process. The lack of participation in aggregation was attributed either due to i) their fast dissolution kinetics and/or ii) their increased colloidal stability with respect to crystal-like nanoparticles (“C<sub>1</sub>”). The increased colloidal stability can either be due to their negative surface charge, or steric stabilization by adsorbed TPA as reported before.<sup>20,29</sup> A unique aspect of the proposed mechanism is that species “B<sub>1</sub>” to “B<sub>m</sub>”, although not yet MFI nuclei, can contribute to crystal growth by attachment, and the increasing subscript of B<sub>m</sub> denotes an increasing probability for contribution to growth by aggregation. Growing crystals are denoted as C<sub>n</sub>, where  $n > 2$ . In the proposed mechanism, zeolite dissolution, crystal-crystal aggregation, and Ostwald ripening involving monomeric and oligomeric species were neglected so as to simplify the model. To date, no technique has been able to elucidate directly how the nanoparticles structurally evolve as a function of time. An atomic force microscopy (AFM) experiment on a mica surface, after dipping it into fresh and aged TPA-silica sol, lead to the conclusion that the affinity of the nanoparticles for the mica increased with aging time.<sup>17</sup> Later, based on SAXS and microcalorimetry experiment, Rimer et al.<sup>25</sup> reported a change in internal structure of the nanoparticles from amorphous to a more zeolite-like structure with aging time. According to the proposed mechanism by the Minnesota group,<sup>17</sup> the concentration of each intermediate species is significantly lower than the initial concentration of fresh nanoparticles. The concentration of the intermediates decreases significantly as the intermediates progress towards MFI. Although homogenous in size and shape, the structurally distinct population of nanoparticles exhibiting functional diversity towards aggregative crystal growth of the

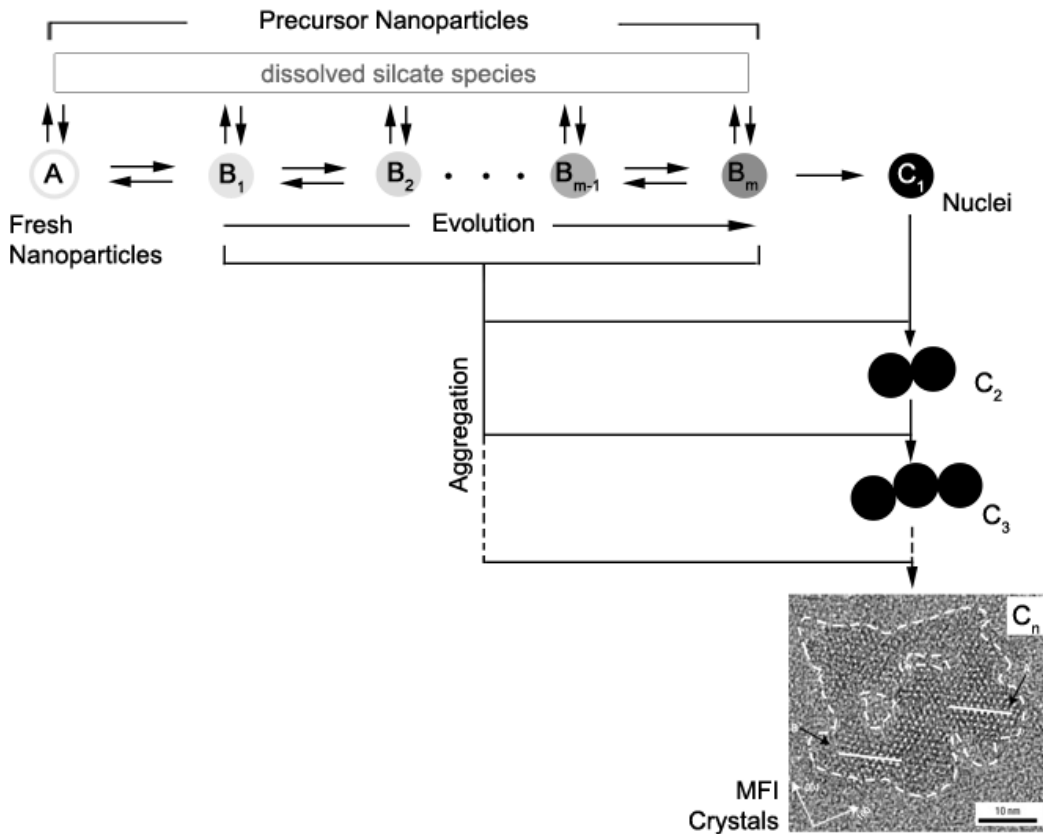


**Figure 1.5:** Schematic illustration of the mechanism proposed for nanoparticles evolution and crystal growth by aggregation.<sup>17</sup> An HRTEM image of MFI crystal oriented along the b-axis is shown (reproduced from the published report).<sup>17</sup> MFI crystal comprises of two slightly misoriented domains (indicated by two arrows). A set of parallel lines are drawn to illustrate this misorientation between the domains.

proposed model explained the experimental observations such as the prolonged induction period (about 6 months for aging at room temperature), the decrease in colloidal stability of nanoparticles with aging time, the presence of relatively large crystals at low yield during the early stage of crystallization, and the broad-size distribution of crystals throughout the growth process.<sup>17,42</sup>

The proposed mechanism was based on the characterization of room temperature aged TPA-silica sol by a number of techniques such as AFM, SAXS, cryogenic TEM (cryo-TEM), high-resolution TEM (HRTEM), and a phenomenological population balance mathematical model. Although room temperature aging may not be practical for commercial production of MFI, it enabled the Minnesota group to capture the complex steps involved in zeolite crystallization by ensuring slow evolution and avoiding complications that may be introduced during quenching before characterization. However, information regarding the structure of intermediate nanoparticles ( $B_1$  to  $B_m$ ), nuclei ( $C_1$ ) and early aggregates ( $C_x$ ,  $x < n$ ) is still very limited since they are minor components of the sols at early stages of growth. Some of the unanswered questions of the proposed model are:

1. Are the nuclei  $C_1$  crystalline? Are early aggregates, such as dimers ( $C_2$ ) and trimers ( $C_3$ ) crystalline?
2. Is aggregate-like appearance of  $C_n$  true? This is important as HRTEM was performed after isolating the crystal from other components of the solution.<sup>17</sup> Is there effect of this crystal isolation procedure on the crystal morphology and its surface structure?
3. What is the role of the nanoparticles during later stages of growth when faceting of the crystals is observed?
4. Is the proposed mechanism valid for concentrated solutions aged at elevated temperature, or for the synthesis mixture prepared using SDAs other than TPAOH?

Understanding nucleation and growth phenomena in TPA-silica solution remains elusive partly due to the complexity of the synthesis mixture and partly due to the challenges involved in the characterization techniques. The existence of nanoparticles as well as their number concentration in the TPA-silica solution is strongly dependent on the

solution pH (Figure 1.2). The nanoparticles are in dynamic equilibrium with the dissolved silica species, so they cannot be separated out for structural investigation without inducing artifacts.<sup>43</sup> Chapter 3 of this thesis introduces cryogenic-TEM as an *in-situ* imaging technique for hydrothermal growth studies in solution. Other chapters focus on MFI nucleation and growth by an extensive use of other electron microscopy techniques such as HRTEM, bright-field and dark field imaging, electron-diffraction analysis, with a combination of SAXS and N<sub>2</sub> adsorption-desorption.

#### 1.4 Thesis Organization

The present dissertation is divided into seven chapters. The chapter 2 describes the study in a concentrated synthesis mixture at 90 °C by TEM and SAXS, and demonstrates the validity of the proposed growth mechanism. The chapter 3 introduces cryo-TEM technique, discusses associated challenges, and demonstrates the importance of high-resolution cryo-TEM in the hydrothermal growth studies. The chapters 4 and 5 describe cryo-TEM and SAXS follow up of TPA-silica sol and present some new details in growth mechanism. The chapter 6 describes the influence of a dimer of TPAOH on the formation of precursor nanoparticles and on the overall course of crystallization. Finally, chapter 7 presents the concluding remarks on the present work. This dissertation also includes appendices describing defects in dC5 (a dimer of TPA)-MFI, and my involvement in other projects at the University of Minnesota.

---

**AGGREGATIVE GROWTH OF MFI<sup>\$</sup>**

Precursor silica nanoparticles can evolve to MFI crystals under hydrothermal conditions in the presence of tetrapropylammonium (TPA) cations. It has been proposed that in relatively dilute sols of silica, TPA, water and ethanol, MFI growth is preceded by precursor nanoparticle evolution and then occurs by oriented aggregation. Here, we present a study of MFI crystallization in more concentrated mixtures and propose that growth follows a path similar to that taken in the dilute system. Small angle X-ray scattering (SAXS), cryogenic transmission electron microscopy (cryo-TEM), and high-resolution transmission electron microscopy (HRTEM) were used to measure nanoparticle size and to monitor zeolite nucleation and early stage crystal development. SAXS was used to detect the onset of secondary particle formation, and HRTEM was used to characterize their structure and morphology. Cryo-TEM allowed for *in situ* visual observation of the nanoparticle population. Combined results are consistent with growth by aggregation of silica nanoparticles and of the larger secondary crystallites. Finally, a unique intergrowth structure, formed during the more advanced growth stages is reported, lending additional support for the proposal of aggregative growth.

---

<sup>\$</sup>Results presented in this chapter are published in

S. Kumar *et al.*, *J. Phys. Chem. B*, **2007**, 111, 3398

## 2.1 Introduction

Silicalite-1, an all-silica zeolite with the MFI-type framework (referred to as MFI from here onwards),<sup>12</sup> has received considerable attention as a model system in the study of hydrothermal crystal growth.<sup>17-20</sup> Through a better understanding of zeolite crystallization, it may be possible to tune crystal morphology and size for specialized applications such as in the synthesis of oriented zeolite membranes.<sup>15,44</sup> To meet this end, the nucleation and growth behavior of MFI has been studied at multiple temperatures and compositions.<sup>2,17,28-31</sup> Typically, clear precursor sols are used as the growth medium due to their reduced number of constituents and, therefore, relative simplicity. These clear sols are made from a silica source, most frequently tetraethylorthosilicate (TEOS); the structure directing agent, tetrapropylammonium hydroxide (TPAOH); and water.

Precursor nanoparticles (c.a. 5 nm) spontaneously form in these clear sols immediately following TEOS hydrolysis.<sup>2</sup> The structure of the nanoparticles and their role in MFI crystallization are subjects of extensive research. Researchers differ in their ideas about the relationship of these nanoparticles to the nuclei and building units of MFI. The research group at Leuven<sup>38-40</sup> has reported that specific silica oligomers condense to form nanoslabs with the MFI framework, which act as building blocks and directly attach to form MFI crystals. Recently, our group proposed a mechanism<sup>17</sup> describing the evolution of precursor nanoparticles to MFI nuclei and crystal growth by oriented aggregation of these primary particles; a schematic of the proposed pathway is shown in Figure 1.5. In the schematic, “A” denotes the precursor nanoparticles with a disordered silica-core/TPA-shell structure. This species does not contribute to aggregative growth. Rather, “A” species evolve through  $m$  intermediates,  $B_1$  to  $B_m$ , with structure increasingly similar to silicalite-1 nuclei, which are denoted as “C<sub>1</sub>”. Species  $B_1$  to  $B_m$ , although not yet crystalline, can contribute to crystal growth by attachment, and the increasing subscript of  $B_m$  denotes an increasing probability for contributing to growth by aggregation. Growing crystals are denoted as C<sub>n</sub>, where  $n > 2$ . To date, no technique has

been able to elucidate how the nanoparticles structurally evolve as a function of time. However, it is reported that the colloidal stability decreases as a function of time.<sup>17</sup> The structurally and functionally distinct populations of nanoparticles of the model explained the presence of relatively large crystals at low yield during the early stages of crystallization as well as broad size distribution of crystals throughout the growth process.<sup>17,42</sup> The possibility of MFI growth by crystal-crystal aggregation, which, in order to keep the discussion simple, was not considered in the initially proposed mechanism, is also included in the present chapter. Oriented aggregation occurs when crystals attach at similar crystallographic surfaces to form a new single-crystal.<sup>45</sup> To date, there are few reports<sup>17,39</sup> suggesting the oriented aggregation of precursor nanoparticles during MFI crystal growth. However, oriented aggregation has been reported to be one of the main mechanisms for nanocrystal formation in various other systems.<sup>45-51</sup>

Characterization techniques such as small angle X-ray scattering (SAXS),<sup>28,32</sup> dynamic light scattering (DLS),<sup>33</sup> nuclear magnetic resonance (NMR) spectroscopy,<sup>34,35</sup> and transmission electron microscopy (TEM)<sup>18,36,37</sup> have been employed to examine MFI crystallization in previous studies. SAXS is a uniquely sensitive technique to detect the onset of formation of a secondary population<sup>28,32</sup> due to the fact that scattering intensity goes as particle size to the sixth power ( $\text{Intensity} \propto \text{diameter}^6$ ). In this way, SAXS is indispensable in studying crystallization from clear sols if the earliest stages of crystal growth are to be captured. However, SAXS provides only an indirect measure of particle size and therefore requires considerable data interpretation. A second technique, for example high-resolution transmission electron microscopy (HRTEM), aids this data interpretation while also providing a means for direct observation of crystal evolution at the nanoscale.<sup>36,37,52</sup> Simulated HRTEM images of MFI crystals in three principal zone axes with corresponding electron-diffraction patterns are shown in Figure 2.1 (a). The HRTEM image information is primarily controlled by two parameters: sample thickness ( $t$ ) and defocus ( $\Delta f$ ). A thickness-defocus map of MFI viewed down the straight channels is shown in Figure 2.1(b). Crystallites generally sit along b-axis on TEM grid as it is the

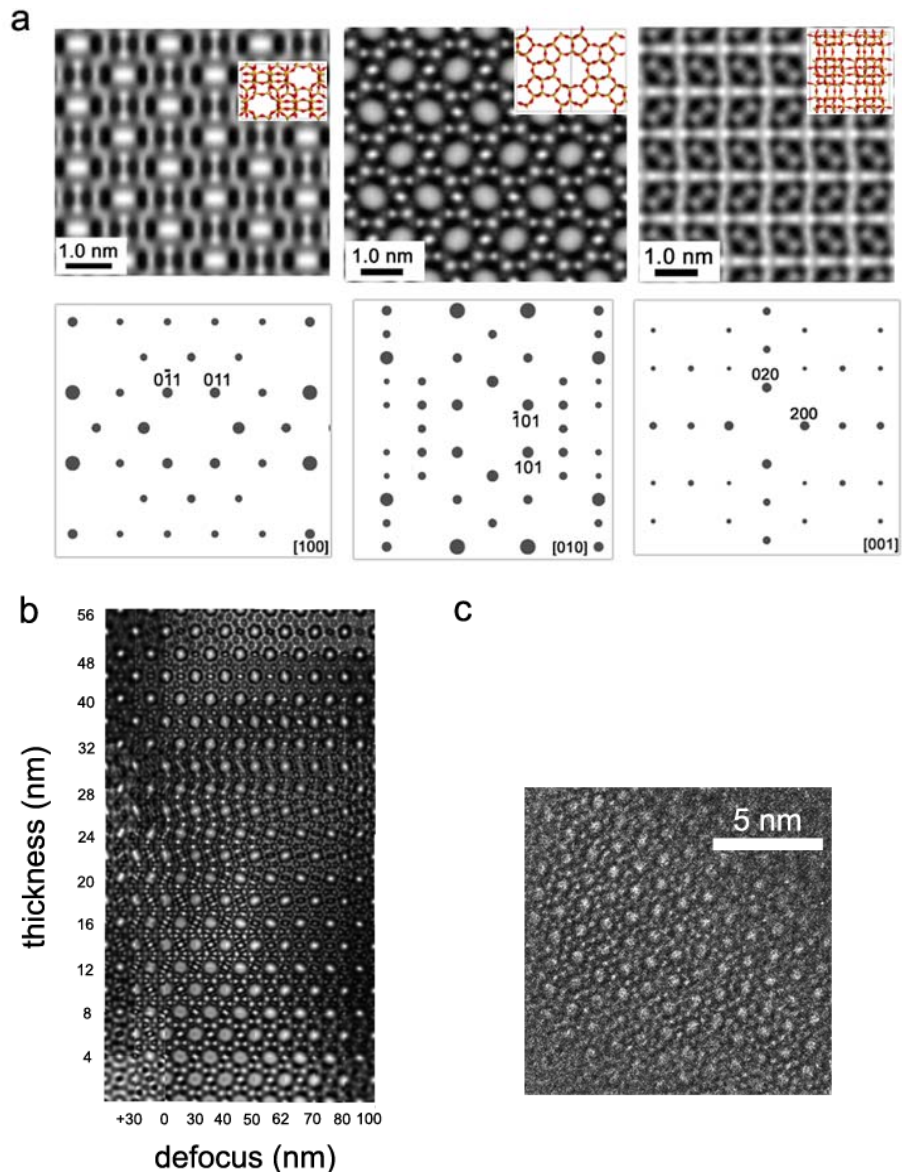


**Figure 2.1:** (a) Simulated HRTEM images along the a-, b-, and c-axis, respectively. The crystal structure of MFI is also overlapped for clarity. The diffraction pattern for each zone axis is shown below each simulated image. Images are simulated at Scherzer defocus ( $\Delta f_{Sch} = 62$  nm) and sample thickness ~5 nm. (b) The thickness-defocus map for MFI along straight channels (b-axis). Each unit cell (~2 nm along the b-axis) was divided into 8 slices. (c) An experimental HRTEM image of a MFI crystal oriented along the b-axis revealing 10MR straight channels surrounded by two 6MR and eight 5MR. This MFI crystal was grown using dC5 (dimer of TPA with 5 carbons linking the head groups) as SDA. All simulation results are for 300 kV Tecnai F-30 ( $C_s = 1.2$  mm).

thinnest dimension of TPA-MFI, so visualization along straight channels is important. All the results in Figures 2.1(a)–(b) are generated in Cerius2 by employing multi-slice simulation (details of simulation parameters are given in the Figure caption). For a comparison, an experiment HRTEM image of a b-oriented MFI crystal, revealing 10 member-ring (MR) straight channels surrounded by two 6MR and eight 5MR, is shown in Figure 2.1(c). The SAXS and HRTEM, when used in combination, provide a powerful tool for the elucidation of crystal growth behavior. In the literature, there are few reports of HRTEM investigations of MFI crystallization possibly due to the severe electron beam damage that occurs during TEM imaging of zeolites.<sup>53,54</sup> Furthermore, viewing of the crystals is often obstructed by the more highly abundant amorphous silicate species, especially at low crystal yield. However, Davis et al.<sup>17</sup> recently described a two-step dialysis procedure permitting isolation of the MFI crystals from soluble silica and TPA species.

This paper presents a study of MFI crystallization in a relatively concentrated silica-TPA sol and reports a new type of defect. Experimental observations are made by SAXS, cryo-TEM and HRTEM.

## 2.2 Experimental Methods

### 2.2.1 Synthesis

MFI was synthesized from clear precursor sols consisting of TPAOH (1.0 M Aldrich), distilled water, and TEOS (98% Aldrich) at the following molar composition:



Upon mixing of the sol components, M1 was aged at room temperature for 30 days and then heated at 90 °C for various times. Aliquots were removed at regular time intervals and quenched in water bath prior to characterization.

### **2.2.2 Small Angle X-ray Scattering**

SAXS was used to characterize the size and concentration of PNs and to detect the onset of secondary particle formation. The SAXSess SAXS instrument (Anton-Parr) was employed to characterize M1 sols. After normalizing the SAXS patterns with respect to the incident beam intensity, the scattering profile from water was subtracted as background. The GIFT software<sup>55</sup> was used to analyze the SAXS data and to correct for instrumental broadening caused by the slit-collimated incident beam. Measurements were made at room temperature (25 °C).

### **2.2.3 Cryogenic Transmission Electron Microscopy**

Specimens of M1 were prepared without dilution or alteration for cryo-TEM imaging according to the method described by Talmon.<sup>56</sup> Vitrified specimens were then transferred under liquid nitrogen to a Gatan 613.DH Cooling Holder. Images of the vitrified sol ( $T < -180$  °C) were acquired at JEOL 1210 TEM operating at 120 kV using a Gatan charge-couple device (CCD) camera.

### **2.2.4 Transmission Electron Microscopy**

The two-step dialysis procedure described by Davis et al.<sup>17</sup> was performed to isolate MFI crystals from precursor nanoparticles, dissolved silica and unreacted TPA cations prior to sample preparation for HRTEM. The purpose of dialysis was to minimize silica and TPA precipitation that typically occurs upon specimen drying. TEM specimens were prepared by diluting a small amount of dialyzed sol in ethanol and placing a few droplets onto a holey-carbon coated copper grid (Ted Pella, Inc.). Samples were then allowed to air-dry. TEM characterization was performed using a FEI Tecnai G2 F30 TEM operating at 300 kV. All TEM micrographs were collected using a CCD camera.

## 2.3 Results and Discussion

### 2.3.1 Characterization of Clear Sols

Particles ranging in size from about 1 to 50 nm and suspended in a medium (e.g., silica nanoparticles in water) are easily detectable by small angle scattering techniques given that the contrast between the particle and matrix is sufficient. In the case of x-ray radiation, the contrast is defined as the electron density difference between the particle and matrix. The measured scattering intensity, collected as a function of the scattering vector,  $q$ , is a function of this contrast as well as a function of the particle volume,  $V$ , and number concentration,  $n$ , according to the following relationship<sup>57</sup>:

$$I(q) = nV^2 \text{contrast}^2 P(q)S(q)$$

The form factor,  $P(q)$ , results from intraparticle scattering and gives information about particle size and shape. The structure factor,  $S(q)$ , is a result of interparticle scattering and therefore describes particle-particle interactions and the spatial arrangement of the particles in the solvent. In the case of dilute sols,  $S(q)$  is reduced to unity and the problem of data analysis is greatly simplified.

The clear sols were monitored using the SAXSess instrument and is shown in Figure 2.2(a). Measurements were taken at the following time steps: immediately after TEOS hydrolysis (t1), after 30 days at room temperature (t2), 30 days at room temperature followed by 2 hours (t3), 3 hours (t4), and 6 hours at 90 °C (t5). The diameter of the PNs at t1 as determined from the PDDF (not shown) is ~4.0 nm, and agrees well with cryo-TEM imaging (Fig 2.2(b)). The PNs in M1 increase in size to ~4.7 nm and exist as the only detectable species during the 30 days at room temperature. However, after only 2 hours at elevated temperature, a secondary population of larger sized particles is detected, causing a sharp increase in the low- $q$  scattering intensity. Immediately following detection of the larger particles, aliquots of the sols were removed for dialysis and

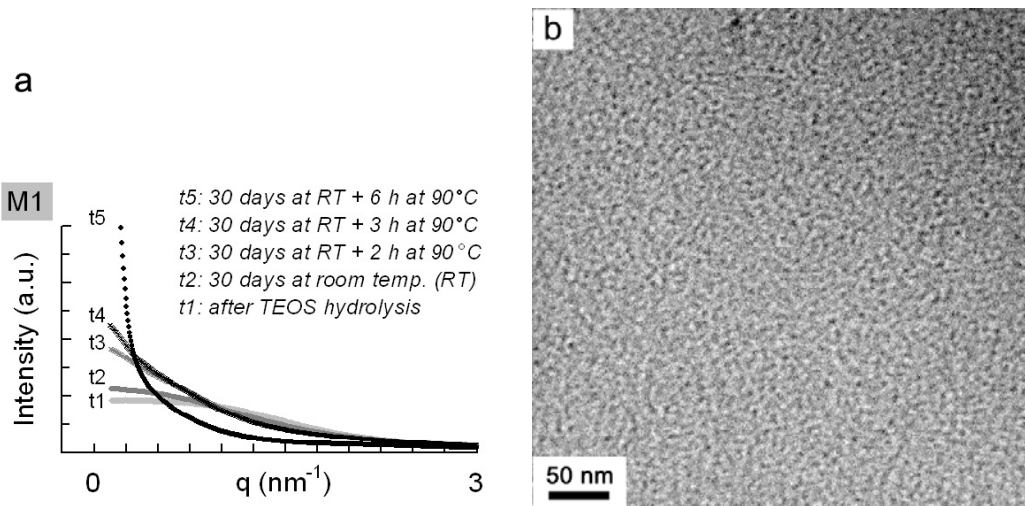


**Figure 2.2:** (a) SAXS Measurements from M1 with increasing time steps: immediately after TEOS hydrolysis (t1), after 30 days at room temperature (t2), and 30 days at room temperature followed by 2 h (t3), 3 h (t4), and 6 h at 90 °C (t5). The onset of secondary particle formation in M1 is shown to occur during the first 2 h at 90 °C. (b) M1 prior to aging was also characterized by cryo-TEM.

HRTEM characterization. The scattering intensity continues to increase beyond the initial detection of the secondary particles, signifying an increase in their size and number.

### 2.3.2 Aggregative Crystal Growth

HRTEM results show that the secondary particles are MFI crystals, which is consistent with previous results in the more dilute system.<sup>17</sup> The MFI crystallites produced by heating M1 at 90 °C for 52 hours are typically faceted and have the hexagonal prismatic shape that is characteristic of this zeolite phase.<sup>58-60</sup> Figures 2.3 (a)–(c) shows representative HRTEM images of crystallites that were isolated by the two-step dialysis procedure.<sup>17</sup> The vast majority of the crystallites display the well-faceted appearance of Figures 2.3(a) and 2.3(b), which show MFI crystallites oriented along the [010]-axis. A schematic showing characteristic hexagonal prismatic morphology is shown in Figure 2.3(d). Upon close inspection, however, small deviations from the hexagonal prismatic shape can be discerned. For example in Figure 2.3 (a), there are

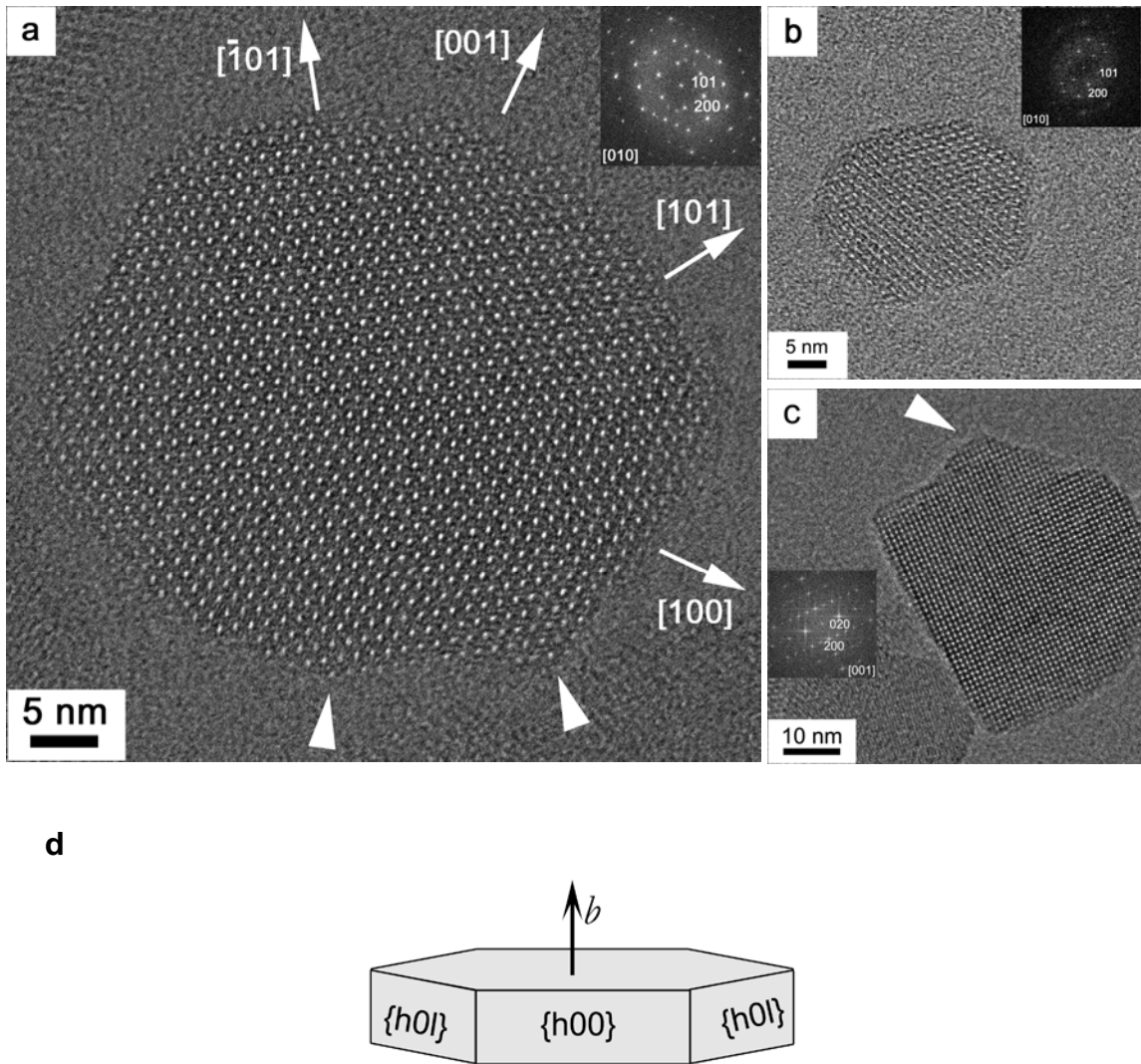


**Figure 2.3:** HRTEM images of MFI crystals from sol heat-treated for 52 h at 90 °C. Rounded protrusions of approximately 5 nm size are shown by arrowheads in (a) and (c). (d) A schematic of characteristic hexagonal-prismatic morphology of TPA-MFI.

rounded protrusions that are approximately 5 nm in size (illustrated by arrowheads). Similar features are evident in most images, including those of crystallites in other orientations (e.g., Figure 2.3(c)). Interestingly, such features were also evident in crystals produced from a much more dilute sol ( $H_2O:SiO_2$  about 22 times greater than in present work).<sup>17</sup> A preliminary explanation for the protrusions is the adhesion of nanoparticles

(ca. 5 nm) to the crystals. While *in situ* AFM imaging provided a second means for detecting nanoparticle adsorption on etched mica in the more dilute system, data interpretation in the presence of MFI crystals is less transparent. Specifically, distinction between MFI surface features and nanoparticles adsorbed on the crystal surface is difficult by *in situ* AFM and does not provide additional information in regards to the observed 5 nm protrusions shown in Figure 2.3(a). In Figure 2.3(c), crystal dimensions along [100] and [010] are comparable, which is expected for TPA-MFI.<sup>58-60</sup> Some crystallites exhibit faceted morphologies that not only have the small rounded features but also are quite asymmetric as shown in Figure 2.4. This image shows a morphology that suggests growth occurred through the oriented aggregation of at least two silicalite-1 crystals of sizes  $60 \times 40$  and  $40 \times 30$  nm.<sup>45,46</sup>

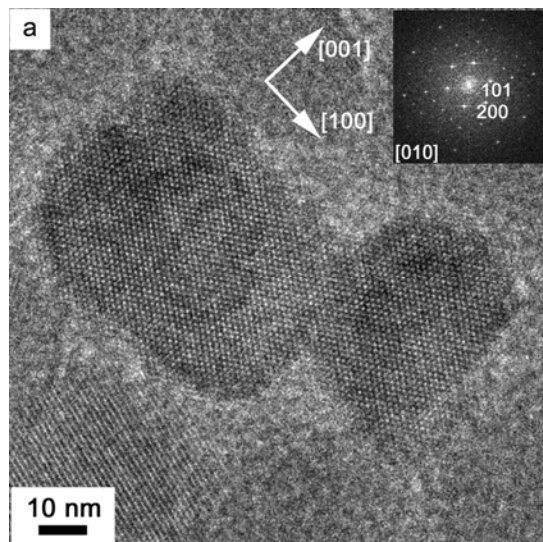


**Figure 2.4:** A HRTEM image of MFI crystal with FFT inset of sol heat-treated for 52 h at 90 °C.

As the SAXS results suggest, the emergence of secondary particles (with a larger size) occurs much earlier than 52 hours. In fact, HRTEM and SAXS data clearly demonstrate that MFI crystallites have formed within two hours at 90 °C. Through time-

resolved HRTEM characterization, crystal development in M1, progressing from the observation of extremely small crystallites (ca. 10 nm) to relatively large crystals (ca. 50 nm, as shown in Figures 2.3 and 2.4) was captured.

Figures 2.5, 2.6 and 2.7 show TEM images of crystallites isolated from suspensions heat-treated at 90 °C for 2, 3 and 6 hours, respectively. No evidence of crystal lattice fringes was seen by HRTEM prior to heat-treatment at 90 °C. In addition, electron diffraction patterns (not shown) performed on cryo-TEM specimens are characteristic of an amorphous material prior to heat treatment. Crystallinity was first observed by HRTEM in samples prepared after 2 hours at 90 °C. Representative TEM images showing ~10 nm crystallites are shown in Figure 2.5; FFTs are shown in the insets. Figure 2.5(a) shows a TEM image of a MFI crystallite oriented either along the [100]- or [010]-axis. Figure 2.5(b) shows a TEM image of a crystallite oriented away from any major zone axis with a lattice fringe spacing consistent with the MFI-type framework. The images in Figures 2.5 are reproduced on the right, and dashed white lines serve to highlight the perimeter of the crystallites. The crystallites appear to be composed of rounded MFI subdomains in the ca. 5-10 nm size range. The rounded features evident in the images shown in Figure 2.3 are also in this size range. Figure 2.6 shows TEM images of MFI after heat-treatment at 90 °C for 3 hours; crystals have increased by as much as 15 nm in size. The MFI crystal in Figure 2.6(a) is oriented along the [111]-axis but is oriented close to the [100]- or [010]-axis in (b); FFTs are shown in the insets.

Figures 2.7 and 2.8 show representative TEM images of MFI crystals present after heat-treatment at 90 °C for 6 hours. The crystals exhibit aggregate-like morphologies. Magnified images of two crystals in Figure 2.7, indicated by white arrows numbered 1 and 2, are shown in the insets. Crystals were observed to be ~10-20 nm wide and ~20-50 nm long with lattice fringes consistent with the MFI-type framework. In crystal 1, there is a slight misorientation between the lower portion and the remainder of the crystallite. This misorientation is highlighted by the white lines, which are drawn parallel to local lattice fringes and have an angular mismatch of ~19°. Crystal 2 is an aggregate-like

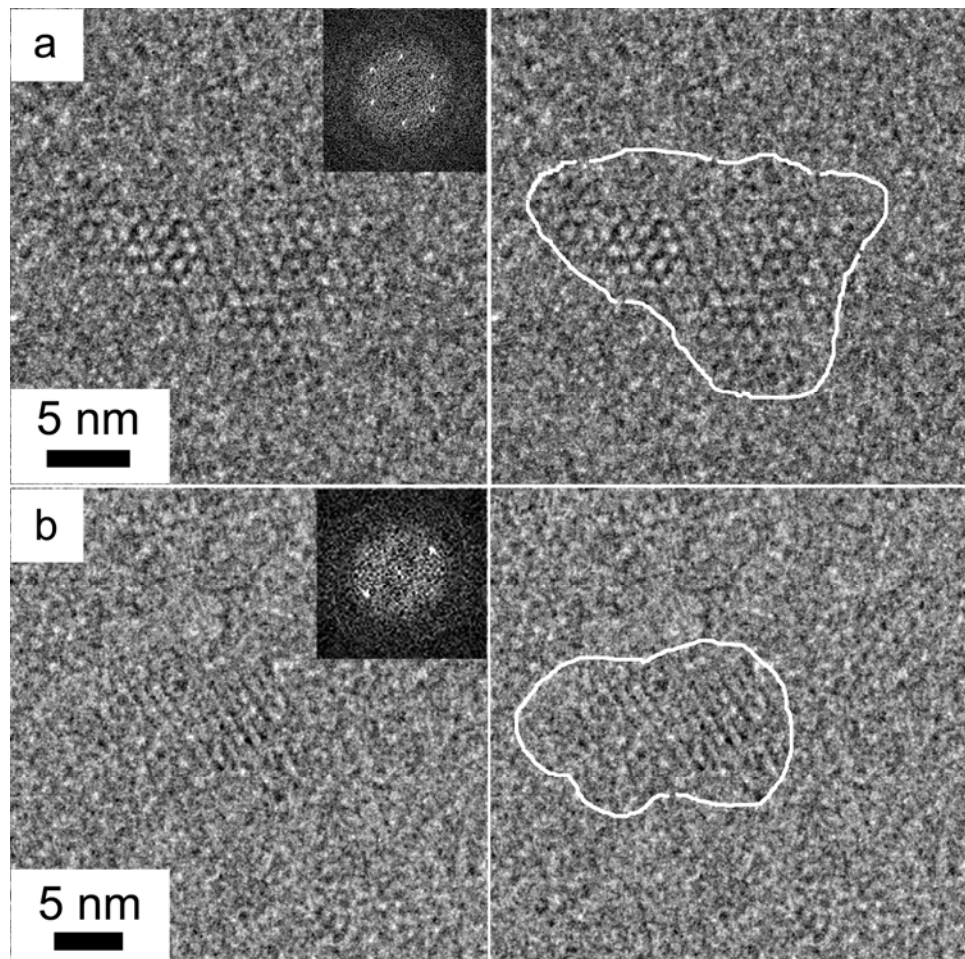


**Figure 2.5:** HRTEM images ((a) and (b)) of the first evidence of crystallinity in sol after heat-treatment for 2 h at 90 °C. MFI crystals in (a) is oriented either along a- or b-axis whereas it is tilted away from the major zone axis in (b); FFTs are shown in insets. TEM images are reproduced on the right; white lines serve to highlight the crystal perimeter.

cluster comprised of ~5-nm sized nanocrystalline domains (indicated by the arrowheads). Similar features were evident in most of the imaged MFI crystals. Such aggregate-like crystals with domain sizes on the order of the precursor nanoparticles (ca. 5 nm) are suggestive of crystal growth by oriented aggregation.<sup>17,19,45,46,61,62</sup> The observed crystal

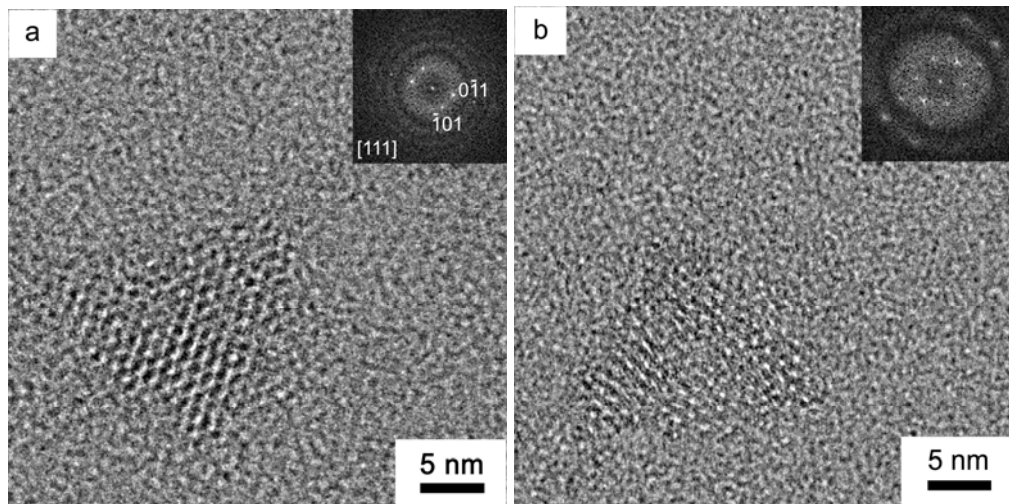


**Figure 2.6:** HRTEM images of MFI crystals present in sol after heat-treatment for 3 h at 90 °C; FFTs are shown in insets. Crystal in (a) is oriented along [111]-axis while it is oriented either along a- or b-axis in (b).

morphology is very different from the compact morphology reported for the aluminosilicate zeolites, for which a gel to zeolite transformation has been proposed.<sup>36,37</sup>

The presence of smaller crystallites (ca. 10 nm), frequently observed with the larger crystals, provides additional evidence of the oriented aggregation growth mechanism. An example image illustrating the broad crystal size distribution is given in Figure 2.8 (a); the top crystal is ~10 nm whereas neighboring crystals are ~20 nm in size. A wide particle size distribution is consistent with the model proposed previously<sup>17,42</sup> for MFI crystal growth in dilute silica sols. Although aggregation of amorphous nanoparticles followed by crystallization of the aggregate upon reaching some critical aggregate size is another possibility to explain the observed morphology, a tighter particle size distribution would be expected and the observed lattice misorientations could not be explained. It is also possible that the dialysis procedure alters the crystal morphology in some way. For example, amorphous regions of the particle may dissolve upon dialysis. However, the formation of single crystal aggregates during dialysis is improbable and therefore

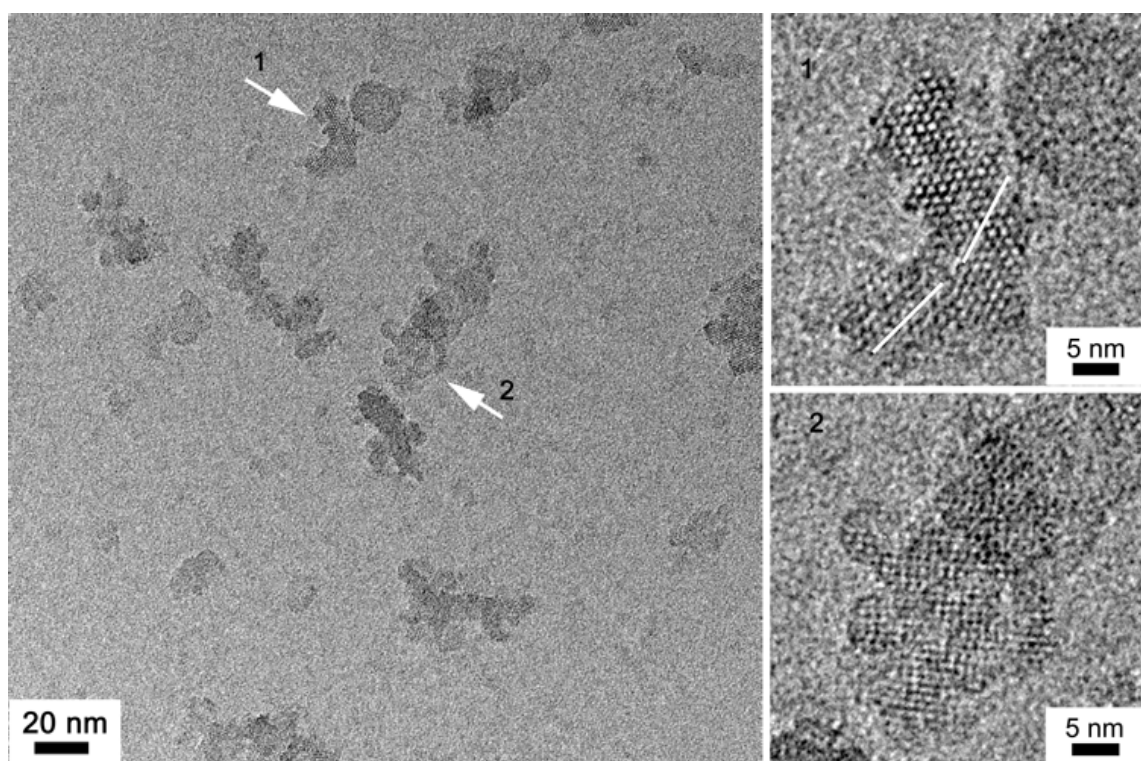


Figure 2.7: HRTEM images showing MFI crystals formed after heat treatment for 6 h at 90 °C.

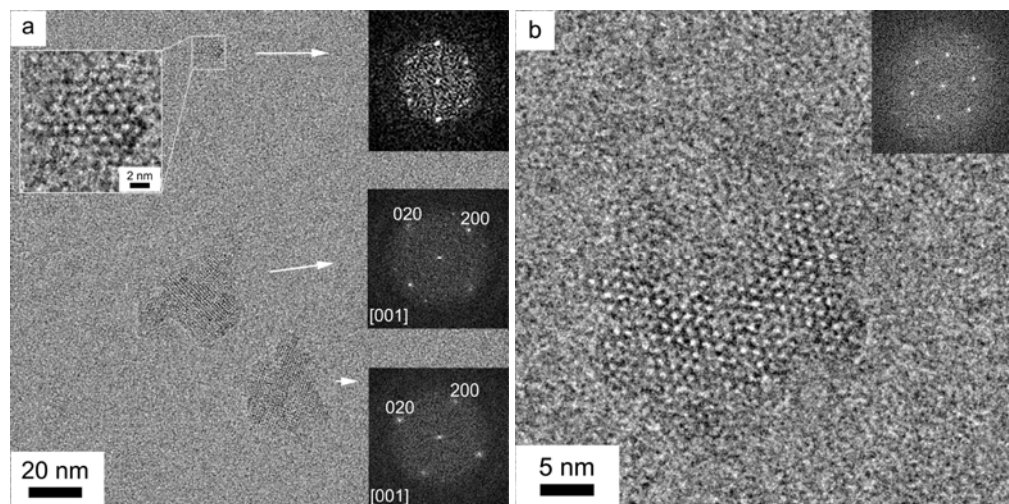
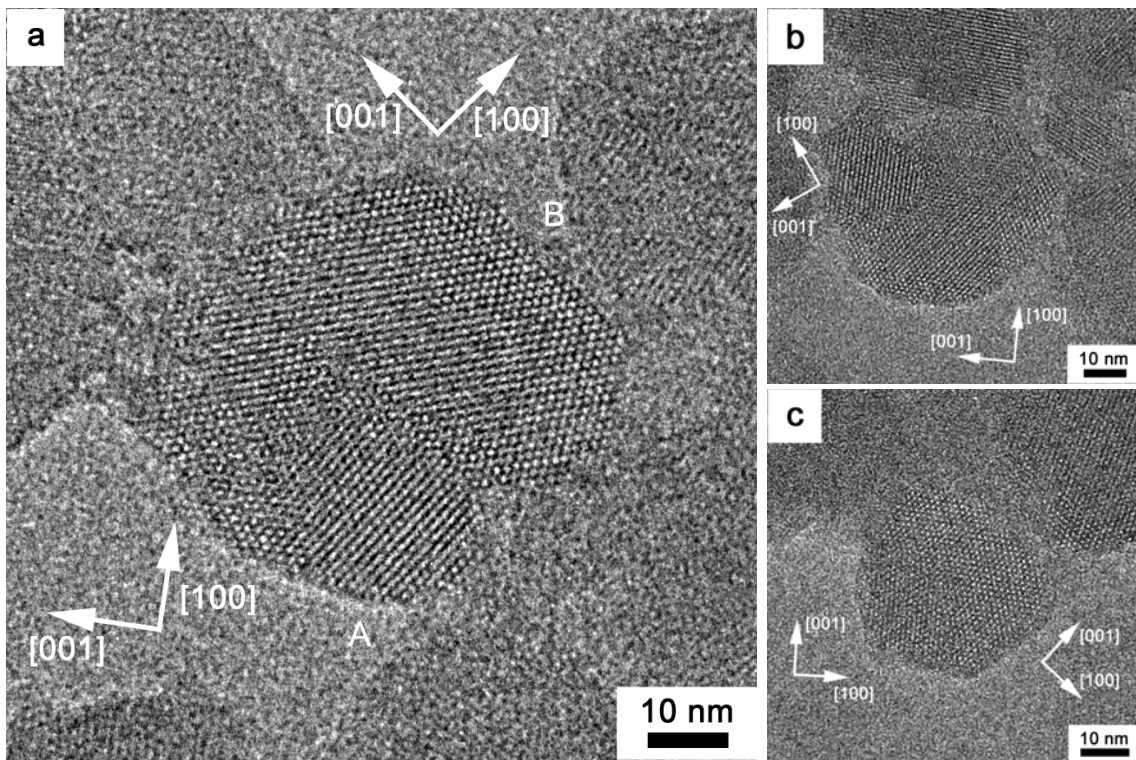


Figure 2.8: HRTEM images of MFI crystals present in sol after heat treatment for 6 h at 90 °C; FFTs are shown in insets.

oriented aggregation remains as the most likely explanation of the experimental observations reported here.

Detailed examination of these HRTEM images (Figures 2.5, 2.6 and 2.7) yields three key observations. Firstly, crystallite size increases with increasing crystallization time at 90 °C. Secondly, the crystallites appear to be composed of an ever-increasing number of primary particles. Thirdly, the rounded protrusions are retained and are in the ca. 5-10 nm size range. Based on these observations, we hypothesize that the rate of growth by aggregation during the early stages of crystallization is substantially faster than the rate of recrystallization, a process that would smoothen out such features. During the latter stages of growth (i.e., 52 hours), the crystals become more compact and faceted suggesting that growth at these longer times is occurring by monomer addition. This competing growth process (monomer addition) becomes important during the latter stages due to a combination of increased crystal surface area, increased sol pH, and reduced nanoparticle number concentration and was also observed in the more dilute system.<sup>17</sup> Consideration of the time-resolved SAXS profiles (Figure 2.1(a)) provides evidence that after 6 hours at 90 °C, the number of nanoparticles present has been reduced considerably. More specifically, the scattering intensity for  $q > 0.8 \text{ nm}^{-1}$  is significantly less after the 6-hour heat-treatment than the scattering intensity at earlier times.

An additional feature consistent with the proposed growth mechanism persists in some crystals up to at least 52 hours of hydrothermal growth. Specifically, MFI crystals imaged after 52 hours at 90 °C are sometimes found to contain unique defects that may be explained by an aggregative growth mechanism. MFI crystals possessing this signature defect are shown in Figures 2.9(a)–(c). The images show MFI crystals composed of distinct regions that are misoriented with respect to one another. Moreover, the individual crystalline regions have a common axis of rotation <010>, and for the crystals shown in Figure 2.9, the regions are related to each other by an angle of 37.3° ( $\pm 2.5$ ). The measured angle of rotation was determined from calibrated images using



**Figure 2.9:** HRTEM images showing intergrown MFI crystals present in sol after heat-treatment for 52 h at 90 °C. Pairs of white arrows show the crystallographic orientation of the two regions.

Gatan Digital Micrograph. To date, this type of misorientation in MFI has not been reported.

Further inspection shows that the interface between the misoriented regions is not a sharp boundary (Figures 2.9(a) and 2.9(c)). The measured angles of misorientation,  $\sim 37.3^\circ$  for the three crystals shown in Figure 2.9, may be interpreted by considering the MFI framework structure. In this zeolite, the angle between  $<101>$  and  $<001>$  in the MFI framework is  $\sim 34^\circ$ . In the image of the crystal shown in Figure 2.9(a),  $[101]_A$  is parallel to  $[001]_B$ , and the misorientation between  $[101]_A$  and  $[101]_B$  is  $37^\circ$ . This data could indicate that it is the arrangement of the straight pores that controls the nature of the defect. The angular consistency coupled with the morphology of these intergrown crystals suggests that such particles are formed by oriented aggregation. If, instead, the intergrowth was the result of two crystallization events in a single amorphous particle, the

angular relationship would likely vary from one intergrowth to the next. There are reports that growth by oriented aggregation can lead to the formation of defects such as twin boundaries and other interfaces.<sup>17,45,61</sup> The only requirement for oriented aggregation is that structural accord be achieved at the interfaces. Thus, we hypothesize that when MFI crystallites achieve an orientation in which the straight pores in one subunit are arranged parallel to the [001] in a second subunit, oriented aggregation can occur. Preliminary results are in agreement with this argument, however, more results and extensive image simulations are necessary to fully interpret the dependence of the intergrown particles' angular relationship on the arrangement of straight pores in MFI. The low frequency of intergrown particles likely indicates that this type of structural accord does not result in as low an energy configuration as oriented aggregation in which the crystallites are oriented with respect to all three crystallographic axes (or close to it). It should also be noted that intergrown MFI crystals were not observed during the early stages of crystallization. Rather, it seems that the intergrowth is a unique consequence of crystal-crystal aggregation ( $C_n-C_n$ ) during the latter stages.

## 2.4 Conclusions

The combination of two techniques, SAXS and time-resolved HRTEM, was employed to track MFI crystallization in a concentrated silica sol. SAXS and cryo-TEM provided a means for characterizing the precursor nanoparticles and SAXS enabled early detection of larger particles, samples of which could then be prepared for HRTEM imaging. The development and growth of aggregate-like crystals (Figures 2.5–2.8) that later transform to display faceted (Figure 2.3) to rounded-faceted morphologies (Figures 2.4 and 2.9) was followed by HRTEM. Aggregate-like crystals with domains on the order of the precursor nanoparticles during the initial stage of crystallization are consistent with the oriented aggregation mechanism. The reported intergrowth structures observed in the MFI crystals provide additional evidence for growth by oriented aggregation. The results

from this hydrothermal growth study of MFI, when taken collectively, strongly suggest that crystallization in a concentrated precursor sol follow a similar pathway (recall schematic in Figure 1.5) that was proposed to describe crystal growth in a more dilute system.<sup>17</sup>

#### ACKNOWLEDGEMENTS

The SAXS data and cryo-TEM image in Figure 2.2 were acquired by Dr Tracy Davis.

---

## HIGH RESOLUTION CRYO-TEM OF NANOZEOLITES

This chapter introduces the cryogenic transmission electron microscopy (cryo-TEM) technique in context to zeolite growth studies. The challenges associated with sample preparation and early stage crystal growth studies are discussed. High-resolution cryo-TEM of zeolite nanocrystallites is demonstrated on up to ~20 nm sized zeolite crystals. The formation of artifacts, especially transformation of vitreous into crystalline ice, and their implication on high-resolution imaging are also discussed.

### 3.1 Introduction

Cryogenic transmission electron microscopy (cryo-TEM) is a vital technique to study liquid and biological systems.<sup>63,64</sup> However, cryo-TEM has not been explored much to study nucleation and crystal growth from solution primarily due to the requirement of structural resolution to determine crystalline phases. A cryo-TEM study of zeolite growth from solution imposes two-fold challenges: first, the electron-beam sensitivity of material<sup>53,54,65,66</sup> and second, the issues inherent to the technique.<sup>67</sup> The open framework structure, presence of organic ions in the zeolite channels, smaller size of crystallites ( $\leq 50$  nm, a requirement for the early stage zeolite growth studies) make zeolite materials difficult to characterize by electron microscopy. The detection of the crystalline-phase requires a resolution limit of a few Å to a nm depending on the size of unit-cell. For example, the resolution should be 9 Å or better to confirm the presence of MFI-type phase. We can easily get this resolution in state-of-the-art TEM instruments available today, but issues arise due to imaging at cryogenic temperature ( $\leq 180$  °C).

Imaging at cryogenic temperature imposes challenges such as frost formation, film-thickness control, and specimen-drift.<sup>67-69</sup> Frost formation during sample preparation (and transfer) is unavoidable but can be minimized by careful sample handling in a clean

environment. Film-thickness is controlled by adjusting the number of blots (by trial and error) and blot-time. Specimen-drift is caused by the temperature gradient around the specimen. Its affect can be minimized by adjusting exposure-time and binning.

Based on a non-cryogenic TEM study of electron-beam irradiated quartz and multi-slice simulation, Qin et al.<sup>70</sup> reported that a specimen can appear perfectly crystalline till the portion of the amorphous is less than one half of the sample thickness. The TEM image appears dominantly disordered only after the amorphous portion has reached about two-third of the specimen thickness. Interesting enough, the simulation results were similar irrespective of the position of the amorphous inclusion embedded in the crystalline matrix. Qin et al's study points out the difficulty in high-resolution cryo-TEM imaging; if the crystallites in investigation are very small, than the thickness of the vitreous-film is the limiting parameter. Assuming a film-thickness of 50-100 nm, a rough approximate of the smallest crystallite size that can be imaged with structural resolution will be about 17-33 nm. However, the type of chemical bonds, size of unit-cell, and the beam stability of crystals will be among other parameters in ensuring high-resolution cryo-TEM of crystallites.

Acquiring a good cryo-TEM image with adequate contrast without inducing any artifacts is always an issue.<sup>67-69</sup> Artifacts are described as the microstructures that are not present in the original sample, but are rather formed during sample preparation (such as shear force due to blotting, solvent evaporation after blotting, or frost formation) or due to the electron-beam irradiation (such as amorphization of the crystalline material and transformation of vitreous into of crystalline ice).<sup>71</sup> High-resolution cryo-TEM requires an intense electron-beam on a relatively smaller area to ensure enough electron-dose to visualize atomic or pore channels with adequate contrast without damaging the original microstructure. Therefore it is important to optimize the electron-dose for high-resolution imaging as well as fine-tune the imaging parameters such as binning and exposure time.

Cryo-TEM samples are generally prepared by quenching the sample from room temperature to below -180 °C at atmospheric pressure ( $10^5 \text{ Nm}^{-2}$ ). The temperature is maintained through out the characterization, but the pressure decreases by 10 orders of magnitude once the sample is inside the TEM column ( $<10^{-5} \text{ Nm}^{-2}$ ).<sup>72</sup> Water is often the major component of the samples to be examined, which have led to many studies on the possible microstructures of water at such a low temperature and pressure.<sup>64,73-75</sup> In these conditions, three forms of ice: vitreous ( $I_v$ ), hexagonal ( $I_h$ ), and cubic ( $I_c$ ) are encountered.  $I_v$ , being kinetically trapped amorphous phase, is the only form of ice that is desired for cryo-TEM imaging. However,  $I_h$  is the only thermodynamically stable phase at these conditions; it has a hexagonal close packed structure (wurtzite-type) with  $a = 4.519 \text{ \AA}$  and  $c = 7.363 \text{ \AA}$ .<sup>76</sup>  $I_c$  is a metastable form of ice formed at moderately fast cooling rate; it is face centered cubic (diamond-type) with  $a = 6.358 \text{ \AA}$ .<sup>76</sup>  $I_h$  may contain defects such as dislocation, stacking faults and grain boundaries.<sup>73</sup> If not kept at low temperature, or if the electron-beam exposure is not kept to the minimum,  $I_v$  can transform first to  $I_c$  followed to  $I_h$ .<sup>64</sup> The first section of the chapter demonstrates high-resolution cryo-TEM imaging, and the second section discusses the transformation of vitreous into crystalline ice under prolonged illumination.

## 3.2 Experimental Methods

### 3.2.1 Synthesis

Different samples used in this chapter are summarized below. The possible crystalline phases in these samples can be crystalline silica ( $\alpha$ -quartz), crystalline ice ( $I_h$  or  $I_c$ ), and MFI.

(A) 20SiO<sub>2</sub>/9TPAOH/9500H<sub>2</sub>O/80EtOH (noted as S1)

Sol S1 aged at room temperature for 240 days (pH~11.5).

- (B)  $\leq 20$  nm sized MFI crystals suspended in water. (pH  $\sim 8.0$ )  
Zeolite particles were synthesized by confined growth method.<sup>77</sup>
- (C) Sol S1 aged at 40 °C for 15 days and after dialysis (pH  $\sim 7.5$ ).  
The dialysis procedure was performed to isolate MFI crystals from other components. The detail is given in chapter 5.
- (D) Sol S1 aged at 40 °C for 10 days and after dialysis (pH  $\sim 7.5$ ).

### **3.2.2 Cryo-TEM**

Specimens were prepared for cryo-TEM imaging according to the method described by Talmon.<sup>67</sup> The droplets were thinned to a film by gently blotting with filter paper. Immediately after thinning, the specimen was plunged into liquid ethane and then quickly moved to a liquid nitrogen reservoir. Vitrified specimens were then transferred under liquid nitrogen to a Gatan 613.DH cooling holder. The imaging was performed at -180 °C by using an FEI Tecnai G2 F30 TEM operated at 300 kV. The microscope has a twin-pole piece with a point-to-point resolution of 0.24 nm and enabled us to obtain images with structural resolution.

## 3.3 Results and Discussion

### **3.3.1 High Resolution Cryo-TEM of MFI Nanocrystals**

A high-resolution cryo-TEM image of 240 days room temperature aged silica sol (sample A) is shown in Figure 3.1. An aggregate-like particle, shown inside a rectangular box, is embedded in a sea of precursor nanoparticles. The weak contrast from this particle is a general observation of cryo-TEM imaging, which is either due to the thickness of the vitreous film, or overlapped dot-like contrast from the nanoparticles ( $\sim 10^{17}$  particles/cc), or due to the low electron-dose condition of TEM imaging. It is important to note that the visualization of these embedded particles is extremely difficult while on microscope

because of their barely visible contrast. This particle with size  $70\text{ nm} \times 30\text{ nm}$  is concluded as a MFI crystal only after a closer look. A magnified image of the particle revealing lattice fringes are shown in the bottom-right. The corresponding Fast Fourier Transform (FFT), indicating bright and dark dots in high-resolution image to be straight channels of MFI framework, is shown in the top-right. MFI crystallites do not have a defined morphology (such as cubes, spheres or cylinders) during earlier stages of growth, which impose another issue to distinguish them at low magnification as they appear similar to frost particles (an artifact of cryo-TEM). These are only distinctly distinguishable as zeolite particles at relatively higher magnification after revealing their structure. The dilute composition of S1 (20 moles of silica in 9500 moles of water) added

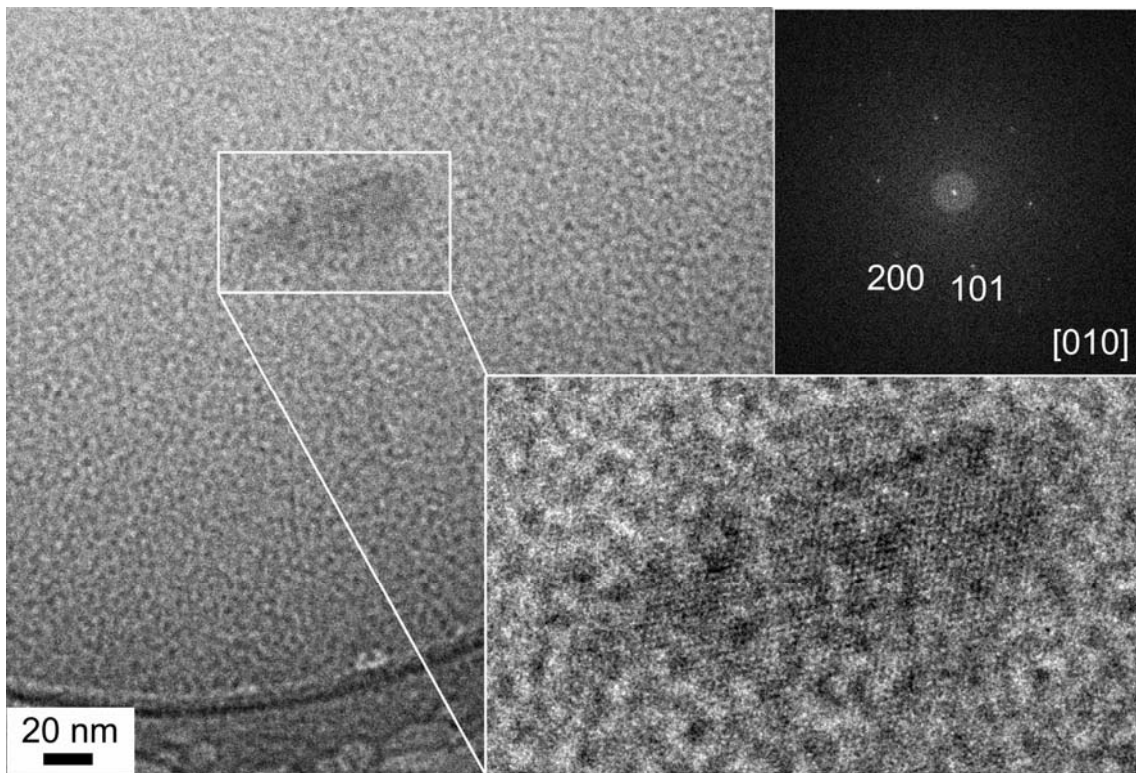


**Figure 3.1:** A representative cryo-TEM image of a MFI crystallite embedded in vitreous TPA-silica sol aged for 240 days ( $\text{pH} \sim 11.5$ ). Dot-like contrast is due to the presence of precursor nanoparticles. Magnified image of the crystallite is shown in bottom-right and FFT is shown in the top-right.

with our desire to elucidate the events during early stages of zeolite growth and prior to crystallization made the detection of the particles in the present work a major challenge. Even if all SiO<sub>2</sub> converted to zeolite, the zeolite volume fraction would be 0.32%. At the small yield studied in chapters 4 and 5, the volume fraction is well under 0.016%. Low-dose imaging module (available on FEI Tecnai instrument) could not be used in the present study due the sparse crystallite population on the TEM grid; however, low-dose was optimized manually.

We demonstrated that, besides metal nanoparticles,<sup>78</sup> highly electron-beam sensitive such as zeolites can be imaged with structural resolution while maintaining the solution microstructure. In order to push the technique further to reveal structural information from smallest possible zeolite particles, microscopy was done on sample B. A representative cryo-TEM image of a MFI crystallite, with FFT inset, is shown in Figure 3.2(a); the crystallite is 14 nm × 18 nm in size. FFT shows spots (~11 Å) corresponding to the MFI framework. This result demonstrates that it is possible to reveal zeolite phase

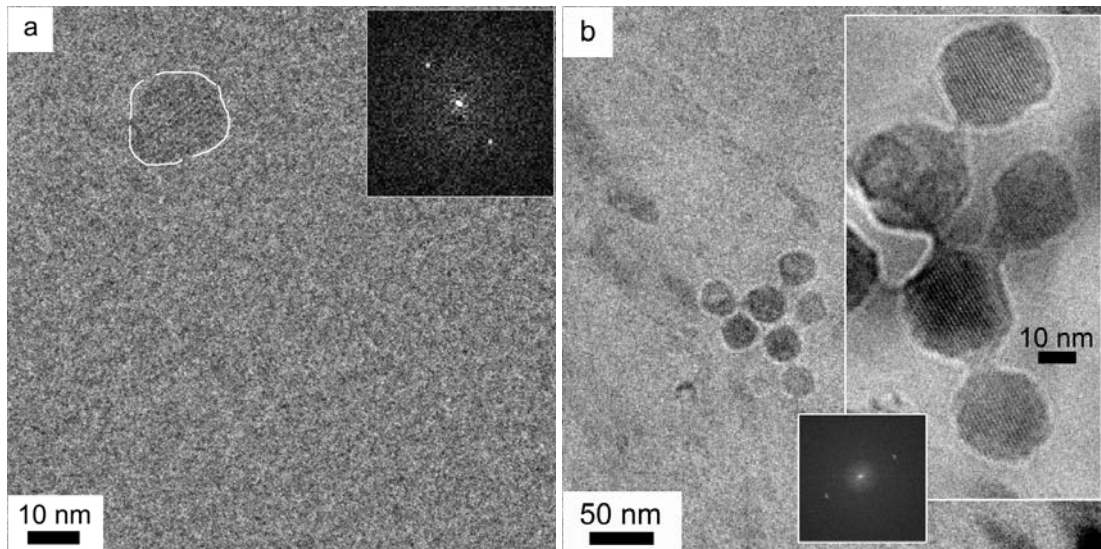


**Figure 3.2:** (a) A representative cryo-TEM image of 14×18 nm sized MFI crystal. Spots in inset FFT correspond to 11 Å. (b) Cryo-TEM image indicating MFI particles to be single-crystalline.

by cryo-TEM in at least 15-20 nm MFI crystallites irrespective of the challenges associated with the technique. One more cryo-TEM image of the same sample is shown in Figure 3.2(b). Seven particles are connected through the neck, and the inset high-resolution image and FFT indicate these MFI crystallites to be single-crystalline.

### 3.3.2 Formation of Crystalline Ice

If imaging is not performed quick enough (<5 mins), which is always an issue as fine tuning of focus and alignment can engage a couple of minutes, vitreous ice can transform into crystalline ice. A representative cryo-TEM image of the sample A is shown in Figure 3.3. The image has a uniform and weak contrast except the features, marked by an arrow, exhibit diffraction contrast. The inset FFT, taken from the whole image, suggests polycrystallinity with the ring corresponding to  $d_{hkl} \sim 3.3\text{-}3.8 \text{ \AA}$ . Bottom region showing no contrast showed similar ring in FFT. Neither  $\alpha$ -quartz nor MFI match with these d-spacings. This appears to be approximately  $\{1100\}$ -type spots of  $I_h$  or  $\{111\}$ -type spots of  $I_c$ . Besides the ring, there are other spots noted as M and N, corresponding to 2.6 and 2.2  $\text{\AA}$ , respectively, which match with low-index d-spacing of crystalline ice.

A cryo-TEM follow-up of the nucleation and crystallization is shown in Figure 3.4 (sample B). Particle-like features sitting on the vitreous ice in Figure 3.4(a) are MFI crystals (same as in Figure 3.2); the absence of lattice fringes is either due to their amorphization under electron-beam, or their improper orientation, or due to the relative thickness of the film. The corresponding FFT is shown in (b), which indicates that the features in the image are amorphous. The vitreous ice is stable for a relatively longer time (about 500 s), after which the first evidence of crystalline ice is observed (Figure 3.4(c)). The FFT corresponding to (c) is shown in (d); there are sets of spots with  $d_{hkl} \sim 3.7 \text{ \AA}$ . Most of the image shows a weak contrast, but an emerging diffraction contrast is evident in the bottom-right of the image (shown by an arrow). Once the crystalline ice is formed, it propagates very quickly as shown in the image acquired just after 10 s (Figure 3.4(e));

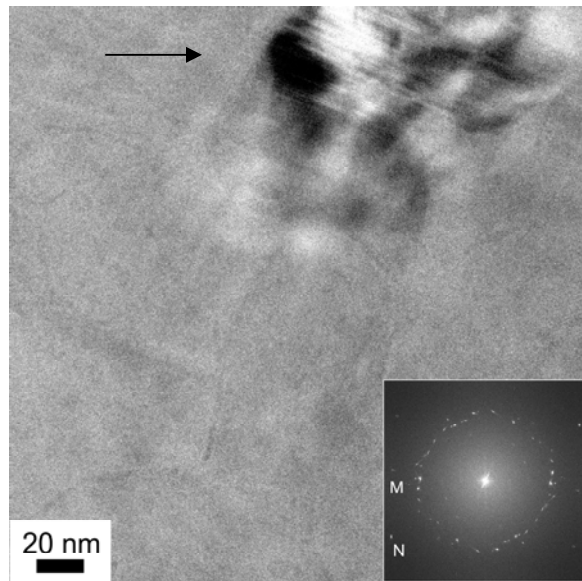


**Figure 3.3:** A representative cryo-TEM image of sample A with inset FFT is shown. The first ring of spots corresponds to  $d_{hkl} \sim 3.7\text{-}3.9 \text{ \AA}$ . The spots marked as M and N correspond to 2.6 and 2.2  $\text{\AA}$ , respectively.

features showing the diffraction contrast in the bottom-right in (c) have propagated towards the center in (e). The FFT corresponding to (e) is shown in (f); the number and intensity of spots have increased suggesting larger fraction of crystalline ice. This observation also agrees with Talmon et al<sup>64</sup> that electron beam damage is less severe in vitreous ice than in crystalline ice, i.e., once ice nucleates, it quickly propagates. Most commonly,  $I_h$  forms thin sheets of crystals with thinnest dimension along the basal plane.<sup>76</sup> The  $<0001>$ -oriented hexagonal crystalline ice would give rise to  $\{1\bar{1}00\}$ -type spots ( $\sim 3.9 \text{ \AA}$ ) as the first ring in FFT. It appears that  $I_h$  forms numerous thin ice crystals stacked on the basal plane.

A TEM image showing a general appearance of the sample C, after the formation of crystalline ice, is shown in Figure 3.5(a). Two features noted as 1 and 2 are further shown in (b) and (c). Figure 3.5(b) shows a region with weak contrast and absence of any

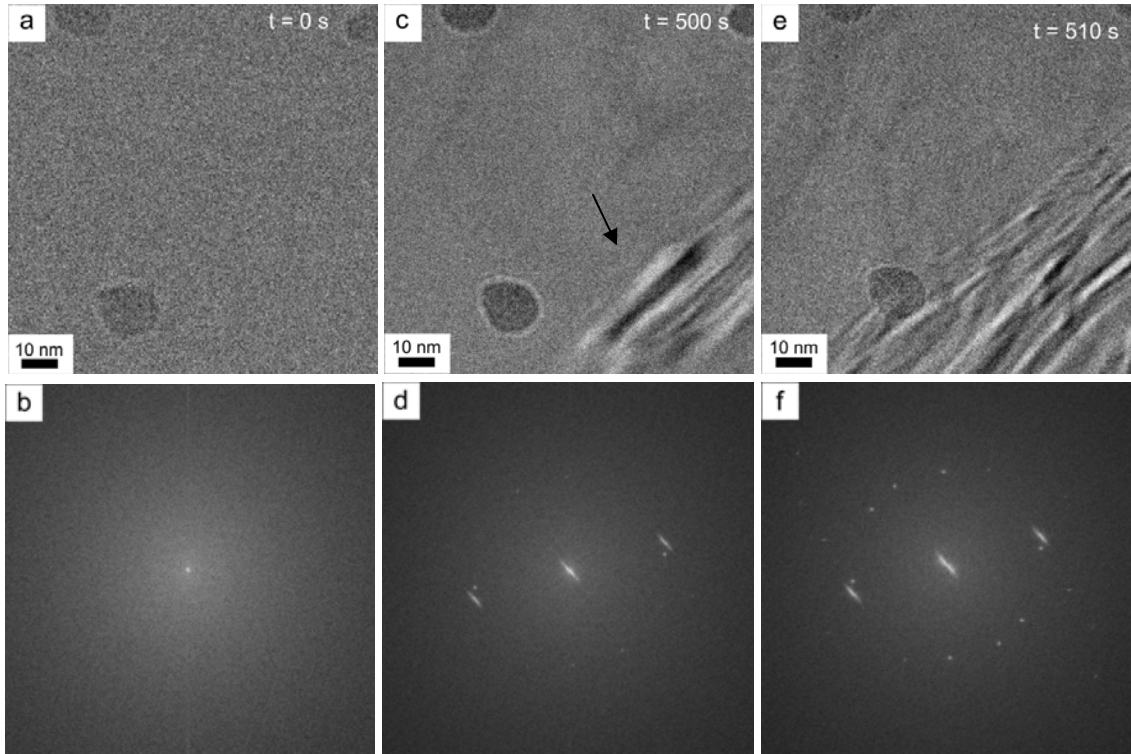


**Figure 3.4:** (a) A cryo-TEM image with (b) FFT of sample B. (c) Crystallization of hexagonal ice occurs after about 500 s, which then propagates very fast as shown in (e). FFT corresponding to (c) and (e) are shown in (d) and (f), respectively.

detectable feature. However, the FFT shown in the inset shows a single-crystalline  $I_h$  oriented along [0001]-axis. A square region in the bottom of the image has further magnified to reveal a set of {1010}-type lattice fringes. The central region of the feature noted as 2 in Figure 3.5(a) is magnified in 3.5(c). The corresponding FFT is shown in the inset; two sets of {1010}-type planes intersect each other at  $\sim 40^\circ$ .

An interesting example of the interference of crystalline ice with the original sample microstructure is demonstrated in Figure 3.6 (Sample D). A square-region, showing the particle with visible lattice fringes, is further magnified in the inset. The FFT from this region is shown in the inset (bottom-right). The set of spots indicated by “P” ( $d \sim 9.6 \text{ \AA}$ ) can be either  $d_{\{200\}}$  or  $d_{\{101\}}$  of the MFI-type framework structure. However, other spots

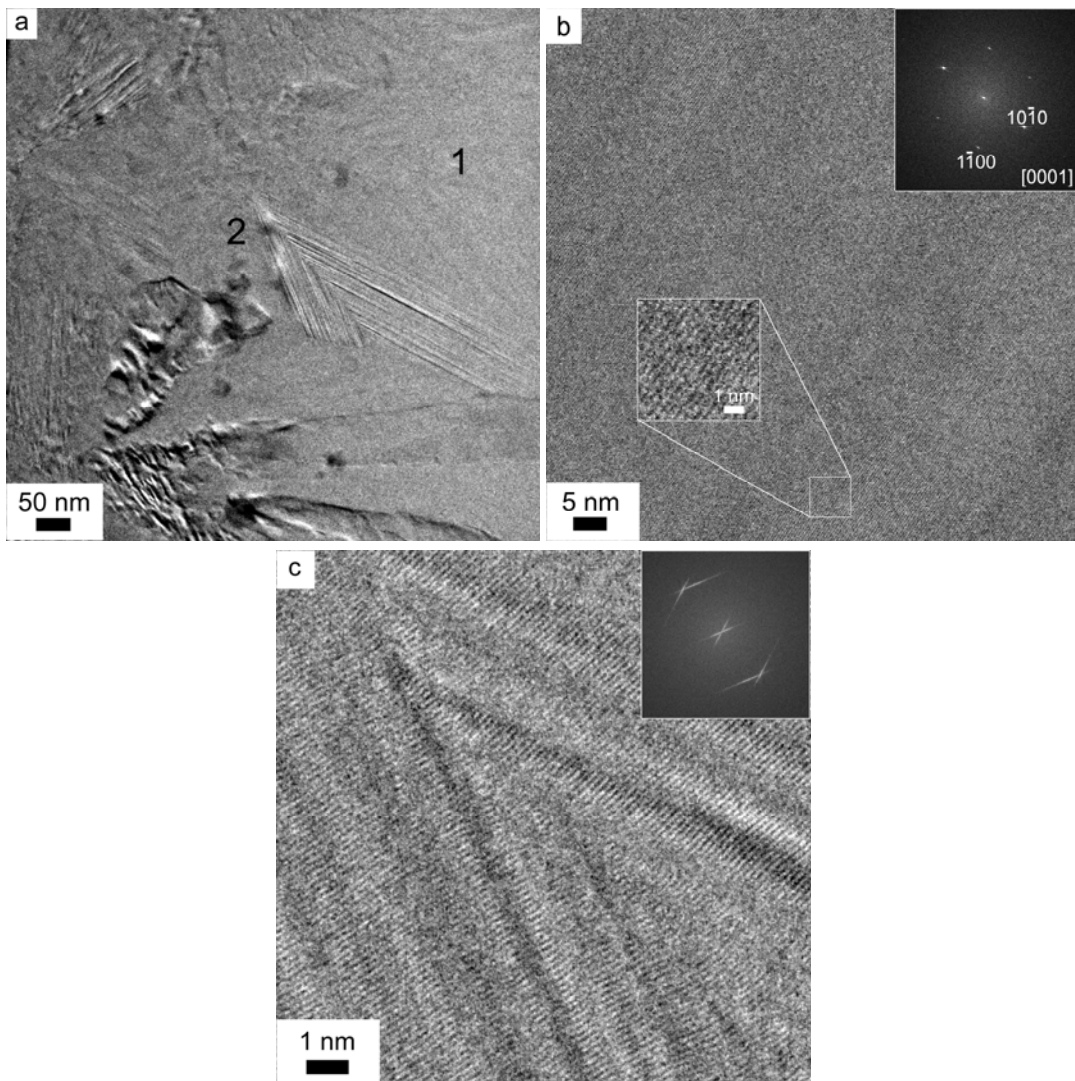


**Figure 3.5:** Cryo-TEM image of sample C was acquired after the exposure to the electron beam for ~8 minutes. Two features noted as 1 and 2 are further shown in (b) and (c). Image with FFT inset in (b) shows a [0001]-oriented single-crystalline  $I_h$ . A square area is magnified to reveal  $\{10\bar{1}0\}$ -type lattice fringes. The central part of the region 2 is magnified in (c); two sets of  $\{10\bar{1}0\}$ -type planes intersect each other at  $40^\circ$ .

forming a ring in FFT have originated from the crystalline ice ( $d \sim 3.7 \text{ \AA}$ ). Although the possibility of spots “P” to be Moire fringes cannot be neglected, the particle morphology and the most general d-spacing, indicating it to be a MFI crystal, cannot be overlooked.

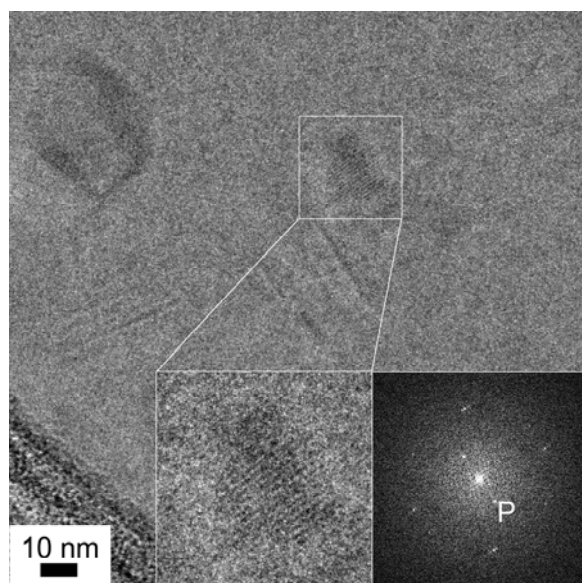


**Figure 3.6:**A cryo-TEM image of sample D with a square region magnified in the bottom. The FFT inset from the square region consist a ring of spots corresponding to 3.7 Å. There is a set of spots (noted as P) which may correspond to MFI-type framework (d-spacing ~9.6 Å).

This example illustrates that it is very important to be careful while performing analysis of cryo-TEM images.

### 3.4 Conclusion

The present study demonstrates that high-resolution cryo-TEM imaging of zeolite crystallites is possible while maintaining the solution microstructure. It also reports some of the associated challenges with the cryo-TEM technique such as the transformation of vitreous ice to its crystalline form. The lattice fringes due to crystalline ice may interfere with the structure of the original sample.

#### ACKNOWLEDGEMENTS

Sample B was provided by Xueyi Zhang and Pyung-Soo Lee.

---

## A STRUCTURAL RESOLUTION CRYO-TEM STUDY OF THE EARLY STAGES OF MFI GROWTH<sup>¥</sup>

In this chapter, we present a study of MFI nucleation and early stages of MFI growth in (tetrapropylammonium) TPA-silica sol primarily by cryogenic-transmission electron microscopy (cryo-TEM) to elucidate MFI nucleation and early stages of growth. Small-angle x-ray scattering (SAXS) and (non-cryogenic) high-resolution transmission electron microscopy (HRTEM) are employed as the complementary techniques. The present results show that the nuclei and early aggregates ( $C_x$ ,  $x < n$  in Figure 1.5) do not need to have well-developed MFI structure. MFI nucleation and crystallization follows the formation of amorphous aggregates.

---

<sup>¥</sup>Results presented in this chapter are published in

S. Kumar *et al.*, *J. Amer. Chem. Soc.*, **2008**, 130 (51), 17284

#### 4.1 Introduction

Understanding nucleation and growth phenomena in solution remains elusive partly due to the challenges involved in available sample preparation and characterization techniques. Such phenomena are of fundamental and practical significance for the synthesis of various materials including zeolites and other templated porous materials.<sup>7,14,15,21-23,37,79-83</sup> In this context, the synthesis of pure silica MFI (TPA-silicalite-1; hereafter referred to as MFI), in optically clear sols, has been studied extensively as a model system.<sup>2,25,29,84-86</sup> The synthesis mixture is prepared from tetraethylorthosilicate (TEOS), water, and tetrapropylammonium hydroxide (TPAOH). Upon hydrolysis of TEOS, nanoparticles with typical size ~5 nm form spontaneously.<sup>2</sup> The nature of these nanoparticles and their role in early stages of MFI growth is still under debate.<sup>2,87,88</sup> In 2006, group at the University of Minnesota proposed a mechanism for the early stages of MFI growth.<sup>17,89</sup> It includes evolution of precursor nanoparticles to nuclei and crystal growth by aggregation of a fraction of the evolving nanoparticles (model depicted in Figure 1.5). The precursor nanoparticles (denoted A) are known to initially have a disordered silica-core/TPA-shell structure.<sup>29</sup> We hypothesized that they evolve through intermediates (denoted B<sub>1</sub> to B<sub>m</sub>) to nuclei C<sub>1</sub>. A unique aspect of the proposed mechanism is that intermediate nanoparticles B<sub>1</sub> to B<sub>m</sub>, although not yet fully transformed to MFI, can contribute to aggregation with different rates of attachment. This distributed population of nanoparticles, exhibiting diversity towards aggregative crystal growth,<sup>17</sup> was proposed in order to explain the prolonged induction period observed in MFI nucleation and the presence of relatively large crystals at low yield at the early stages of crystal growth. The proposed mechanism was based on the characterization of room temperature aged TPA-silica sol by a number of techniques such as atomic force microscopy (AFM), small-angle X-ray scattering (SAXS), and high-resolution transmission electron microscopy (HRTEM) and a phenomenological population balance mathematical model. Although room temperature aging may not be practical for commercial production of MFI, it enabled us to capture the complex steps involved in

zeolite crystallization by ensuring slow evolution and avoiding complications that may be introduced during quenching before characterization. However, information regarding the structure of intermediate nanoparticles ( $B_1$  to  $B_m$ ), nuclei ( $C_1$ ) and early aggregates ( $C_x$ ) is still very limited since they are minor components of the sols at early stages of growth.

Here, we present a cryogenic transmission electron microscopy (cryo-TEM) study on sols, with similar composition to those studied previously,<sup>17</sup> prior to and during the early stages of MFI formation. Although cryo-TEM was employed in chapter 2, it was limited only to the characterization of nanoparticles. In the present study, cryo-TEM images with structural resolution are obtained and yield new insights in MFI growth. SAXS, (non-cryogenic) HRTEM and N<sub>2</sub> adsorption-desorption are also employed as complementary characterization techniques. The TPA-silica sol used has a molar composition 20SiO<sub>2</sub>/9TPAOH/9500H<sub>2</sub>O/80C<sub>2</sub>H<sub>5</sub>OH and corresponds to relatively small excess of silica beyond its solubility limit. It is one of the most dilute compositions that nucleate MFI and is used here because it is known to yield MFI crystals at room temperature over reasonable time scale (i.e. ~7 months). This slow time-frame is ideal for attempting to discern structural differences in the evolving particles just before and during the early stages of crystal growth. At higher temperatures, the transition from isolated primary particles to MFI crystals occurs over days (ca. 40 °C) to hours (ca. 80 °C) for this silica sol composition. We believe that other more concentrated sols could also be studied using cryo-TEM to obtain images with structural resolution.

## 4.2 Experimental Methods

### 4.2.1 Synthesis

TPA-silica sol was prepared by combining TPAOH (Aldrich, 1.0 M in water), TEOS (Aldrich, 98%) and DI water with molar compositions:



The sol was stirred for ~24 h to complete the hydrolysis of TEOS, filtered (0.45 µm syringe filter) into multiple Teflon-coated bottles, and then sealed with paraffin film. The sols were periodically characterized by SAXS and cryo-TEM. Some sol samples were dialyzed following the characterization by SAXS and (non-cryogenic) HRTEM.

#### **4.2.2 Small Angle X-ray Scattering**

The detection of the onset of aggregation could be accomplished by dynamic light scattering (DLS) and/or SAXS.<sup>17,18,90</sup> Here we use SAXS because it can capture the very early stages of aggregation without uncertainties due to dust contamination and can effectively monitor the aggregate and PN populations simultaneously. The SAXSess SAXS instrument (Anton-Parr) was employed to characterize fresh and aged S1 sols. Sols were loaded into a vacuum-tight 1 mm quartz capillary. This instrument is equipped with a Cu-K<sub>α</sub> slit-collimated radiation source. Slit collimation is beneficial in that a larger volume of sample is illuminated at once and therefore data collection time may be significantly reduced without a reduction in measured intensity. However, the scattering profile produced from a line collimated beam will be “smeared” due to the incident beam geometry, an effect that can be accounted for during data analysis using the software program, Generalized Indirect Fourier Transform (GIFT).<sup>91,92,55</sup> The scattering vector  $q$  was determined from the scattering angle  $\theta$  through use of the relationship:  $q=4\pi \lambda^{-1} \sin(\theta/2)$ . In all instances, measurements were made at room temperature (~25 °C).

#### **4.2.3 Cryogenic Transmission Electron Microscopy**

Specimens were prepared by transferring a small drop of TPA-silica sol on to a holey carbon coated TEM grid (Ted Pella Inc.) without any sol alteration. The droplets were thinned to a film by gently blotting with filter paper. Immediately after thinning, the specimen was plunged into liquid ethane and then quickly moved to a liquid nitrogen reservoir. Details of the procedure are given by Talmon.<sup>93</sup> Resultant vitrified specimens were transferred to a Gatan 613.DH Cooling Holder (-180 °C) under liquid nitrogen. The

imaging was performed at -178 °C using a FEI Tecnai G2 F30 TEM operated at 300 kV. The microscope has a twin-pole piece with point to point resolution of 0.24 nm and enabled the acquisition of images with structural resolution.

#### 4.2.4 Transmission Electron Microscopy

TEM specimens were prepared by placing a few droplets onto an ultrathin holey-carbon coated grid (Ted Pella, Inc.). Dialyzed sols were diluted in ethanol prior to specimen preparation. Specimens were then allowed to air-dry. TEM characterization was performed using FEI Tecnai G2 F30, operating at 300 kV.

### 4.3 Results and Discussion

Room temperature aging of clear TPA-silica sols was monitored using the SAXSess instrument, and the SAXS patterns are shown in Figure 4.1. Scattering intensity increases with aging time indicating an increase in the size of nanoparticles, which can be accounted for structural reorganization as proposed before.<sup>17</sup> SAXS data (Figure 4.1)

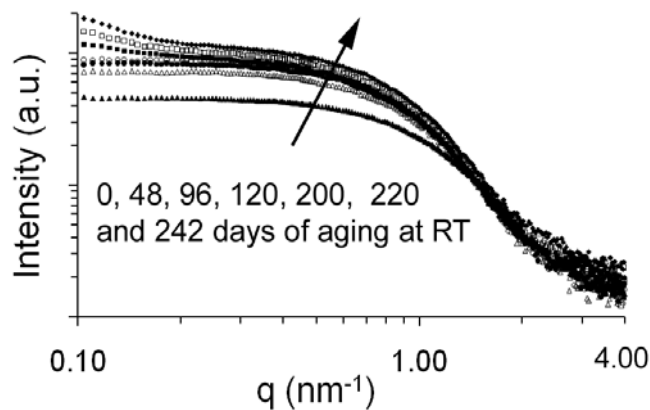


**Figure 4.1:** SAXS scattering profiles from TPA-silica sols after various times at room temperature.

show the presence of ca. 5 nm precursor nanoparticles and the emergence of a second population of larger particles (evident by the rise in the low- $q$  scattering intensity) after about 200 days, in agreement with the previous report.<sup>17</sup> Representative cryo-TEM data of the sols after the detection of larger particles (200 days) are shown in Figure 4.2(a). A small number (by comparison to precursor nanoparticles) of aggregate-like larger particles (30-50 nm), indicated by arrows, are present in a sea containing dark dots (contrast due to the ca. 5 nm precursor nanoparticles). The magnified image of an aggregate is shown in Figure 4.2(b). The Fast Fourier Transform (FFT), shown in the inset shows no evidence for crystallinity in these aggregate-like particles. Twenty such aggregates were examined, and no evidence of crystallinity was observed. Their stability under the beam suggests that these features are not artifacts due to surface contamination but rather the silica particles responsible for the low  $q$  scattering intensity in the SAXS data. This was also suggested by the location of these particles inside the vitrified sol rather than on its surface. We conclude that the larger particles detected by SAXS (here, after 200 days) and denoted by  $C_x$  ( $x < n$ ) in Figure 1.5) are predominantly amorphous. This new finding could not be obtained in our previous work employing conventional (non-cryogenic) TEM and dialysis for sample preparation because, most likely, the aggregates dissolved during dialysis.<sup>17,89</sup>

A representative cryo-TEM image of the sol after 220 days is shown in Figure 4.2(c). Again, as expected from the SAXS data, larger particles as well as precursor nanoparticles are present. In contrast to the aggregates observed in specimens collected after 200 days, the aggregates observed at 220 days exhibit lattice fringes consistent with the MFI crystal structure (Figure 4.2(d)). White lines serve to highlight the crystal perimeter and indicate the absence of well developed facets. The FFT (inset of Figure 4.2(d)) indicates that the crystal is oriented either along the [100]- or [010]-axis, with the dots inside the highlighted perimeter representing the sinusoidal or straight MFI channels. Ten of such particles were closely inspected. To our knowledge, this is the first time such resolution has been achieved for zeolites imaged in the parent sol by cryo-TEM. The

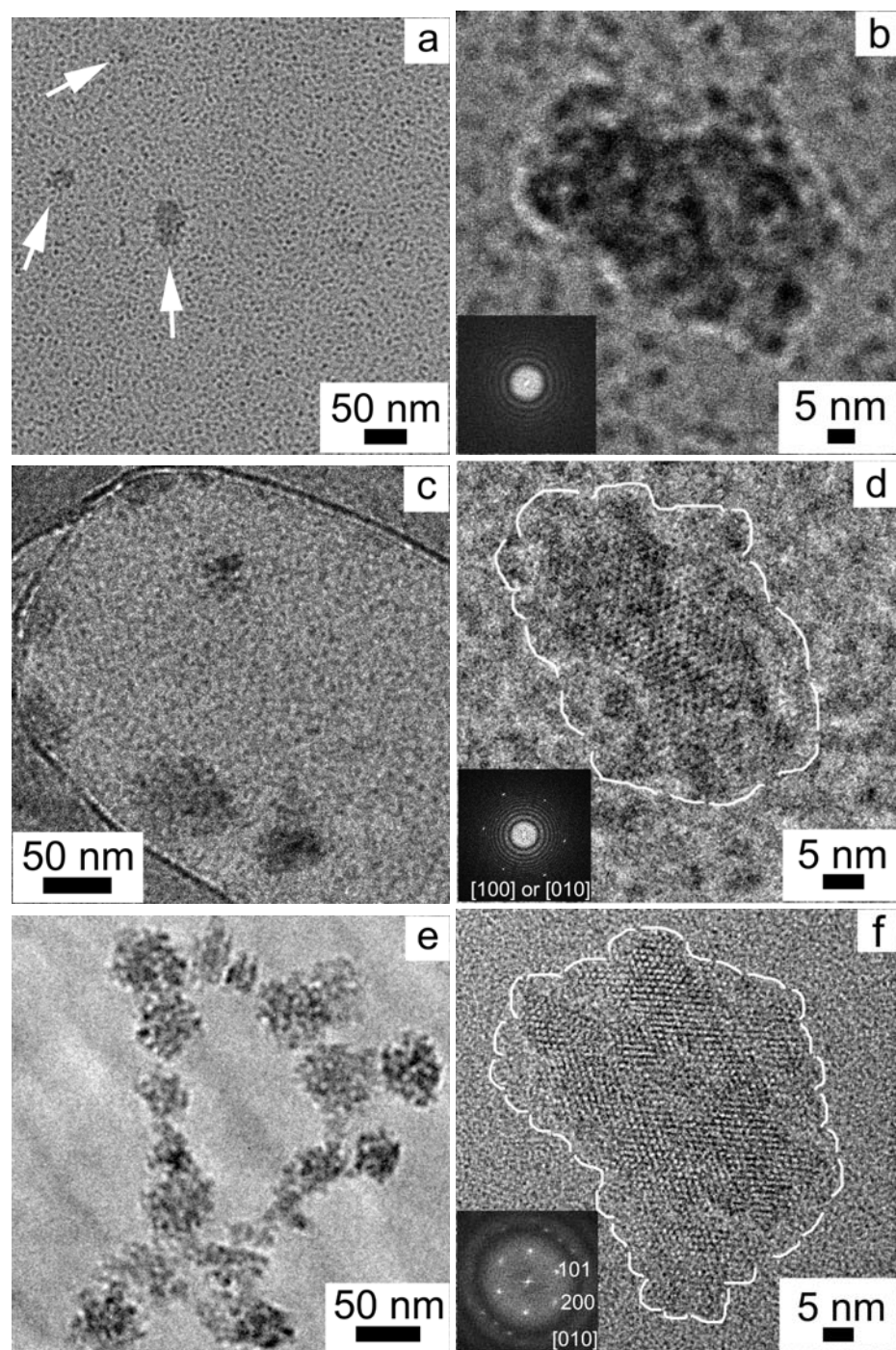


**Figure 4.2:** (a) A representative cryo-TEM image of the sol kept for 200 days at room temperature. A magnified image of a representative aggregate with FFT inset is shown in (b). (c) A cryo-TEM image of sol after 220 days; a high-resolution cryo-TEM image of a representative crystal with FFT inset is shown in (d). A cryo-TEM image of dialyzed sol after 220 days is shown in (e). A conventional (non-cryogenic) TEM image of a dry crystal isolated from the dialyzed sol is shown in (f).

crystals do not have the typical MFI morphology. Instead they are aggregate-like and are in the similar size range (~30-50 nm) as the predominantly amorphous aggregates shown in Figures 4.2(a)-(b). This observation suggests that the particles observed at ~200 days continue to transform and give rise to MFI crystals sometime between 200 and 220 days (a relatively short period). This observation adds a new element to the aggregation mechanism we have proposed before (Figure 1.5) in that early aggregates ( $C_x$ ) do not have, to say the least, a well developed MFI structure. The transformation takes place in a relatively short period of time. However, we cannot state if it is a sudden or gradual transformation, nor if it is taking place simultaneously or starts localized and propagates through the particle. More in-depth studies with improved time resolution as well as sol characterization by other techniques, such as nuclear magnetic resonance (NMR),<sup>94</sup> mass spectroscopy (MS)<sup>95</sup> and infrared spectroscopy (IR)<sup>96</sup> are required to further elucidate the zeolite nucleation events.

One of the challenges, we faced in the present work, was due to very low aggregate and crystal yield (< 5%) imposed by our desire to observe the very first nucleation and growth events. The low aggregate and crystal yield made it difficult to find particles other than the 5 nm precursor nanoparticles on the TEM grid. Furthermore, high-resolution imaging requires an incident electron beam on a relatively smaller area of the sample. So, there is fair chances that while imaging a certain crystallite other nearby ones are amorphized. Therefore, although we can state with certainty the presence of only predominantly amorphous aggregates in 200 days, we cannot make similar strong statements regarding the co-existence of amorphous with crystalline aggregate-like particles in 220 days aged sols.

We further examined the sols containing MFI crystals (220 days) after using a dialysis procedure previously reported<sup>17</sup> so as to isolate MFI crystals from precursor nanoparticles and dissolved species. SAXS patterns from the original and dialyzed sol are shown in Figure 4.3. A representative cryo-TEM image from the dialyzed sol is shown in Figure 4.2(e). The SAXS pattern agrees with the cryo-TEM observation; i.e., only the

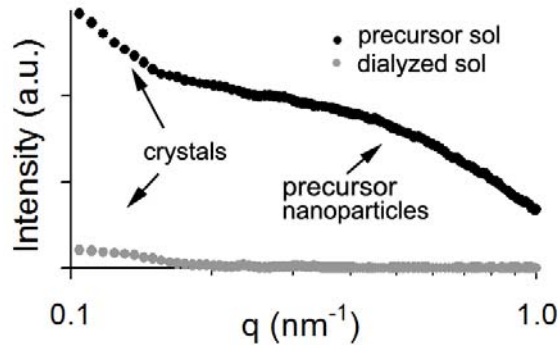


**Figure 4.3:** SAXS patterns from the original and dialyzed sols after 220 days at room temperature.

larger particles are present in the dialyzed sol. Moreover, crystals in the dialyzed sol exhibit characteristic swiss-cheese morphology while voids are not evident in the crystals present in the original sol. For comparison, a high-resolution conventional (non-cryogenic) TEM image of a (dry) crystal isolated from the dialyzed sol is shown in Figure 4.2(f). White lines serve to highlight the crystal perimeter. The FFT, shown in the inset, shows that the crystal is oriented along the [010]-axis. We attribute the voids created by dialysis to the dissolution of partially transformed regions distributed within the crystals. SAXS may not detect a change in the particles due to the formation of such voids because the overall size and shape of the post-dialysis crystals is similar to those of the pre-dialysis aggregates. In this respect, the statement that was made previously:<sup>17</sup> “SAXS analysis indicated that the crystals are not affected significantly by the dialysis procedure” is not precise as now we have clear evidence that dialysis results in the partial dissolution of the aggregates. However, the presence of such regions is in agreement with the mechanism proposed: aggregative MFI growth by attachment of ~5 nm nanoparticles that do not have a well developed structure.<sup>17</sup>

#### 4.4 Conclusion

TPA-silica sols are followed primarily by cryo-TEM for MFI nucleation and growth from solution. Conventional (non-cryogenic) TEM and SAXS are employed as complementary techniques. The importance of this study is two-fold. First, it provides evidence supporting the previously proposed mechanism of evolution of nanoparticles followed by aggregative crystal growth while adding a new element. The new element, not included in the previously proposed model, is the formation of predominantly amorphous aggregates before MFI crystallization and points to the importance of intra-aggregate rearrangements in nucleation and growth.<sup>37,52</sup> Second, it demonstrates that, in addition to metal nanoparticles,<sup>78</sup> electron-beam sensitive materials such as zeolites can be imaged by cryo-TEM with structural resolution in their parent sols. Similar studies for other zeolites under different conditions may reveal useful structural information for the understanding of hydrothermal nucleation and growth.

#### ACKNOWLEDGEMENTS

The author would like to thank Zhuopeng Wang for SAXS data shown in Figure 4.1.

---

## MFI NUCLEATION AND CRYSTALLIZATION IN SILICA SOLS

In this chapter, TPA-silica sols were studied by a combination of small-angle x-ray scattering (SAXS), transmission electron microscopy (TEM), cryogenic TEM (cryo-TEM), and N<sub>2</sub> adsorption-desorption. Results are consistent with the hypothesis that amorphous aggregates of nanoparticles form prior to MFI crystallization. Once the onset of crystallization had occurred, the aggregates were observed to be composed of both crystalline and amorphous regions, indicating that crystallization was likely nucleated within the initially amorphous aggregates.

### 5.1 Introduction

The growth of all-silica MFI (tetrapropylammonium (TPA)-silicalite-1; hereafter referred to as MFI) in optically clear TPA-silica-water sols is often studied as a model system to elucidate zeolite nucleation and growth.<sup>2,18,29-31,97</sup> The synthesis mixture is prepared by mixing tetraethylorthosilicate (TEOS) in an aqueous solution of TPAOH. Precursor nanoparticles (PNs), typically ~5 nm in size, form spontaneously upon hydrolysis of TEOS.<sup>2,98</sup> Researchers differ in ideas regarding the nature of the PNs (ordered vs disordered) and their role (nutrients vs direct participant) in MFI growth.<sup>2,87,88</sup> As discussed in chapter 1, Minnesota group proposed a mechanism of early stages of MFI growth that includes the structural evolution of PNs from their initially amorphous state, denoted A, to a fully crystalline state, denoted C<sub>1</sub> (Figure 1.5).<sup>17</sup> The initial PNs (A) are known to have disordered silica-core/TPA-shell structures.<sup>29</sup> The PNs evolve through intermediates (denoted B<sub>1</sub> to B<sub>m</sub>) to the crystalline state, C<sub>1</sub>. The unique aspect of the mechanism is that the structurally evolving nanoparticles ((B<sub>1</sub> to B<sub>m</sub> in Figure 1.5), although not yet fully crystalline, contribute to crystal growth by aggregation with increasing probability as their structure becomes more and more similar to the MFI

crystal structure. This structurally diverse population of nanoparticles explains the prolonged induction period, the broad size distribution of crystals, and the presence of larger crystals at low yield during the early stages of MFI growth.<sup>17</sup>

An ongoing challenge is the direct characterization of the nature of PNs and aggregates as they exist in the growth medium. In chapter 2,<sup>17,89</sup> transmission electron microscopy (TEM) was performed on MFI crystals after a two-step dialysis procedure. The dialysis procedure enabled separation of the crystals from dissolved silica species, PNs, and excess TPA ions, species that would otherwise lead to precipitation during the TEM specimen preparation.<sup>17</sup> In contrast, one can obtain images of crystalline material after the dialysis procedure.<sup>17,89</sup> An example TEM image of MFI crystals obtained from non-dialyzed TPA-silica sol is shown in Figure 5.1(a). It is evident that considerable material is deposited as the sol dried on the TEM grid. On the contrary, one can obtain images showing only crystals after the dialysis procedure (Figure 5.1(b)). The results shown in Figure 5.1 are from a TPA-silica sol similar to the chapter 4 but heated at 50 °C

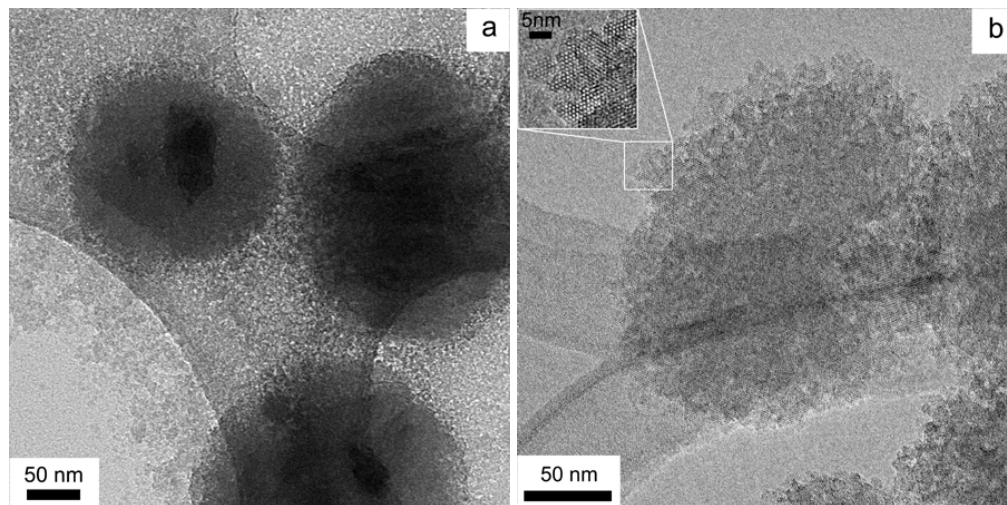


**Figure 5.1:** TEM image of the materials obtained on a TEM grid by depositing from (a) TPA-silica sol and (b) the same sol after the dialysis procedure.

(instead of room temperature) for 17 days. A square area in Figure 5.1(b) is magnified and shown in the inset to reveal straight channels of MFI framework, which appear as bright dots. Important conclusions regarding the aggregate-like morphology of MFI crystals were made based on the TEM characterization of the dialyzed sols.<sup>17,89</sup> Unfortunately, neither approach produces TEM specimens that can provide true representations of the state of the growing particles *in situ*. Cryogenic TEM (cryo-TEM) enabled direct characterization of suspensions. Results in chapter 4 demonstrated that the aggregate-like MFI crystals were indeed altered by the dialysis procedure, demonstrating that less ordered regions were dissolved from the MFI during the dialysis procedure. The results lent strong support to the hypothesis that growth involves a structurally diverse population of PNs with the probability of contributing to aggregation increasing as the PN structure approached that of the MFI crystal structure.<sup>99</sup> Open questions regarding MFI nucleation remain. Several possibilities include: evolution of PNs to crystalline MFI, with subsequent aggregation of intermediate PNs ( $B_1$  to  $B_m$  in Figure 1.5) and continued structural evolution towards the MFI crystal structure; aggregation of intermediate PNs with subsequent phase transformation initiated either within the core or at the surface of the aggregate; aggregation of intermediate PNs with phase transformation initiated upon addition of MFI-like PNs ( $C_1$  in Figure 1.5). What the chapter 4 demonstrated is that the formation of aggregates precedes MFI nucleation and crystallization, and crystals contain disordered regions within them (suggesting involvement of the structurally distributed population of PNs in crystal growth). The goal of this chapter is to image these aggregates at the earliest stage of crystallization possible.

Here, we report the use of cryo-TEM combined with (non-cryogenic) HRTEM on TPA-silica sols, before and after the dialysis procedure, to image the earliest stage of crystallization. The working hypothesis is that small crystalline domains exist within the aggregates but that these aggregates have heretofore escaped detection by cryo-TEM due to technique limitations. If such crystalline domains exist, they could be exposed after the

dialysis procedure as disordered regions would dissolve away due to higher solubility as compared to the crystalline domains.

## 5.2 Experimental Section

### 5.2.1 Synthesis

Silica sols were prepared by combining TPAOH (Aldrich, 1.0 M in water), tetraethylorthosilicate (TEOS; Aldrich, 98%), and DI water with final molar compositions  $20\text{SiO}_2/9\text{TPAOH}/9500\text{H}_2\text{O}$ . The sols were stirred for ~24 h to complete the hydrolysis of TEOS, filtered (0.45  $\mu\text{m}$  syringe filter) into multiple Teflon-coated bottles, and then sealed by wrapping paraffin film around the caps. Bottles containing sols were either left at room temperature or heat-treated at 40 °C by submerging them in oil baths. Sols were periodically sampled for characterization by SAXS, TEM, and cryo-TEM.

### 5.2.2 Crystal Isolation by Two-Step Dialysis and Centrifugation

To separate crystalline zeolite particles from PNs, dissolved silica and TPA ions present in the sol, the two-step dialysis procedure described previously was employed.<sup>17</sup> First, the sol was transferred to a rinsed dialysis bag (Spectra Por 3 purchased from Spectrum Laboratories). After sealing the bag, it was placed in a 1-liter polypropylene (PP) beaker containing 6 ml of 1.0 M TPAOH and 1 liter of water (pH ~ 11.5). Dialysis against TPA/water is allowed to continue until the PN concentration falls below the detection limit (by SAXS). During the second step, the suspension was dialyzed against water in a clean 1-liter PP beaker, and the bag was rotated by magnetic stirring. Progress was monitored by measuring the pH outside the bag. The dialysis water was exchanged for fresh water about every 12 hours. The second dialysis step was complete when the pH stabilized at ~8 (after ca. 48 hours).

Centrifugation was performed at 15000 rpm for 20 minutes. The supernatant was removed after centrifugation and fresh DI water added. The procedure was repeated until the sol pH dropped to ~7 (six to eight times total). Hereafter, samples are referred to as PS (precursor sol), DS (sol after the two-step dialysis procedure), or CDP (particles collected using the centrifugation of precursor sol followed by drying at 60 °C).

### 5.2.3 Small Angle X-ray Scattering

The detection of the onset of aggregation was accomplished by SAXS using the SAXSess SAXS instrument (Anton-Parr). Each sol was loaded into a vacuum-tight 1 mm quartz capillary. The SAXSess is equipped with a Cu-K<sub>α</sub> slit-collimated radiation source. Slit collimation is beneficial in that a larger volume of sample is illuminated at once, and therefore the data collection time may be significantly reduced without a reduction in measured intensity. However, the scattering profile produced from a line-collimated beam will be “smeared” due to the incident beam geometry, an effect that can be accounted for during data analysis using the software program, Generalized Indirect Fourier Transform (GIFT).<sup>91,92,55</sup> The scattering vector  $q$  was determined from the scattering angle  $\theta$  based on the relationship:  $q = 4 \pi \lambda^{-1} \text{Sin}(\theta/2)$ . Measurements were made at room temperature (~25 °C) in all instances.

### 5.2.4 Cryogenic Transmission Electron Microscopy

Specimens were prepared by transferring a small drop of the PS or DS on to a holey-carbon coated TEM grid (Ted Pella Inc.) in a controlled environment vitrification system (CEVS).<sup>68</sup> The droplets were thinned to a film by gently blotting with filter paper. Immediately after thinning, the specimen was plunged into liquid ethane and then quickly moved to a liquid nitrogen reservoir. Each vitrified specimen was transferred to a Gatan 613.DH cooling holder under liquid nitrogen. The imaging was performed at -180 °C using either a 300 kV FEI Tecnai G2 F30 or 120 kV JEOL 1210 TEM. The FEI Tecnai G2 F30 has a twin-pole piece with point to point resolution of 0.24 nm and enabled the acquisition of images with structural resolution.

The cryo-TEM technique imposes certain challenges, such as frost-formation, specimen-drift and film-thickness control.<sup>67-69</sup> The silica sols used here and in chapter 4 are just above the silica solubility limit, which make them amongst the most dilute compositions to nucleate MFI. The dilute composition combined with the goal of characterizing samples prior to nucleation and during earlier stages of growth made the detection of the particles a major challenge. Assuming 100% yield, the zeolite volume fraction would be only 0.32%. At the small yield studied here, the volume fraction is well under 0.02%. The absence of well-defined crystal morphology during earlier stages of growth can also make distinguishing these particles from artifacts in cryo-TEM (e.g. the presence of frost particles, which can form during sample transfer in a humid environment) difficult.

A major issue in the present study is the lack of substantial contrast due to the vitreous film thickness;<sup>70</sup> if the crystallites under investigation are too small, then the film-thickness will make discerning particles embedded within that thin film impossible. In order to test whether 20 nm crystallites could be imaged at high-resolution, 20 nm MFI crystals in water was imaged. Figure 5.2(a) shows a cryo-TEM image of these particles, and this representative image demonstrates that high-resolution imaging of such particles is indeed practical. However, we cannot conclude if these observed particles are smaller or imperfect. The 20 nm MFI particles were synthesized by confined growth<sup>77</sup> and the cryo-TEM sample was prepared by dispersing the zeolite powder in DI water followed by vitrification. The spots in FFT inset correspond to either  $d_{\{101\}}$  or  $d_{\{200\}}$  ( $\sim 9.8 \text{ \AA}$ ) of MFI framework structure. For a comparison, a conventional (non-cryogenic) TEM image of similar MFI crystals, with inset HRTEM image of one b-oriented MFI crystal, is shown in Figure 5.2(b). Finally, zeolites are highly electron-beam sensitive materials,<sup>54,65,66</sup> which means that very little time is available for optimizing microscope conditions and/or particle orientation before the crystalline nature of the particle is lost.

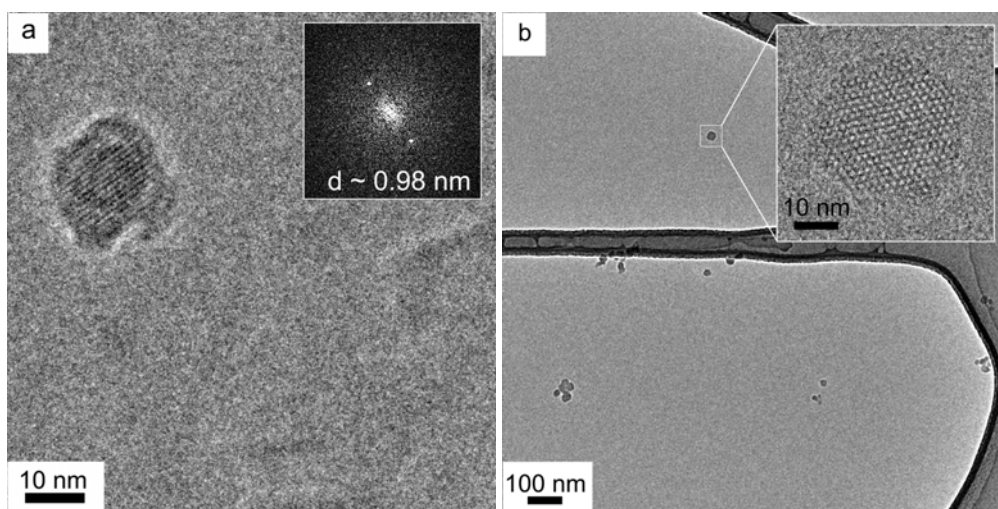


**Figure 5.2: 20 nm sized MFI crystals observed by (a) cryo-TEM and (b) TEM.**

### 5.2.5 Transmission Electron Microscopy

TEM specimens were prepared by placing a few droplets of DS after dilution with ethanol or a few droplets of PS (no dilution) onto ultrathin holey-carbon coated grid (Ted Pella, Inc.) and the grids were allowed to air-dry. CDP specimens were prepared by dry mounting, which involved sprinkling the powders onto the TEM grid. TEM characterization was performed using FEI Tecnai G2 F30, operating at 300 kV and equipped with a charge-coupled device (CCD) camera.

### 5.2.6 Nitrogen Adsorption-Desorption

An Autosorb-1 analyzer (Quantachrome Instruments) was employed to measure the Nitrogen adsorption–desorption at 77 K. The specific surface area was calculated using the Brunaer–Emmett–Teller (BET) method. The samples were degassed at 200 °C and 1 mm Hg for 2 hours to remove the adsorbed moisture prior to the autosorb experiment.

## 5.3 Results and Discussion

### 5.3.1 The Presence of Crystalline Domains within Aggregates

Representative cryo-TEM images of TPA-silica sols heat-treated at 40 °C shown in Figures 5.3(a)–(d). Amorphous aggregates were first observed after six days (Figure 5.3(a)) and the first evidence of crystalline MFI was detected after 21 days (Figure 5.3(d)). Qualitatively, the sequence of events at 40 °C is similar to that observed for the sols aged at room temperature (chapter 4), while time to detection of the aggregates is much shorter (6 d at 40 °C versus 200 d at room temperature). As with previous work, this implies that the mechanism does not change significantly with the change in temperature.<sup>89</sup>

Representative TEM images of samples collected from the TPA-silica sol heat treated at 40 °C and subjected to the dialysis procedure are shown in Figures 5.4(a)–(c). The first evidence of crystallinity was observed after 9 days (Figure 5.4(a)), and the size and number of MFI crystallites increased with heating time. The observation of crystalline material prior to its first detection in the cryo-TEM images of the PS samples suggests that MFI fragments may be hidden within at least some of the aggregates observed after 9 days (Figures 5.3(b) and 5.3(c)) and the aggregates<sup>99</sup> observed after 200 d at room temperature. The average size of 10-25 particles was determined from the calibrated images and plotted in Figure 5.4(d). The crystallite size in the DS samples is always smaller than the aggregate size of the PS samples. Furthermore, the crystal growth appears faster than the aggregate growth, although Figure 5.4(d) is based on relatively few measurements due to the low concentration of aggregates and crystallites at this early stage. This study suggests that the MFI nucleation is localized somewhere within the aggregates and that crystallization gradually proceeds to finally transform the entire aggregate. There are few reports in the literature regarding the importance of internal restructuring of the aggregates in zeolitic nucleation and crystallization.<sup>37,100-102</sup> However, the present results give the first evidence of the formation of amorphous

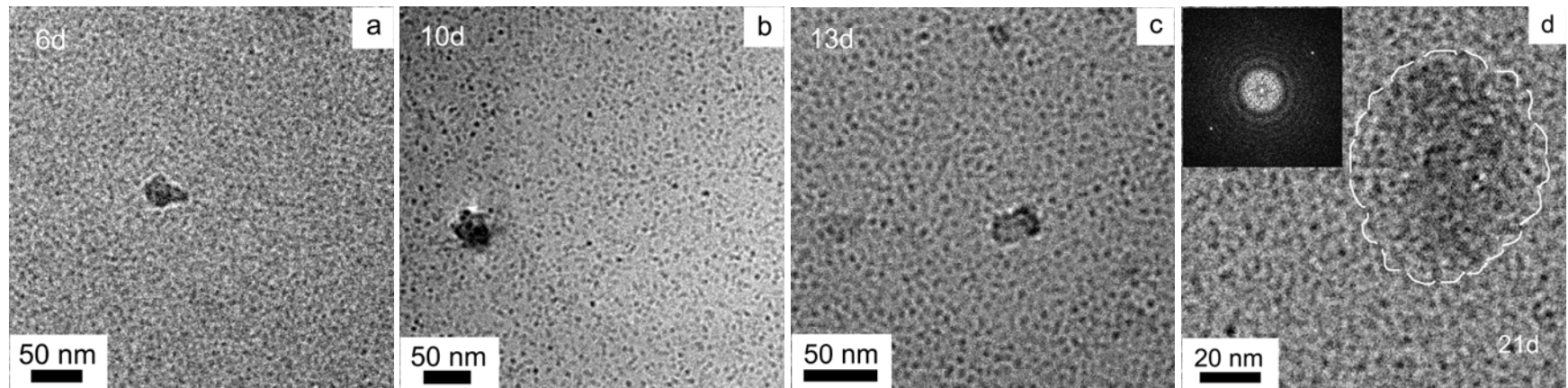


Figure 5.3: Cryo-TEM images of TPA-silica sols heated at 40 °C for (a) 6d-PS, (b) 10d-PS, (c) 13d-PS and (d) 21d-PS.

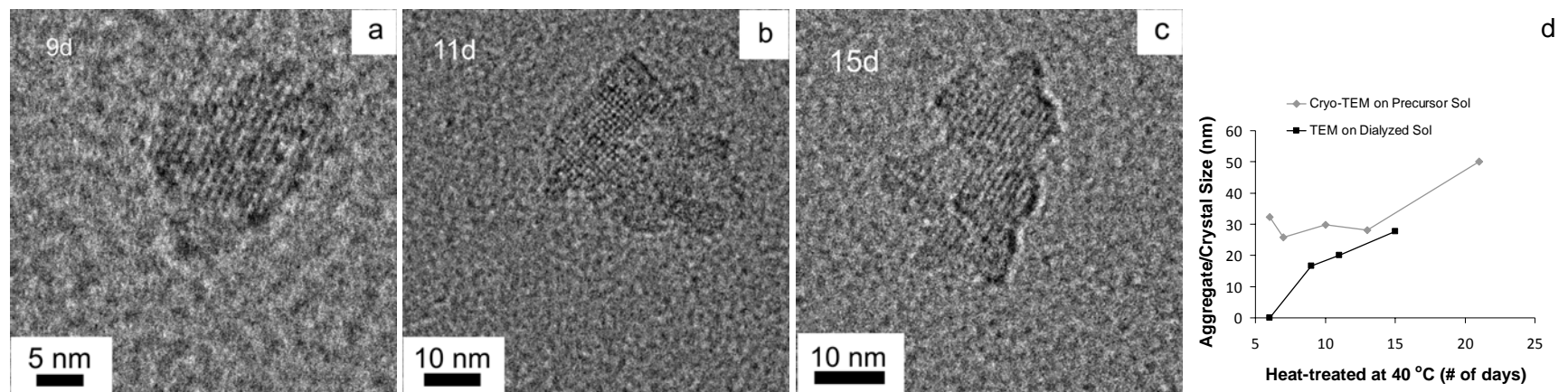
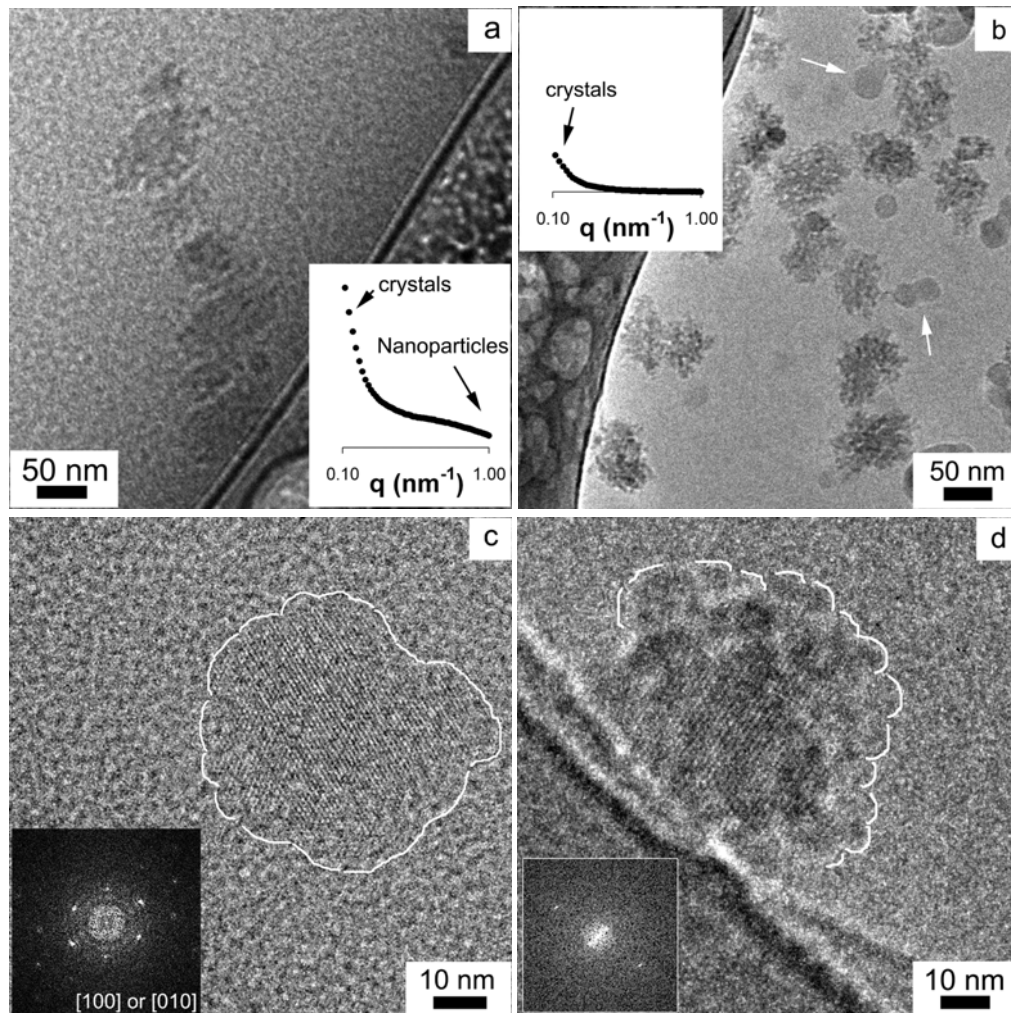


Figure 5.4: TEM images of TPA-silica sols heated at 40 °C for (a) 9d-DS, (b) 11d-DS and (c) 15d-DS. (d) A plot showing the average size of particles as a function of heating time.

aggregates followed by internal ordering as the essential steps in MFI nucleation. Nevertheless, we cannot state if MFI nucleation occurs inside the amorphous aggregate or at the aggregate-solution interface.

### 5.3.2 Aggregation of Evolving Nanoparticles

Results in chapter 4 examining MFI crystal growth at room temperature supported the hypothesis of evolving nanoparticles (noted as  $B_1$ - $B_m$  in Figure 1.5) with ever increasing probability of aggregation. The formation of aggregates composed of structurally diverse nanoparticles, even after MFI nucleation occurred, was confirmed by comparing cryo-TEM and TEM images of PS and DS samples. The disordered or less-crystalline regions dissolved away during the dialysis procedure owing to their higher solubility as compared to crystalline MFI. One more set of results for TPA-silica sols aged at room temperature for 390 d is shown in Figure 5.5. A representative cryo-TEM image of 390 d-PS is shown in Figure 5.5(a). MFI crystals (30-80 nm) are present in a sea of PNs ( $\sim 5$  nm). The SAXS data, shown in the inset, agrees with the cryo-TEM observation, i.e., both PNs and larger particles are present in the PS. A representative cryo-TEM image of the 390d-DS, with inset SAXS data, indicating the presence of only larger particles is shown in Figure 5.5(b). Crystals in both the PS and DS do not have faceted morphology and have aggregate-like appearance. However, crystals in the DS are more open with swiss-cheese appearance while the voids are absent in the crystals in the PS. Frost particles are indicated by arrows in Figure 5.5(b). The observed differences were further investigated by high-resolution cryo-TEM. Representative images for PS and DS are shown in Figures 5.5(c) and 5.5(d). White lines serve to highlight the crystal perimeter. FFT inset indicates that the MFI crystal in 5.5(c) is oriented either along the a- or b-axis. The swiss-cheese appearance of crystals in the DS in Figure 5.5(b) results in a contrast modulation in the high-resolution image (Figure 5.5(d)). This contrast modulation is probably due to the formation of voids after the dissolution of disordered or less-crystalline regions. Although, the dialysis procedure opens up the internal structure, the particle morphology is similar to that observed in the PS.



**Figure 5.5:** Representative cryo-TEM images of room temperature aged TPA-silica sols for (a) 390d-PS and (b) 390d-DS. SAXS patterns are shown in the insets. Corresponding high-resolution cryo-TEM images are shown in (c) and (d), respectively. Frost particles are marked by arrows in (b).

In order to test whether the hypothesis of aggregation of evolving nanoparticles in zeolite growth would hold for samples aged at higher temperature, thorough TEM characterization was performed on similar sols aged at 50 °C. Representative TEM images of PS (Figure 5.6(a)) and DS (Figure 5.6(b)) samples collected after 17 days demonstrate that the PS particles are substantially larger than the DS particles (Figures 5.6(a) and 5.6(b) insets, respectively). Furthermore, the modulated contrast in the images

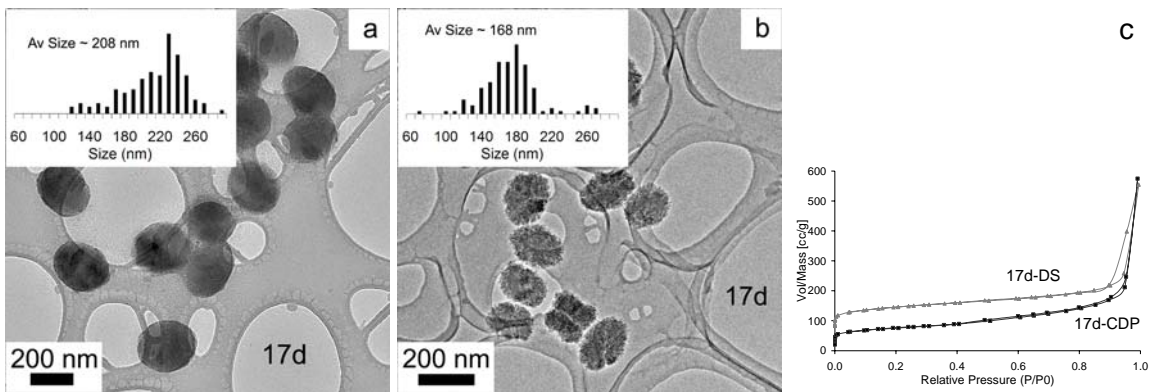


**Figure 5.6: TEM images of TPA-silica sols heated at 50 °C for (a) 17d-PS and (b) 17d-DS. PSDs are shown in the insets. (c) N<sub>2</sub> adsorption-desorption isotherms for the powder obtained from the 17d-CDP and 17d-DS.**

of the DS crystals in Figure 5.6(b) indicates that these particles are porous while the more uniform contrast of the PS crystals indicates these particles are more dense and uniform in their density. Finally, evidence of substantial precipitation, an artifact of TEM sample preparation from undialyzed sols, is also observed. But, the size difference of ~40 nm cannot be fully explained by silica precipitation upon sample drying.

Thus, the samples were further characterized using N<sub>2</sub> adsorption-desorption experiment. The 17d-DS was dried at 60 °C and calcined at 450 °C for 6 h to remove TPA ions from the zeolithic pores. For comparison, the 17d-CDP was calcined in a similar way. The adsorption-desorption isotherms are shown in Figure 5.6(c). Microporosity (indicated by adsorption at low pressure) is significantly higher for the powders obtained from 17d-DS, which indicates the presence of abundant pores that are in the micropore regime ( $\leq 2$  nm). In addition, the BET surface area for 17d-DS ( $446.6\text{ m}^2/\text{g}$ ) is considerably higher than that for the 17d-CDP ( $241.6\text{ m}^2/\text{g}$ ). Higher microporosity as well as particle-size decrease resulting from the dialysis procedure further support conclusion that dissolution of the high solubility, less-crystalline regions occurred during the dialysis procedure.

#### 5.4 Conclusion

Silica sols are followed by a combination of cryo-TEM, conventional (non-cryogenic) TEM and SAXS to elucidate MFI nucleation and crystallization. The formation of amorphous aggregates (noted as  $C_x$  in Figure 1.5) precedes MFI nucleation and crystallization. We report that there exist small MFI fragments in  $C_x$  suggesting that nucleation occurs in these non-crystalline aggregates. There is an intermediate stage of crystal development when crystals are clearly observed in the PS by cryo-TEM but the dialysis procedure has a profound effect on the surface structure suggesting internal disordered regions in growing crystals. The presence of disordered or less-crystalline regions in the growing crystals supports the previously proposed mechanism<sup>17</sup> of MFI growth by the aggregation of structurally distributed population of nanoparticles.

#### ACKNOWLEDGEMENTS

The sample, for microscopy characterization shown in Figure 5.2, was provided by Xueyi Zhang and Pyung-Soo Lee.

---

## MFI GROWTH BY USING MONOMERS AND DIMERS OF TPAOH

This chapter further extends our understanding of MFI nucleation and crystallization by employing structure directing agents (SDAs) other than tetraprolylammonium (TPA). The results discussed here are consistent with MFI growth by aggregation of structurally distributed population of nanoparticles.

### 6.1 Introduction

TPA-silicalite-1 (referred to as MFI) is often studied to elucidate zeolite nucleation and growth in the TPA-silica-water system. The 3-5 nm sized precursor nanoparticles, with disordered silica-core/TPA-shell structure,<sup>29</sup> form immediately upon hydrolysis of silica.<sup>2</sup> The Minnesota group proposed a mechanism of MFI growth that describes the evolution of precursor nanoparticles towards nuclei that trigger the formation of aggregates, which subsequently followed by zeolite nucleation and crystallization.<sup>17,89,99</sup> Evolving nanoparticles continue to attach to the growing crystals.

TPA is the most commonly used structure directing agent (SDA) in MFI synthesis primarily because of its moderately hydrophobic character and its symmetric structure that fits well in the straight channels of MFI.<sup>86,103</sup> TPA-MFI crystals have a hexagonal prismatic morphology with crystal dimensions:  $L_c \geq L_a > L_b$  (where,  $L_i$  is the crystal dimension along the  $i$ -axis; see Figure 2.3(d)). A small change in the structure of the SDA, such as using dimers of TPA, hereafter referred to as dC $n$  with  $n$  equals to the number of carbons in an alkane chain linking the TPA groups, can substantially decrease the rate of MFI growth and dramatically influence the crystal morphology.<sup>58,60,86</sup> Using dC6 results in boat-like morphology with  $L_c > L_a \approx L_b$ , using dC5 results either in flat plate-like ( $L_b$  as the shortest dimension) or cylinder-like ( $L_b > L_c \geq L_a$ ) crystals, dC7 results in octagon-shaped ( $L_c \geq L_a > L_b$ ), and tC6 (a trimer of TPA with the TPA groups linked by a

six carbon chain) leads to flat leaf-shaped crystals with  $L_c > L_b > L_a$ .<sup>60</sup> Interestingly, dC7-MFI crystals also exhibit frequent twinning whereas dC5-, dC6- and tC6-MFI crystals do not.<sup>60</sup>

There have been many studies to understand the role of SDAs in zeolite crystal growth, especially in directing unique morphologies.<sup>28,35,58-60,86,104,105</sup> de Vos Burchart<sup>58</sup> interpreted the relative dimensions of MFI crystals along the a- and b-axes on the basis of how well the SDA molecules fit in the straight vs sinusoidal channels. In case of dC<sub>n</sub>-TPA, molecular mechanics simulation suggested that the SDA molecules prefer straight over sinusoidal channels in the order of dC7<dC6<dC5.<sup>58</sup> However, an increase in the crystal dimension along b-axis is not a universal observation for dC<sub>n</sub>-MFI crystals.<sup>60</sup> Thus, a good fit of SDAs in the framework channels is not a sufficient parameter that can explain the development of unique morphologies. Later, the importance of other parameters, such as SDA adsorption/desorption on the crystal surface, nature of PNs and their rate of attachment and rearrangement, and the effect of silica speciation were proposed to explain the observation of unique crystal morphologies.<sup>59</sup>

Based on atomic force microscopy (AFM) characterization of well-developed TPA-MFI crystals (~20 μm), Agger et al.<sup>85</sup> proposed a 4-fold difference in nucleation of a pentasil layer on the a- and b-surfaces and concluded that crystal dimension along the crystallographic direction is governed by the nucleation rates of pentasil layers rather than the step propagation rates. In a different AFM experiment, Chuan He<sup>106</sup> observed that a- and b- surfaces of TPA- and tC6-MFI crystals have the same surface potential and suggested that the rate of attachment of PNs to the crystal surface should be similar in both cases. Moreover, Diaz et al.<sup>59</sup> performed high-resolution transmission electron microscopy (HRTEM) and AFM on TPA- and tC6-MFI crystals (100-300 nm) and argued that the competition between SDA adsorption/desorption (one-site vs. multiple-site) and surface nucleation rate governs the relative growth rates of crystal surfaces. They proposed that surface nucleation is rate-limiting on the b-surface of tC6-MFI but tC6 adsorption (three-site adsorption) is rate-limiting on the a-surface. The proposed

argument also precluded the addition of PNs as the rate-limiting step for growth on all faces of these well-developed crystals. In an effort to enhance our understanding of the role of SDAs in MFI nucleation and crystallization, we present a study on silica sols synthesized by using a monomer of TPA, dC6 and a mixture of monomer and dC6 by a combination of small-angle x-ray scattering (SAXS) and TEM techniques.

## 6.2 Experimental Methods

### 6.2.1 Synthesis

The SDA-silica sols were prepared as discussed in previous chapters. However, the SDAs used were a monomer of TPA, a dimer (dC6) of TPA, and a mixture of monomer and dC6. The final molar composition was  $20\text{SiO}_2/x\text{TPAOH}/y\text{dC6}/9500\text{H}_2\text{O}$  with  $(x, y) = (9.0, 0.0)$ ,  $(0.0, 4.5)$  and  $(4.5, 2.25)$ , respectively.  $x$  and  $y$  were chosen so that the molar ratio  $\text{N}^+/\text{Si}$  was constant ( $=0.45$ ). Hereafter, prepared sols will be referred to as TPA-, dC6- and TPA/dC6-silica sols, respectively. The sols were stirred for  $\sim 24$  h to complete the hydrolysis of TEOS, filtered ( $0.45 \mu\text{m}$  syringe filter) into multiple Teflon-coated bottles, and then sealed with paraffin film. Immediately after TEOS hydrolysis, the pH of TPA-, dC6- and TPA/dC6-silica sols were 11.15, 11.04 and 11.04, respectively. The bottles were then submerged in oil-baths and aged at  $50^\circ\text{C}$  up to 250 days. Aliquots of the samples were periodically removed and characterized by SAXS and TEM.

The dC6 was synthesized following the recipe described in the literature.<sup>60</sup> The ion exchange of  $\text{I}^-$  to  $\text{OH}^-$  was performed by using  $\text{Ag(II)O}$ .  $\text{Ag(II)O}$  and TPA-dC6( $\text{I}^-$ ) was mixed in water so that both had molar concentrations of 0.1 M. The initial pH of the mixture was 12.05. After 5 days of stirring (pH  $\sim 13$ ), the solution was filtered to remove  $\text{AgI}_2$ . TEM was performed on dC6-MFI crystals synthesized at  $175^\circ\text{C}$  after 2 days aging to test the SDA. Crystals ( $\sim 8 \mu\text{m}$ ) are boat-like with longest dimension parallel to the c-axis as shown in Figure 6.1.

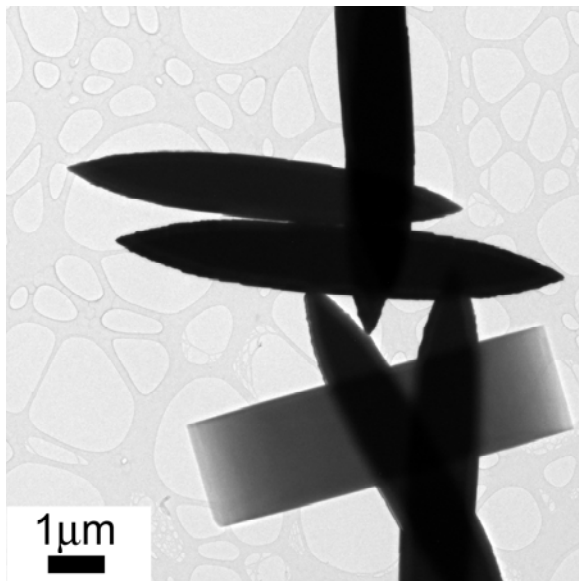


**Figure 6.1:** A representative TEM image of dC6-MFI crystals synthesized at 175 °C aged for 2 days. The crystal have acquired the characteristic boat-like morphology.

### 6.2.2 Small Angle X-ray Scattering (SAXS)

SAXS was used to characterize the PNPs and detect the onset of larger particles in the sol. The SAXSess SAXS (Anton-Parr) instrument was employed in the present study. Sols were loaded into a vacuum-tight 1 mm quartz capillary. The scattering profiles were measured using Cu-K $\alpha$  radiation. After normalizing the SAXS patterns with respect to the incident-beam intensity, the scattering profile from water was subtracted as background. The Generalized Indirect Fourier Transform (GIFT) software<sup>55</sup> was used to analyze the SAXS data and correct for instrumental broadening caused by the line-collimated incident beam.

### 6.2.3 Transmission Electron Microscopy (TEM)

Bright-field, high-resolution and cryogenic TEM were employed in the present work. Here onwards, TEM is used to refer both, bright-field and high-resolution TEM, and cryo-TEM refers specifically to the characterization of vitrified precursor sols. Three

different samples used in this chapter are: precursor sol without any sol alteration (denoted PS), dialyzed sol obtained after two-step dialysis procedure<sup>17</sup> (denoted DS) and powder collected after centrifugation of 250 d aged precursor sol followed by drying at 60 °C (denoted CDP). Two-step dialysis<sup>17</sup> was performed in order to isolate MFI crystals from excess PNs and dissolved silicate species. Centrifugation was done by removing supernatant liquid followed by sol dilution with distilled water; the process was repeated 8-10 times until the pH of the centrifuged sol dropped to ~7.

TEM specimens were prepared by placing a few droplets of DS after dilution with ethanol or a few droplets of PS (no dilution) onto ultrathin holey-carbon coated TEM grids (Ted Pella Inc.) and the grids were allowed to air dry. CDP specimens were prepared by dry mounting, which involved sprinkling the powder onto an ultrathin holey-carbon coated TEM grid. TEM characterization was performed using FEI Tecnai G2 F30 operating at 300 kV equipped with digital camera description.

Cryo-TEM was performed on PS. Specimens were prepared by transferring a small droplet of PS on to a holey-carbon coated TEM grid (Ted Pella Inc.). The droplets were thinned to a film by gently blotting with filter paper. Immediately after thinning, the specimen was plunged into liquid ethane and then quickly moved to a liquid nitrogen reservoir. The vitrified specimens were transferred to a Gatan cooling holder (-180 °C) under liquid nitrogen. A JEOL 1210 operating at 120 kV was used to perform cryo-TEM. All micrographs were collected using a CCD and Gatan Digital Micrograph.

## 6.3 Results and Discussion

### 6.3.1 Precursor Nanoparticles

The SAXS data for sols immediately after TEOS hydrolysis are shown in Figure 6.2(a); an increase in the scattering intensity with dC6 content is discernable. Pair-distance distribution functions (PDDFs) are shown in Figure 6.2(b). The maxima of the

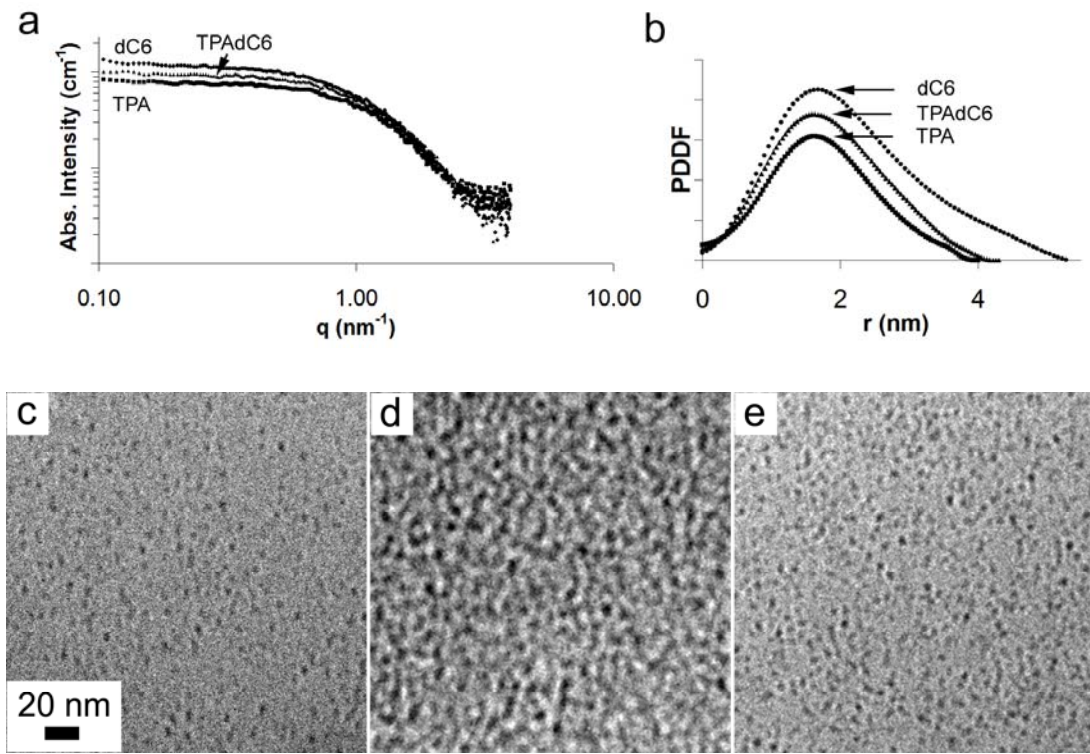


**Figure 6.2:** (a) SAXS patterns and (b) corresponding PDDFs just after TEOS hydrolysis for TPA-, dC6- and TPA/dC6-silica sols. Corresponding cryo-TEM images are shown in (c)–(e), respectively. The scale bar is same for (c)–(e).

PDDFs are at the same position ( $\sim 1.7 \text{ nm}$ ) but the longest dimension has increased from 4 nm for PNs in TPA-silica sol to 5.5 nm for PNs in dC6-silica sol. In the case of monodisperse spheres, the position of the maximum is a close approximation of the radius of the particle.<sup>92</sup> PDDFs in Figure 6.2(b) suggest that PNs in dC6-silica sol have the largest diversion from the monodisperse spherical morphology. However, the possibility of a broader distribution of PN size in dC6- and TPA/dC6-silica cannot be disregarded. The number concentration of PNs was estimated<sup>17,27</sup> using absolute SAXS intensities assuming the PNs were SDA-free and had spherical silica-cores. The result was  $\sim 10^{17}$  particles/cc for all three sols. Representative cryo-TEM images of fresh sols (0d-PS) are shown in Figures 6.2(c)–(e); images are presented at the same magnification.

Despite the differences revealed by the SAXS data, no significant difference in the appearance of PNs was observed by cryo-TEM, which might be due to the limited resolution of the cryo-TEM technique preventing the capture of subtle differences in size and/or shape on the order of 1-2 nm.

The present results differ from previous reports<sup>28,32,86,100</sup> that suggested common PN structures for all mixtures of different SDAs resulting in MFI and that PNs are specific to the zeolite framework formed. The sol composition used in the literature was more concentrated in silica (40<sup>28,32,100</sup> to 95 times<sup>86</sup>) than the sol used in the present study. The larger concentration of nanoparticles in previous studies gave rise to a strong structure factor in the SAXS data and the size of PN was estimated by the position of the maxima in the  $I$  vs.  $q$  plot. In the present study, analyses by PDDFs of a dilute sol capture even a slight difference in the particle size and/or shape, which could be masked by a structure factor and was not detectable by cryo-TEM.

### 6.3.2 Crystallization in TPA-silica sol

SAXS patterns of TPA-silica sol (Figure 6.3(a)) indicate the emergence of larger particles (before 22 d), the size and number of which continued to increase as suggested by an increase and shift in the low- $q$  intensity. The PDDFs for 0, 1 and 9 d aged sols are shown in Figure 6.3(b). The peak position has shifted from 1.64 to 2.34 nm and the longest dimension has increased from 4.0 to 6.5 nm. This PN growth has been reported before and explained by the internal reorganization of nanoparticles and SDA incorporation towards MFI.<sup>17</sup> Crystallization was followed by TEM and representative images are shown in Figures 6.4(a)–(e). The first evidence of crystallinity was observed in the 9 d aged sample; a representative crystal (~40 nm) is shown in Figure 6.4(a). The Fast Fourier Transform (FFT), shown in the inset, indicates the MFI crystallite to be oriented along the b-axis; white dots in the image are straight channels of MFI. Crystallites in this 9d-DS sample were rare (indicating very low-yield), and they have a poorly defined morphology.

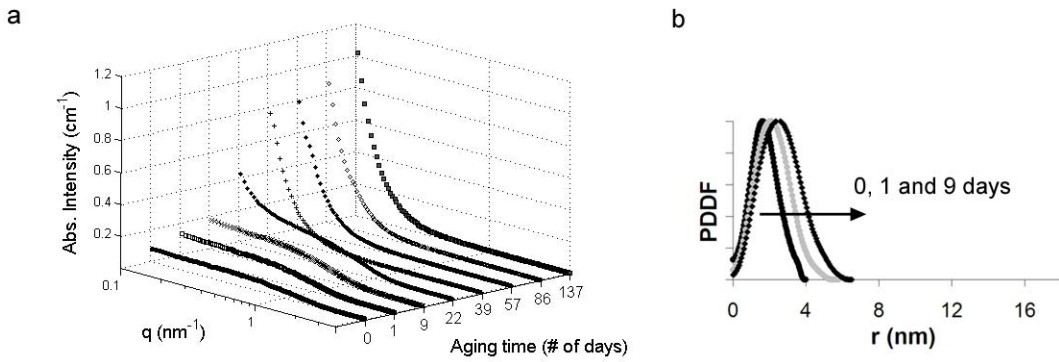


**Figure 6.3: (a)** SAXS patterns for TPA-silica sols until 137 days of aging. PDDFs of 0, 1 and 9 d are shown in (b).

Visible cloudiness, suggesting the presence of numerous larger particles, was observed after 17 d. A representative TEM image of 17d-DS is shown in Figure 6.4(b). A crystal (marked by an arrowhead) is magnified in the inset to reveal the surface roughness. A representative image of TPA-MFI crystals of 22d-DS is shown in Figure 6.4(a). Crystals still have rough appearing surfaces, but the average size has increased to ~200 nm. SAXS data (Figure 6.3)) indicates the presence of plenty of PNPs in solution even after 22 d, the concentration of which drastically decreased after 39 d. TPA-MFI crystals have smoothened surfaces by 86 d (Figure 6.3(d), ~300 nm) and have acquired the equilibrium hexagonal prismatic morphology by 200 d (Figure 6.4(e), ~400 nm). Smooth crystals in 86d-DS indicate that the regions of high-solubility, which led to the opening up of the crystal surfaces until 22d-DS, are no longer available; so there is no usual effect of dialysis on crystals. The faceted morphology of TPA-MFI crystals has been developed after the concentration of PNPs is vanishingly small. It is important to note that the crystal morphology is not defined during the earlier stages of crystallization (here, before 86 d), and they acquire the characteristic morphology only at the later stage

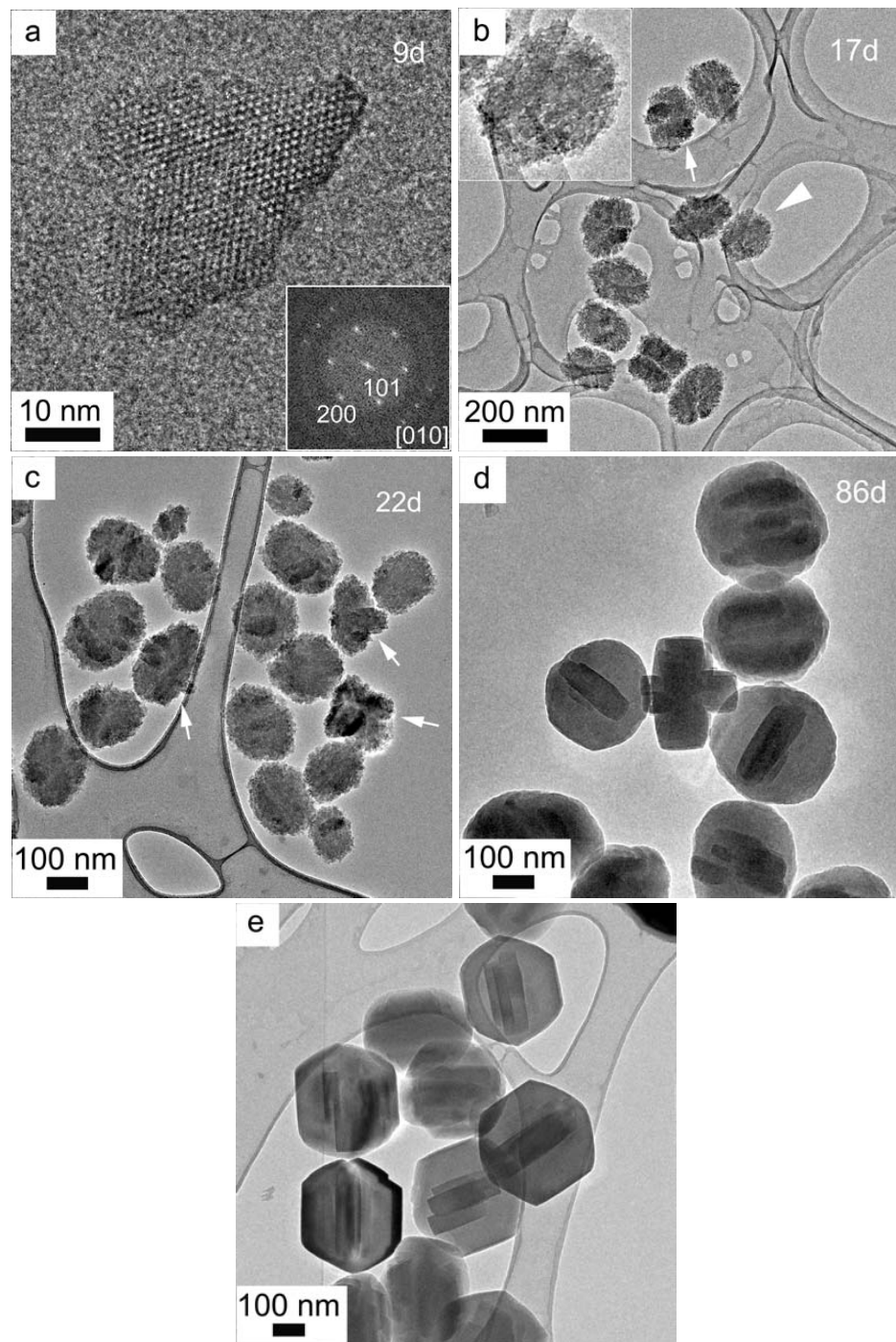


**Figure 6.4: TEM images of TPA-silica sols for (a) 9d-DS, (b) 17d-DS, (c) 22d-DS, (d) 86d-DS and (e) 200d-DS. The marked crystal (by arrowhead) in (b) is magnified in the inset to reveal the surface roughness. Some intergrown crystals are shown by white arrows in (b) and (c).**

of growth ( $\sim 200$  d). Furthermore, no twins were observed in the 9 d aged sol, but they were frequently observed during later stages. Some signs of twins in 17 and 22 d aged sols are shown by arrows in Figures 6.4(b) and (c). This indicates that twins are formed once MFI crystals acquire a finite minimum size. However, the absence of twins in the 9d-DS might also be an artifact of either low-yield of crystals or of the dialysis procedure.

### 6.3.3 Crystallization in dC6-silica sol

The SAXS patterns for dC6-silica sols (Figure 6.5) are distinct from TPA-silica sols as there is no indication of two discrete populations of particles. Overall scattering intensity continues to increase till 57 d, after which there is a rise in the low- $q$  intensity with a subsequent decrease in the high- $q$  intensity. The PDDFs for 0, 1 and 9 d are shown in Figure 6.5(b). The longest dimension has increased from 6 to 16 nm while the position of the peak maximum shifts from 1.7 to 2.7 nm. A cryo-TEM image of 9d-PS is shown in Figure 6.5(c); only PNPs, consistent with the longest dimension from the SAXS data, were observed. PNPs appear elongated and/or aggregated in comparison to the cryo-TEM image of the fresh dC6-silica sol (Figure 6.2(d)). The first evidence of crystallinity in dC6-silica sol was observed after 22 d; a  $\sim 10$  nm sized crystallite is shown in Figure 6.6(a). The FFT inset shows spots with  $d_{hkl} \sim 1.1$  nm, which is consistent with the MFI framework. If compared to TPA-silica sol, which was visibly cloudy by this time, nucleation is substantially delayed in dC6-silica sol. Cloudiness was observed after 63 d in the dC6-silica sol. A representative TEM image of 86d-DS is shown in Figure 6.6(c); crystals have grown to  $\sim 60$  nm. Interestingly, dC6-MFI crystals are smaller in size (63 d,  $< 50$  nm) than TPA-MFI crystals (17 d,  $> 200$  nm) at the stage when cloudiness appears suggesting a high number concentration of dC6-MFI crystals. Therefore, although nucleation was delayed in dC6-silica, the number concentration of dC6-MFI crystals was significantly higher. A cryo-TEM image of 86d-PS is shown in Figure 6.6(d) for a comparison with 86d-DS (Figure 6.6(c)). As discussed for TPA-MFI in chapters 4-5, dC6-MFI crystals do

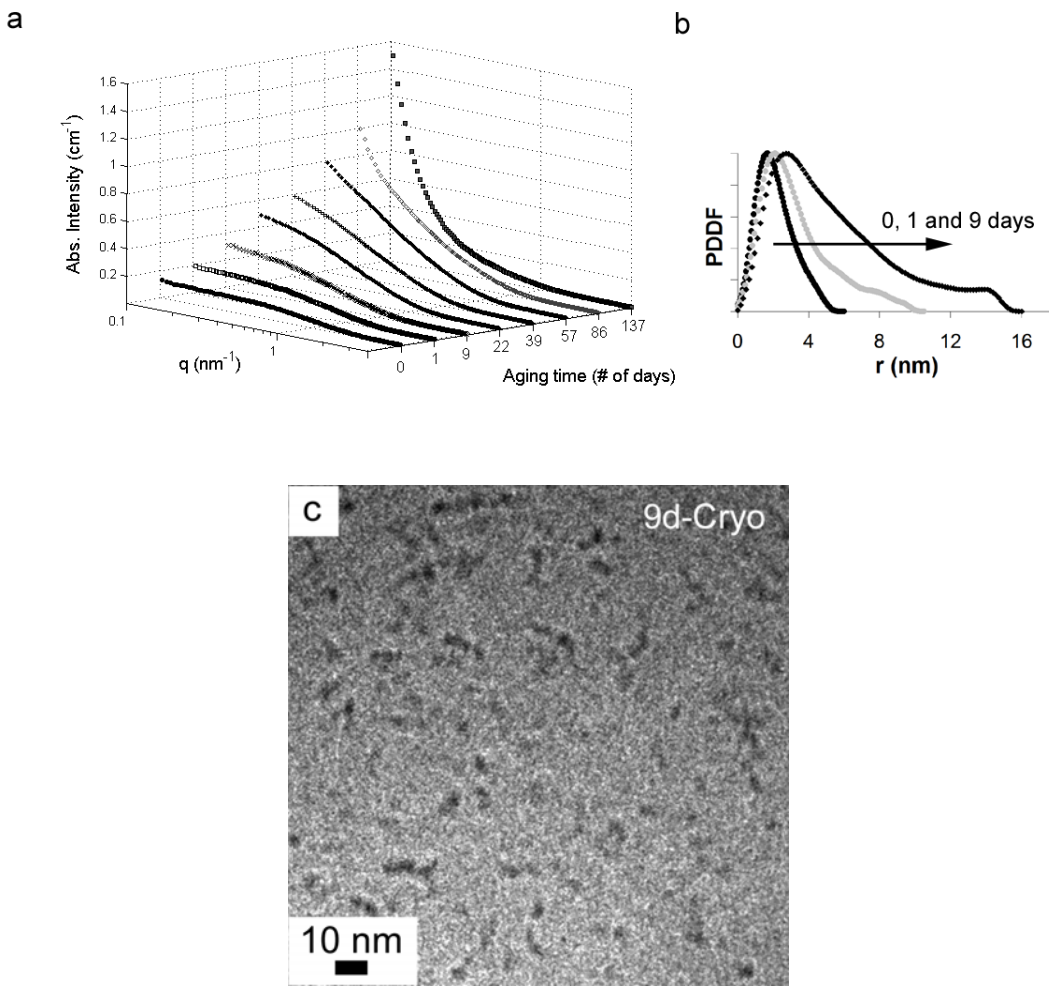


**Figure 6.5:** (a) SAXS follow up for dC6-silica sol. PDDFs for 0, 1 and 9 days heated sols are shown in (b). A cryo-TEM image of dC6-silica for 9d-PS is shown in (c).

not have a defined shape yet but they are more compact in the cryo-TEM image. A slow evolution of PNPs can explain the delayed nucleation in dC6-silica, i.e., a fresh nanoparticle takes longer to evolve to the stage that its colloidal stability is reduced for aggregation followed by crystal growth to occur. The observation of slow crystallization of dC6-MFI agrees with the previous reports that the crystal growth rate decreases as the size of SDA increases from a monomer to a dimer of TPA.<sup>28,86</sup>

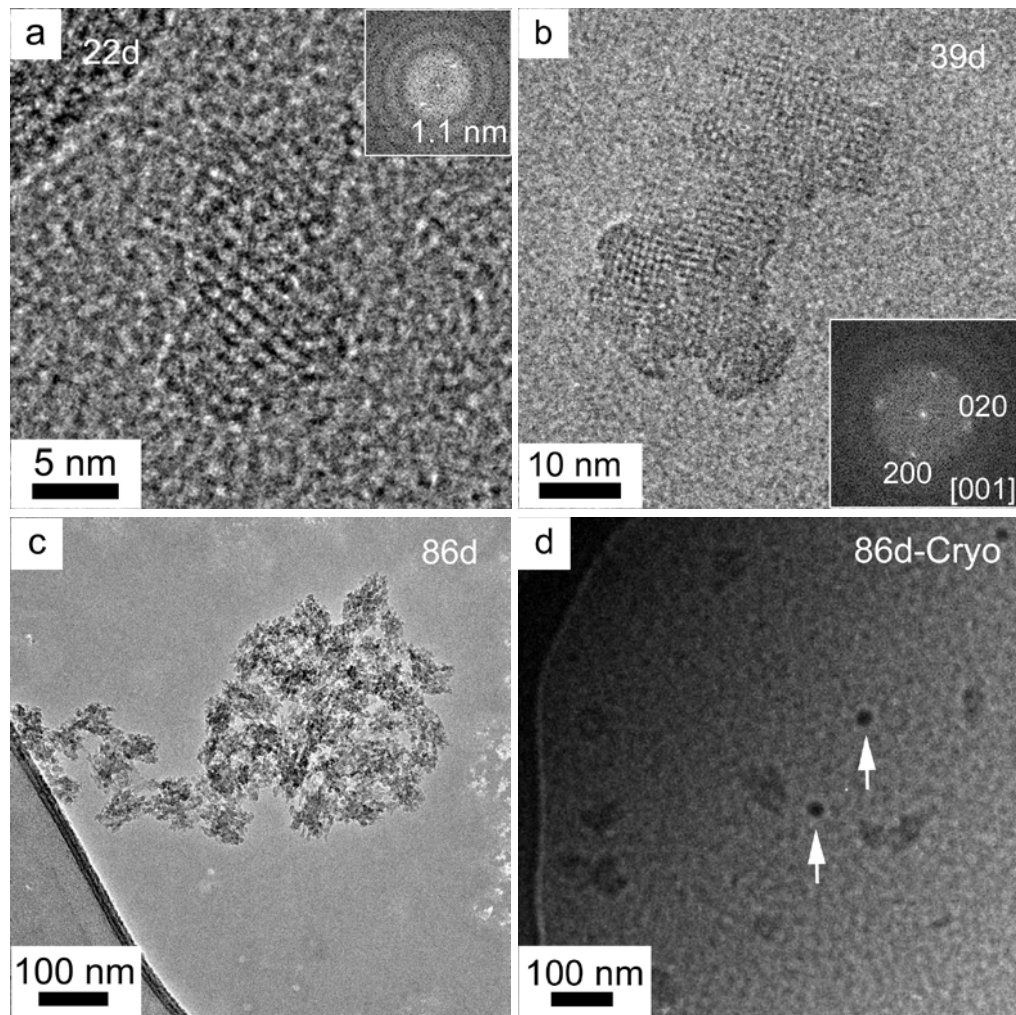


**Figure 6.6:** TEM images of (a) 22d-DS, (b) 39d-DS, and (c) 86d-DS. A cryo-TEM image of 86d-PS is shown in (d); frost particles are shown by arrows.

TEM performed on 250d-CDP is shown in Figure 6.7(a); crystals have grown to oval-shapes with sizes  $\sim$ 150 nm. The present observations indicate that MFI nucleation and growth are slower in dC6-silica than in TPA-silica sol, but growth is even more delayed than nucleation resulting into substantially smaller size of final dC6-MFI crystals. Even after 250 days, the crystals still have open surfaces, and they are far from compact. An HRTEM image of a crystallite oriented along the b-axis with the longest dimension along

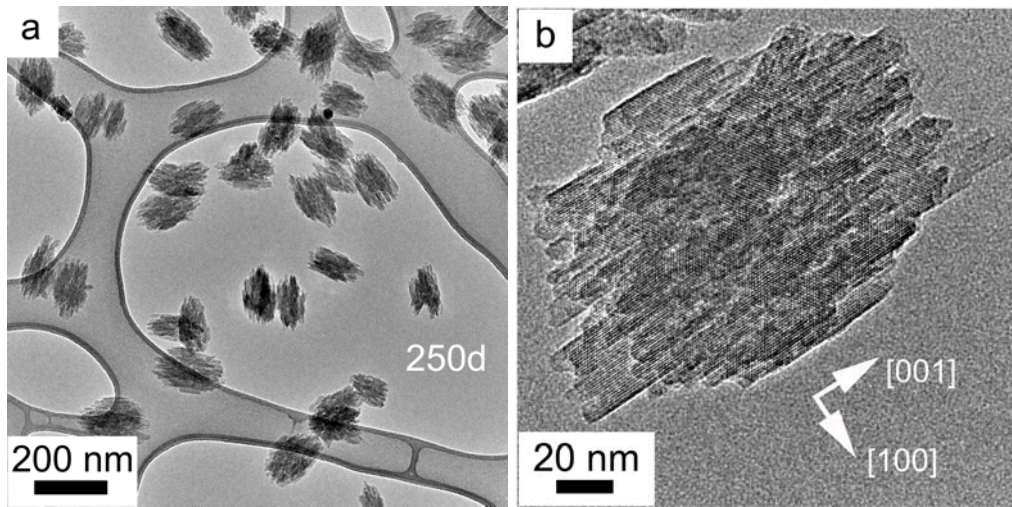


**Figure 6.7:** (a)TEM images of 250d-CDP. A HRTEM image is shown in(b).

the c-axis is shown in Figure 6.7(b). Crystals in Figure 6.7(b) appeared to have a layered structure that can be easily mistaken as a MFI crystal grown layer-by-layer, or a stacked layers of nanoslabs.<sup>88</sup> However, the present results indicate that the final morphology emerges at later stages when PNs have been substantially depleted, and no evidence for such aggregation mechanism of preexisting units exists. Therefore, observing the final crystals alone cannot provide definite information regarding the growth events that lead to their morphology. Instead, crystals must be followed throughout, starting from the early stages of crystal growth.

#### 6.3.4 Crystallization in TPA/dC6-silica sol

SAXS data for TPA/dC6-silica sol, as a function of time, is shown in Figure 6.8(a). In contrast to dC6-silica, there is a separation of the size of the larger particles from PNs after 57 d aging, although not as clear as for TPA-silica sol. PDDFs for 0, 1 and 9 d are shown in Figure 6.8(b). The longest dimension has increased from 4 to 10 nm in 9 days

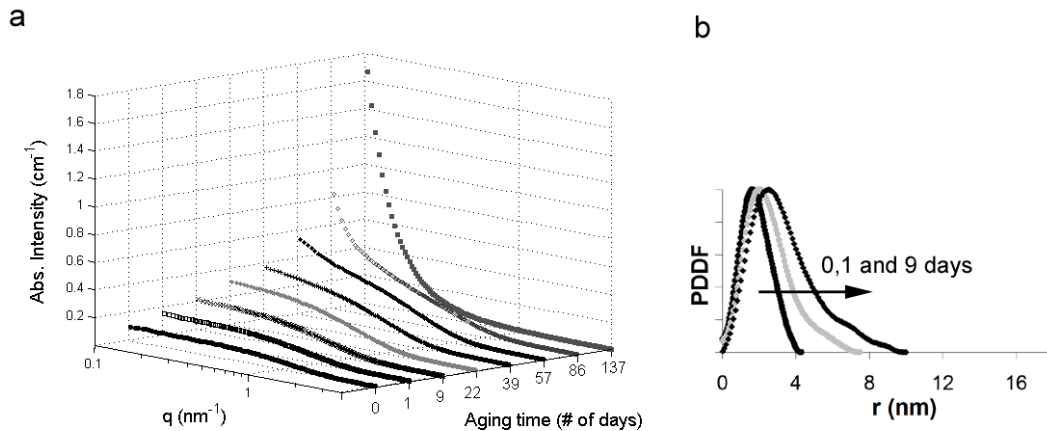


**Figure 6.8: (a)** SAXS follow up for TPA/dC6-silica sol. PDDFs for 0, 1 and 9 d are shown in (b).

and the position of the maximum has shifted from 1.7 to 2.5 nm. TEM images of 39d-DS, 86d-DS, 200d-DS and 250d-CDP are shown in Figures 6.9(a), (c), (e), and (f), respectively. For a comparison with crystals in DS, cryo-TEM images of 39d-PS and 86d-PS are shown in Figures 6.9(b) and 6.9(d), respectively; dot-like contrast is owing to the presence of PNs. Crystals do not have a defined morphology during the earlier stages (before 86 d), but later they appear to be oval-shaped with longest dimension parallel to the c-axis (Figures 6.9(e) and 6.9(f)). The crystal growth process in TPA/dC6-silica sol, as followed by TEM and cryo-TEM, is similar to dC6-MFI and notably different than TPA- MFI. The present work concludes that crystal growth process of TPA/dC6-MFI is dominated by the dC6 content in the composition rather than TPA content in the sol.

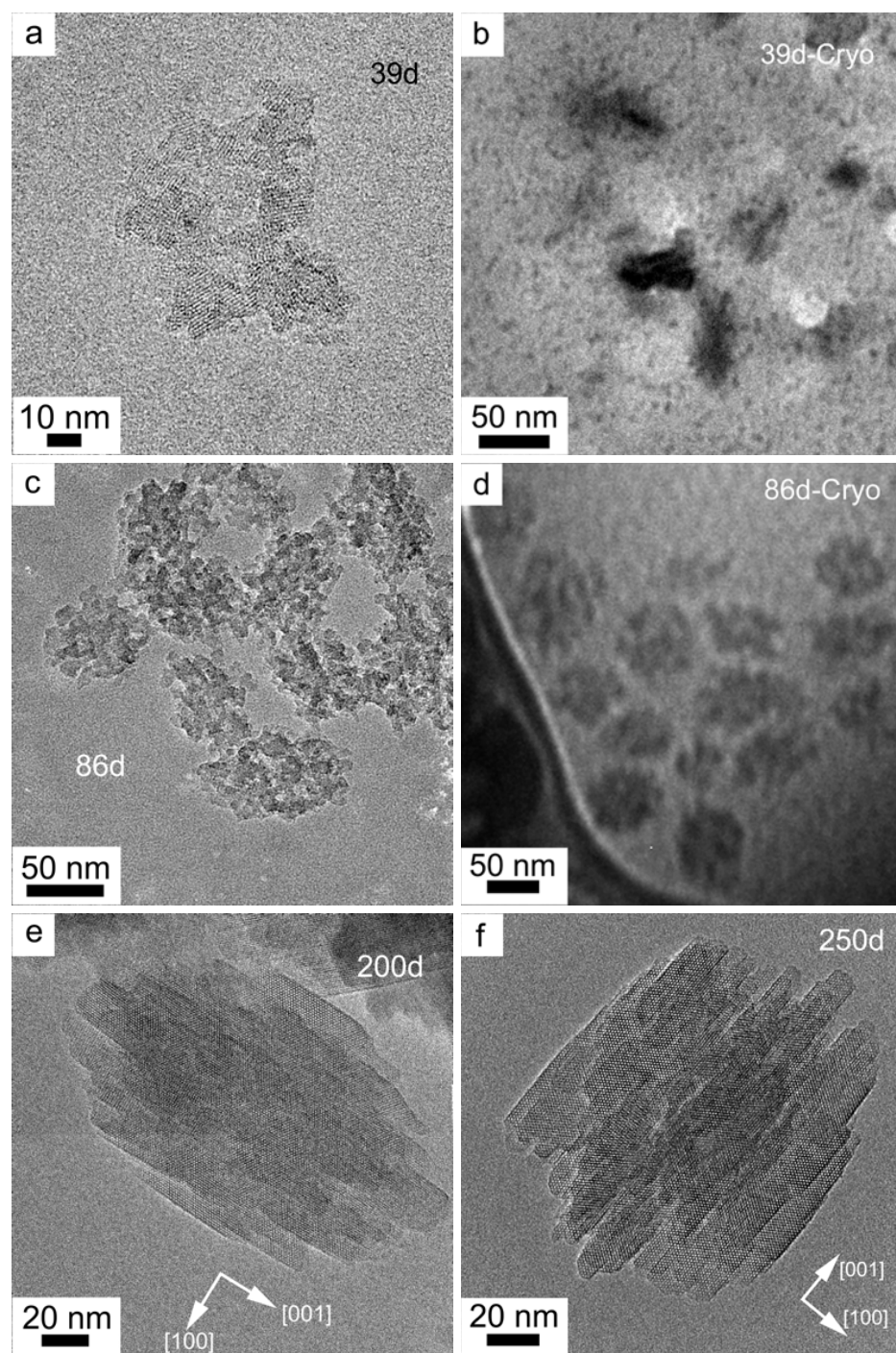


**Figure 6.9:** TEM images of TP/dC6-silica sols for (a) 39d-DS, (c) 86d-DS, (e) 200d-DS and (f) 250d-CDP, and cryo-TEM image of (b) 39d-PS and (d) 86d-PS.

#### 6.4 Conclusions

MFI growth was followed for silica sols prepared using monomer of TPA, dC6, and a mixture of monomer and dC6 by SAXS and TEM (bright-field, high-resolution and cryogenic) techniques. SAXS results demonstrated that the fresh PNs are different in dC6- and TPA/dC6-silica sols as compared to those present in TPA-silica sols. Moreover, SAXS and cryo-TEM show that they evolve during aging, becoming more elongated and/or aggregated. Nucleation and growth in dC6- and TPA/dC6- silica sols were delayed with a more pronounced delay in growth resulting in smaller and a higher number of crystals. Early-stage crystals (coexisting with PN) do not have well-defined morphology and contain less-crystalline (high-solubility) regions as suggested by partial dissolution of these regions during the two-step dialysis procedure. On the contrary, crystals with more developed morphologies appear at later stages when PNs have been mostly depleted. These well-developed crystals do not appear to be affected by dialysis suggesting little to no amorphous/less-crystalline material is present. It is also shown that aggregate-like appearance of final crystals does not necessarily mean that crystals are formed by direct aggregation of pre-existing units. Other, more complicated, solution mediated mechanisms may also be responsible for such appearances.

---

## CONCLUDING REMARKS

This dissertation presents some vital insights into the mechanism of MFI nucleation and growth from solution. Besides supporting the main aspects of the previously proposed model,<sup>17</sup> i.e., structural evolution of nanoparticles and aggregative MFI growth, this research adds new elements. A schematic of the proposed model with new elements is shown in Figure 7.1. The microscopy evidence of crystal-crystal aggregation and the limited role of nanoparticles during crystal faceting are also considered.

The formation of amorphous aggregates is an essential step in MFI nucleation and growth. This research demonstrates that nanoparticles do not require MFI crystalline structure to aggregate. In this regard, the nuclei and aggregates depicted as  $C_1$  and  $C_x$  ( $x < n$ ) in Figure 1.5 may or may not be crystalline. Experimental observations in the present work indicate that Leuven group's hypothesis of precursor nanoparticles as uniquely defined nanoslabs with crystalline MFI structure is not entirely true.<sup>39</sup> Although there are some reports in the literature regarding the importance of internal rearrangement of amorphous aggregates in zeolitic nucleation, present findings give new insights.<sup>37,100,102</sup> Experiments suggest a gradual crystallization of amorphous aggregates rather than a sudden change. However, the available microscopy techniques limit us to directly visualize the nucleation sites in the amorphous aggregates, and so two possibilities, nucleation inside the aggregates or at the liquid-solid interface, are depicted in Figure 7.1. Early stage crystals are characterized by poorly defined morphology and are composed of less-crystalline regions. Zeolite crystals become more compact with aging time. Smoothening/faceting of crystals occurs when the nanoparticle concentration in solution is depleted, and suggested to be governed by monomer addition to the growing crystals.

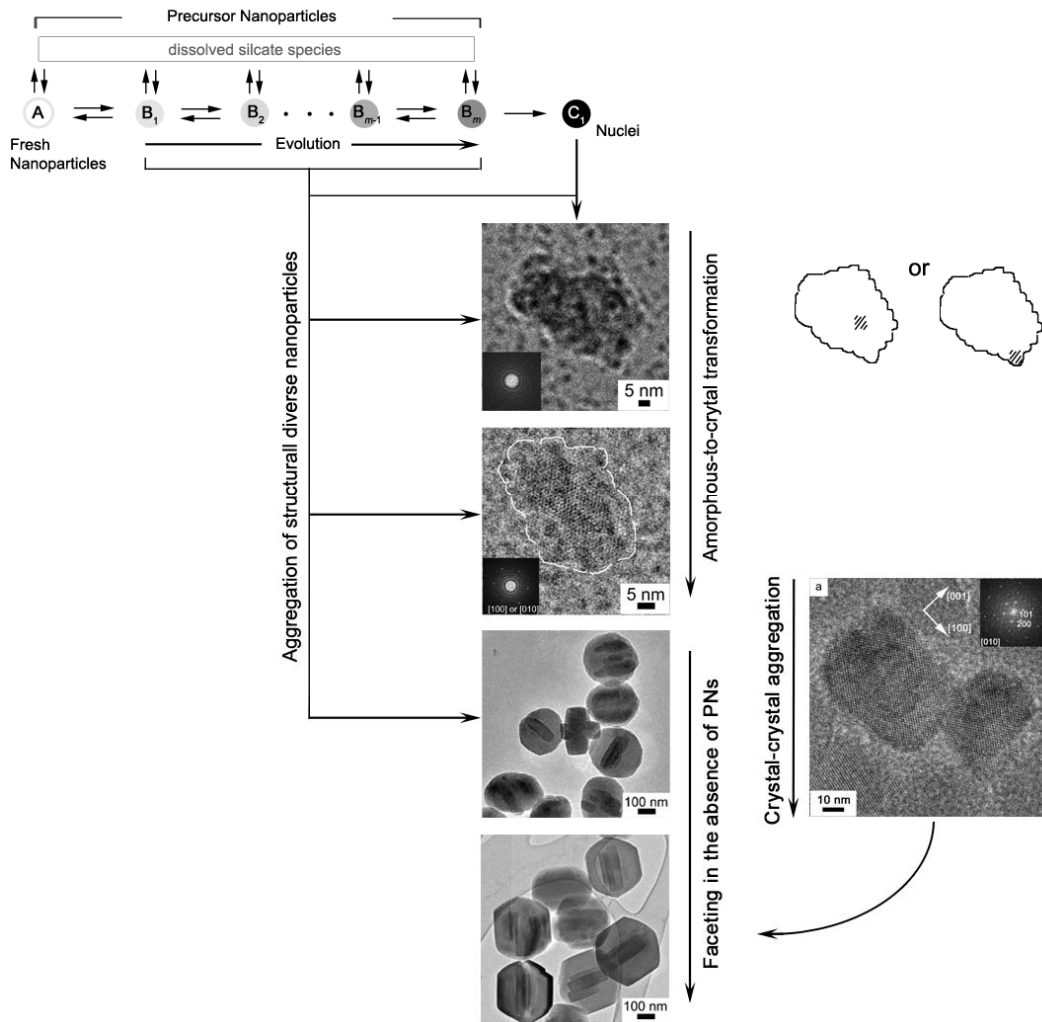


**Figure 7.1:** A schematic illustration of MFI growth mechanism with added new elements: i). formation of amorphous aggregates and intra-aggregate rearrangement to trigger MFI nucleation, ii) crystal faceting in the absence of nanoparticles, and iii) crystal-crystal aggregation.

Formation of finite sized aggregates appears to be very important in MFI nucleation. Thus, in order to harvest 5-10 nm sized faceted MFI crystals, and to use them as building blocks such as to make hierarchical mesoporous material with microporous walls, it is

important to limit aggregation. This goal has been progressively achieved by the group at Minnesota by growing zeolites in confined spaces.<sup>77,107,108</sup>

The use of cryogenic transmission electron microscopy (cryo-TEM) to investigate crystallization events in solution has been limited, primarily, owing to the need of structural resolution imaging. This dissertation demonstrates that it is possible to image electron-beam sensitive materials such as zeolites in the parent sols by cryo-TEM with structural resolution. This opens up a novel path for similar studies for other zeolites and other templated porous materials. A very interesting study on iron-oxides using high-resolution cryo-TEM revealed mesocrystals as an intermediate of crystal grown by oriented aggregation mechanism.<sup>109</sup> This work also opens up the possibility of performing analytical electron microscopy such as energy dispersive spectroscopy (EDS) and electron energy-loss spectroscopy (EELS) to get chemical information from a solution sample. Although it would be challenging, it seems to be feasible depending on the complexity of the system.

## Bibliography

- (1) Breck, D. W. *Zeolite Molecular Sieves*; Wiley, New York, 1974.
- (2) Schoeman, B. J.; Regev, O. *Zeolites* **1996**, *17*, 447.
- (3) Lew, C. M.; Cai, R.; Yan, Y. *Accounts of Chemical Research* **2010**, *43*, 210.
- (4) Giannakopoulos, I. G.; Kouzoudis, D.; Grimes, C. A.; Nikolakis, V. *Adv. Funct. Mater.* **2005**, *15*, 1165.
- (5) Galownia, J.; Martin, J.; Davis, M. E. *Micropor. Mesopor. Mater.* **2006**, *92*, 61.
- (6) Anastas, P. T.; Kirchhoff, M. M.; Williamson, T. C. *Appl. Catal. A: Gen.* **2001**, *221*, 3.
- (7) Davis, M. E. *Nature* **2002**, *417*, 813.
- (8) Li, H.; Eddaoudi, M.; O' Keeffe, M.; Yaghi, O. M. *Nature* **1999**, *402*, 276.
- (9) Ranjan, R.; Tsapatsis, M. *Chem. Mater.* **2009**, *21*, 4920.
- (10) Barton, T. J.; Bull, L. M.; Klemperer, W. G.; Loy, D. A.; McEnaney, B.; Misono, M.; Monson, P. A.; Pez, G.; Scherer, G. W.; Vartuli, J. C.; Yaghi, M. *Chem. Mater.* **1999**, *11*, 2633.
- (11) Kuznicki, S. M., 1990.
- (12) *Database of the Structure Commission of the International Zeolite Association* (<http://www.iza-structure.org/databases/>), 2006.
- (13) Flanigan, E. M.; Bennett, J. M.; Grose, R. W.; Cohen, J. P.; Patton, R. L.; Kirchner, R. M.; Smith, J. V. *Nature* **1978**, *271*, 512.
- (14) Snyder, M.; Tsapatsis, M. *Angew. Chem. Int. Ed.* **2007**, *46*, 7560.
- (15) Lai, Z.; Tsapatsis, M.; Nicolich, J. P. *Adv. Funct. Mater.* **2004**, *14*, 716.
- (16) Coronas, J. *Chemical Engineering Journal* **2010**, *156*, 236.
- (17) Davis, T. M.; Drews, T. O.; Ramanan, H.; He, C.; Dong, J.; Schnablegger, H.; Katsoulakis, M. A.; Kokkoli, E.; McCormick, A. V.; Penn, R. L.; Tsapatsis, M. *Nat. Mater.* **2006**, *5*, 400.
- (18) Mintova, S.; Olson, N. H.; Senker, J.; Bein, T. *Angew. Chem. Int. Ed.* **2002**, *41*, 2558.
- (19) Nikolakis, V.; Kokkoli, E.; Tirrell, M.; Tsapatsis, M.; Vlachos, D. G. *Chem. Mater.* **2000**, *12*, 845.
- (20) Schoeman, B. J. *Microporous and Mesoporous Mater.* **1998**, *22*, 9.
- (21) Tsapatsis, M. *AIChE Journal* **2002**, *48*, 654.
- (22) Wang, J.; Vinu, A.; Coppens, M. O. *J. Mater. Chem.* **2007**, *17*, 4265.
- (23) Schuth, F. *Curr. Opin. Solid State Mat. Sci.* **2001**, *5*, 389.
- (24) Rimer, J. D.; Trofymuk, O.; Lobo, R. F.; Navrotsky, A.; Vlachos, D. G. *J. Phys. Chem. C* **2008**, *112*, 14754.
- (25) Rimer, J. D.; Trofymuk, O.; Navrotsky, A.; Lobo, R. F.; Vlachos, D. G. *Chem. Mater.* **2007**, *19*, 4189.
- (26) Rimer, J. D.; Lobo, R. F.; Vlachos, D. G. *Langmuir* **2005**, *21*, 8960.

- (27) Rimer, J. D.; Vlachos, D. G.; Lobo, R. F. *J. Phys. Chem. B* **2005**, *109*, 12762.
- (28) De Moor, P. E. A.; Beelen, T. P. M.; Santen, R. A. V.; Beck, L. W.; Davis, M. E. *J. Phys. Chem. B* **2000**, *104*, 7600.
- (29) Fedeyko, J. M.; Rimer, J. D.; Lobo, R. F.; Vlachos, D. G. *J. Phys. Chem. B* **2004**, *108*, 12271.
- (30) Houssin, C. J. Y.; Kirschhock, C. E. A.; Magusin, C. M. M.; Mojet, B. L.; Grobet, P. J.; Jacobs, P. A.; Martens, J. A.; Santen, R. A. V. *Phys. Chem. Chem. Phys.* **2003**, *5*, 3518.
- (31) Yang, S.; Navrotsky, A. *Chem. Mater.* **2004**, *16*, 210.
- (32) De Moor, P. E. A.; Beelen, T. P. M.; Santen, R. A. V.; Tsuji, K.; Davis, M. E. *Chem. Mater.* **1999**, *11*, 36.
- (33) Schoeman, B. J. *Zeolites* **1997**, *18*, 97.
- (34) Kirschhock, C. E. A.; Ravishankar, R.; Verspeurt, F.; Grobert, P. J.; Jacobs, P. A.; Martens, J. A. *J. Phys. Chem. B* **1999**, *103*, 4965.
- (35) Burkett, S. L.; Davis, M. E. *J. Phys. Chem.* **1994**, *98*, 4647.
- (36) Mintova, S.; Olson, D. H.; Bein, T. *Angew. Chem. Int. Ed.* **1999**, *38*, 3201.
- (37) Mintova, S.; Olson, D. H.; Valtchev, V.; Bein, T. *Science* **1999**, *283*, 958.
- (38) Kirschhock, C. E. A.; Kremer, S. P. B.; Vermant, J.; Tendeloo, G. V.; Jacobs, P. A.; Martens, J. A. *Chem. Eur. J.* **2005**, *11*, 4306.
- (39) Kirschhock, C. E. A.; Ravishankar, R.; Jacobs, P. A.; Martens, J. A. *J. Phys. Chem. B* **1999**, *103*, 11021.
- (40) Kirschhock, C. E. A.; Buschmann, V.; Kremer, S.; Ravishankar, R.; Houssin, C. J. Y.; Mojet, B. L.; van Santen, R. A.; Grobert, P. J.; Jacobs, P. A.; Martens, J. A. *Angew. Chem. Int. Ed.* **2001**, *40*, 2637.
- (41) Ravishankar, R.; Kirschhock, C. E. A.; Knops-Gerrits, P.-P.; Feijen, E. J. P.; Grobert, P. J.; Vanoppen, P.; Schryver, F. C. D.; Miehe, G.; Fuess, H.; Schoeman, B. J.; Jacobs, P. A.; Martens, J. A. *J. Phys. Chem. B* **1999**, *103*, 4960.
- (42) Drews, T. O.; Tsapatsis, M. *Micro. Meso. Mater.* **2006**, article in press.
- (43) Kragten, D. D.; Fedeyko, J. M.; Sawant, K. R.; Rimer, J. D.; Vlachos, D. G.; Lobo, R. F. *J. Phys. Chem. B* **2003**, *107*, 10006.
- (44) Choi, J.; Ghosh, S.; Lai, Z.; Tsapatsis, M. *Angew. Chem. Int. Ed.* **2006**, *45*, 1154.
- (45) Penn, R. L.; Banfield, J. F. *Am. Mineral.* **1998**, *83*, 1077.
- (46) Penn, R. L.; Banfield, J. F. *Geochim. Cosmochim. Acta* **1999**, *63*, 1549.
- (47) Banfield, J. F.; Welch, S. A.; Zhang, H.; Ebert, T. T.; Penn, R. L. *Science* **2000**, *289*, 751.
- (48) Liu, Z.; Sakamoto, Y.; Ohsuna, T.; Hiraga, K.; Terasaki, O.; Ko, C. H.; Shin, H. J.; Ryoo, R. *Angew. Chem. Int. Ed.* **2000**, *39*, 3107.
- (49) Lee, E. J. H.; Ribeiro, C.; Longo, E.; Leite, E. R. *J. Phys. Chem. B* **2005**, *109*, 20842.

- (50) Ribeiro, C.; Lee, E. J. H.; Longo, E.; Leite, E. R. *ChemPhysChem* **2005**, *6*, 690.
- (51) Gehrke, N.; Colfen, H.; Pinna, N.; Antonietti, M.; Nassif, N. *Cryst. Growth Des.* **2005**, *5*, 1317.
- (52) Tsapatsis, M.; Lovallo, M.; Davis, M. E. *Microporous Mater.* **1996**, *5*, 381.
- (53) Bursill, L. A.; Thomas, J. M.; Rao, K. J. *Nature* **1981**, *289*, 157.
- (54) Pan, M. *Micron* **1996**, *27*, 219.
- (55) Orthaber, D.; Bergmann, A.; Glatter, O. *J. Appl. Cryst.* **2000**, *33*, 218.
- (56) Talmon, Y. *Colloids and Surfaces* **1986**, *19*, 237.
- (57) Glatter, O.; Kratky, O. *Small Angle X-ray Scattering*; Academic Press Inc. (London) Ltd., 1982.
- (58) Burchart, E. D.; Jansen, J. C.; Graaf, B. V.; Bekkum, H. V. *Zeolites* **1993**, *13*, 216.
- (59) Diaz, I.; Kokkoli, E.; Terasaki, O.; Tsapatsis, M. *Chem. Mater.* **2004**, *16*, 5226.
- (60) Bonilla, G.; Diaz, I.; Tsapatsis, M.; Jeong, H.-K.; Lee, Y.; Vlachos, D. G. *Chem. Mater.* **2004**, *16*, 5697.
- (61) Penn, R. L.; Banfield, J. F. *Science* **1998**, *281*, 969.
- (62) Penn, R. L. *J. Phys. Chem. B* **2004**, *108*, 12707.
- (63) Talmon, Y. *Ber. Bunsenges Phys. Chem.* **1996**, *100*, 364.
- (64) Talmon, Y. *Modern Characterization Methods of Surfactant Systems*; Marcel Dekker Inc. New York, 1999.
- (65) Thomas, J. M.; Terasaki, O.; Gai, P. L.; Zhou, W.; Gonzalez-Calbet, J. *Acc. Chem. Res.* **2001**, *34*, 583.
- (66) Treacy, M. M. J.; Newsam, J. M. *Ultramicroscopy* **1987**, *23*, 411.
- (67) Talmon, Y. *Colloid Surface* **1986**, *19*, 237.
- (68) Bellare, J. R.; Davis, H. T.; Scriven, L. E.; Talmon, Y. *J. Electron Microsc.* **1988**, *10*, 87.
- (69) Talmon, Y. *J. Colloid Interface Sci.* **1983**, *93*, 366.
- (70) Qin, L. C.; Hobbs, L. W. "Quantitative HREM of Electron-Irradiated Quartz"; Materials Research Society Symposium Proceedings, 1995, Boston, MA.
- (71) Cui, H.; Hodgdon, T. K.; Kaler, E. W.; Abezgauz, L.; Danino, D.; Lubovsky, M.; Talmon, Y.; Pochan, D. J. *Soft Matter* **2007**, *3*, 945.
- (72) Carter, C. B.; Williams, D. B. *Transmission Electron Microscopy*; plenum, 1996.
- (73) Falls, A. H.; Wellinghoff, S. T.; Talmon, Y.; Thomas, E. L. *J. Mater. Sci.* **1983**, *18*, 2752.
- (74) Vertsner, V. N.; Zhdanov, G. S. *Sov. Phys. Crystallogr.* **1966**, *10*, 597.
- (75) Dubochet, J.; Lepault, J.; Freeman, R.; Berriman, J. A.; Homo, J. C. *J. Microsc.* **1982**, *128*, 219.
- (76) Hall, D.; Wood, M. K. *Acta Cryst.* **1985**, *B41*, 169.

- (77) Fan, W.; Snyder, M.; Kumar, S.; Lee, P.; Yoo, W. C.; McCormick, A. V.; Penn, R. L.; A. S.; Tsapatsis, M. *Nature Materials* **2008**, *7*, 984.
- (78) Balmes, O.; Malm, J. O.; Pettersson, N.; Karlsson, G.; Bovin, J. O. *Microsc. Microanal.* **2006**, *12*, 1.
- (79) Bonilla, G.; Vlachos, D. G.; Tsapatsis, M. *Micropor. Mesopor. Mater.* **2001**, *42*, 191.
- (80) Valtchev, V.; Bozhilov, N. *J. Am. Chem. Soc.* **2005**, *127*, 16171.
- (81) Li, S.; Li, Z.; Bozhilov, K. N.; Chen, Z.; Yan, Y. *J. Am. Chem. Soc.* **2004**, *126*, 10732.
- (82) Ruthstein, S.; Schmidt, J.; Kesselman, E.; Talmon, Y.; Goldfarb, D. *J. Am. Chem. Soc.* **2006**, *128*, 3366.
- (83) Ruthstein, S.; Schmidt, J.; Kesselman, E.; Popovitz-Biro, R.; Omer, L.; Frydman, V.; Talmon, Y.; Goldfarb, D. *Chem. Mater.* **2008**, *20*, 2779.
- (84) de Moor, P. E. A.; Beelen, T. P. M.; Komanschek, B. U.; Diat, O.; Santen, R. A. V. *J. Phys. Chem. B* **1997**, *101*, 11077.
- (85) Agger, J. R.; Hanif, N.; Cundy, C. S.; Wade, A. P.; Dennison, S.; Rawlison, P. A.; Anderson, M. W. *J. Am. Chem. Soc.* **2003**, *125*, 830.
- (86) Cheng, C.-H.; Shantz, D. F. *J. Phys. Chem. B* **2005**, *109*, 13912.
- (87) Ramanan, H.; Kokkoli, E.; Tsapatsis, M. *Angew. Chem. Int. Ed.* **2004**, *43*, 2.
- (88) Liang, D.; Follens, L. R. A.; Aerts, A.; Martens, J. A.; Van Tendeloo, G. *J. Phys. Chem. C* **2007**, *111*, 14283.
- (89) Kumar, S.; Davis, T. M.; Ramanan, H.; Penn, R. L.; Tsapatsis, M. *J. Phys. Chem. B* **2007**, *111*, 3398.
- (90) Cheng, C.-H.; Shantz, D. F. *Curr. Opin. Colloid Interface Sci.* **2005**, *10*, 188.
- (91) Bergmann, A.; Fritz, G.; Glatter, O. *J. Appl. Cryst.* **2000**, *33*, 1212.
- (92) Glatter, O. *J. Appl. Cryst.* **1979**, *12*, 166.
- (93) Talmon, Y. *Modern characterization methods of surfactant systems*; Marcel Dekker: New York, NY, 1999.
- (94) Epping, J. D.; Chmelka, B. F. *Curr. Opin. Colloid Interface Sci.* **2006**, *11*, 81.
- (95) Pelster, S. A.; Schrader, W.; Schuth, F. *J. Am. Chem. Soc.* **2006**, *128*, 4310.
- (96) Patis, A.; Dracopoulos, V.; Nikolakis, V. *J. Phys. Chem. C* **2007**, *111*, 17478.
- (97) Cheng, Y.; Wang, Y.; Zheng, Y.; Qin, Y. *J. Phys. Chem. B* **2005**, *109*, 11548.
- (98) Iler, R. K. *The Chemistry of Silica*; John Wiley & Sons, 1979.
- (99) Kumar, S.; Wang, Z.; Penn, R. L.; Tsapatsis, M. *J. Am. Chem. Soc.* **2008**, *130*, 17284.
- (100) de Moor, P. E. A.; Beelen, T. P. M.; Komanschek, B. U.; Beck, L. W.; Wagner, P.; Davis, M. E.; van Santen, R. A. *Chem. Eur. J.* **1999**, *5*, 2083.

- (101) Van Santen, R. A. *Nature* **2006**, *444*, 46.
- (102) Beale, A. M.; van der Eerden, A. M. J.; Jacques, S. D. M.; Leynaud, O.; O'Brien, M. G.; Meneau, F.; Nikitenko, S.; Bras, W.; Weckhuysen, B. M. *J. Am. Chem. Soc.* **2006**, *128*, 12386.
- (103) Lobo, R. F.; Zones, S. I.; Davis, M. E. *J. Inclusion Phenom. Mol.* **1995**, *21*, 47.
- (104) Burkett, S. L.; Davis, M. E. *Chem. Mater.* **1995**, *7*, 920.
- (105) Burkett, S. L.; Davis, M. E. *Chem. Mater.* **1995**, *7*, 1453.
- (106) He, C., University of Minnesota, 2005.
- (107) Yoo, W. C.; Kumar, S.; McCormick, A. V.; Penn, R. L.; Tsapatsis, M.; Stein, A. *J. Am. Chem. Soc.* **2009**, *131*, 12377.
- (108) Yoo, W. C.; Kumar, S.; Wang, Z.; Ergang, N. S.; Fan, W.; Karanikolos, G. N.; McCormick, A. V.; Penn, R. L.; Tsapatsis, M.; Stein, A. *Angew. Chem. Int. Ed.* **2008**, *47*, 9096.
- (109) Yuwono, V. M.; Burrows, N. D.; Soltis, J. A.; Penn, R. L. *J. Am. Chem. Soc.* **2010**, *132*, 2163.
- (110) Walker, A. M.; Slater, B.; Gale, J. D.; Wright, K. *Nature Mater.* **2004**, *3*, 715.
- (111) Dumrul, S.; Bazzana, S.; Warzywoda, J.; Biederman, R. R.; Sacco, A. *Microporous and Mesoporous Materials* **2002**, *54*, 79.
- (112) Terasaki, O.; Thomas, J. M.; Ramdas, S. *J. Chem Soc., Chem. Commun.* **1984**, *1537*, 216.
- (113) Campbell, B. J.; Cheetham, A. K. *J. Phys. Chem. B* **2002**, *106*, 57.

## Appendix A: Defects in dC5-MFI

This chapter discusses the presence of planar defects such as interfaces, triple junctions and coincidence boundaries in MFI crystals grown by using dC5 (dimer of tetrapropylammonium (TPA) with 5 carbon atoms linking the head groups).

### A.1 Introduction

Study of the formation and behavior of defects is one of the most understudied areas in zeolite research. Many industrially relevant zeolites display features, which suggest that transport of guest species through these porous solids is, to a greater or lesser extent, hindered.<sup>110-112</sup> These observations imply the presence of defects in zeolites such as linear-chain defects,<sup>113</sup> faults,<sup>112</sup> growth spirals,<sup>111</sup> or dislocations.<sup>110</sup> The occurrence of planar defects perpendicular to the pore-alignments have been postulated to account for the reduced diffusivity of the guest species.<sup>1,112</sup> A better understanding of defects is a step towards defect-free zeolite particle production. This chapter demonstrates the presence of some planar defects in dC5-MFI crystals.

### A.2 Experimental Methods

The synthesis mixture was heated for four days at 175 °C. Crystalline powder was obtained after centrifugation followed by drying at 70 °C. The powder was calcined for 10 hours at 540 °C to remove organic ions from zeolite pores. High-resolution transmission electron microscopy (HRTEM) characterization was performed using a 300 kV FEI Tecnai G2 F-30. Sample preparation was done by crushing the powder in mortar and pestle and sprinkling the powder on lacey-carbon coated ultra-thin TEM grid (Ted Pella Inc.).

### A.3 Results and Discussion

The dC5-MFI has a characteristic flat-sheet morphology with the thin dimension along the b-axis.<sup>60</sup> A representative TEM image is shown in Figure A.1. An electron-diffraction pattern from a clean area of the crystal, marked by an arrow, is shown in the inset. dC5-MFI crystal size ranges from 100s nm to a few microns. Very often, tiny fragments of crystals are observed as attached to the larger crystals. Clean areas of the crystal were carefully chosen for TEM characterization.

Two example TEM images of dC5-MFI with interfaces are shown in Figures A.2(a) and (b). Schematics and the Fast Fourier Transforms (FFTs) of the images are shown in right. Interfaces consist of facets along high-index crystallographic planes such as {100}, {001} and {101}. Region A (see Figure A.2(a) and the schematic in its right) has a coincidence boundary defined by a rotation angle  $\sim 53^\circ$  with the b-axis as the axis of rotation. In a coincidence boundary (here, the boundary is in the plane of the page), both

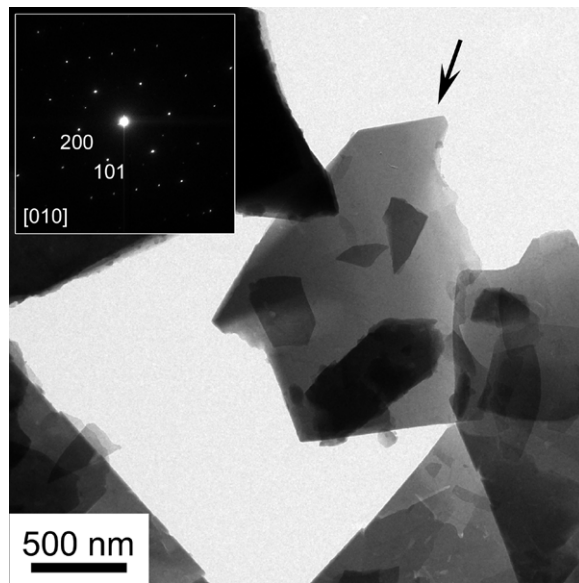


**Figure A.1:** A representative TEM image showing characteristic morphology of dC5-MFI. Electron-diffraction pattern from the clean region of the crystal (marked by an arrow) is shown in the inset.

sides are rotated around a common axis so that they form a common repeated structure. Figure A.2(b) shows an example “triple junction”; three crystals meet coherently at a junction with no mismatch as indicated by the FFT. The occurrence of coherent interfaces

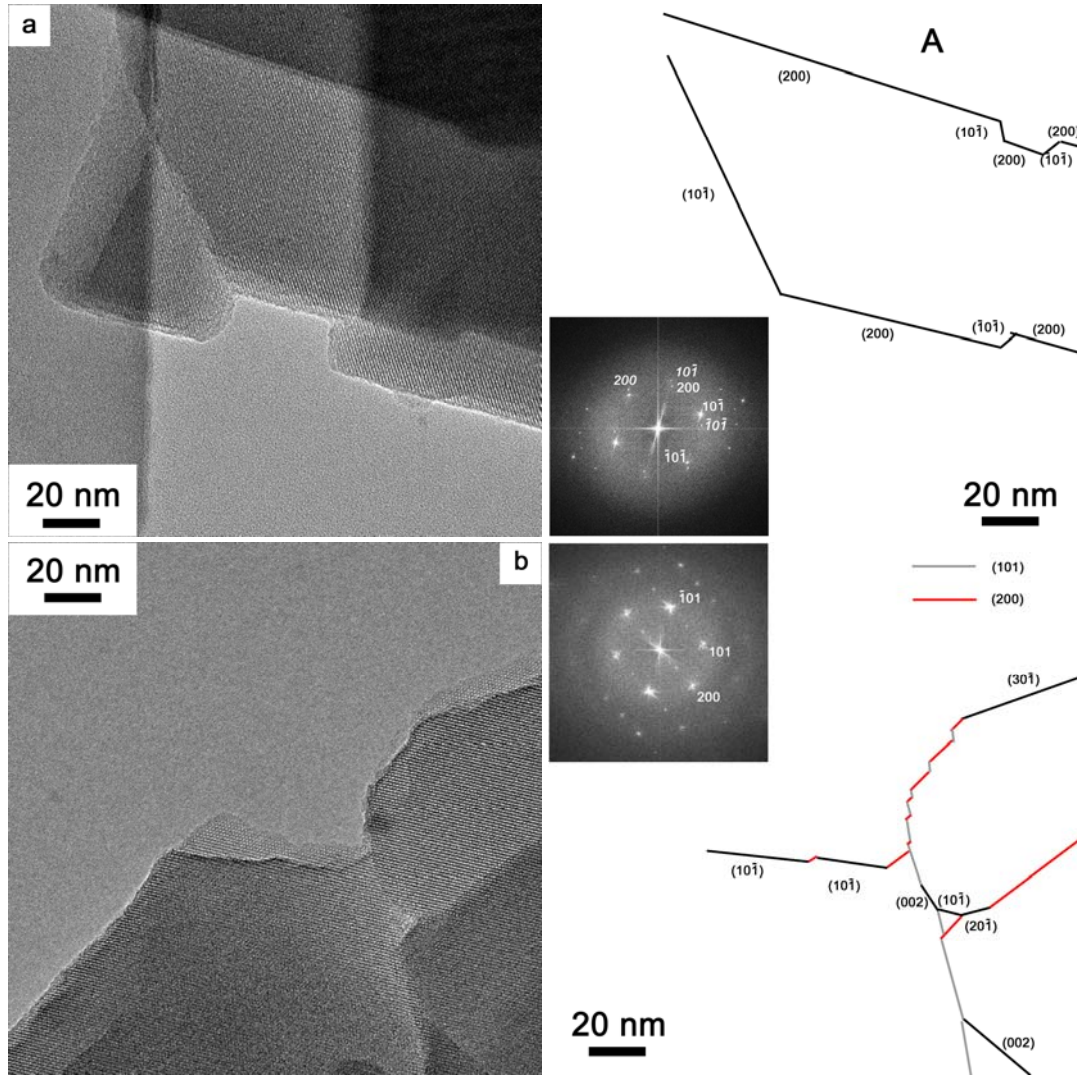


**Figure A.2:** TEM micrographs ((a) and (b)) show coherent interfaces; schematics are shown in right. FFTs are shown as insets with the schematics. The spots, shown in italics in the FFT of (a), have their origin in region ‘A’. ‘A’ consists a coincidence boundary (rotation angle  $\sim 53^\circ$  with the b-axis as the axis of rotation).

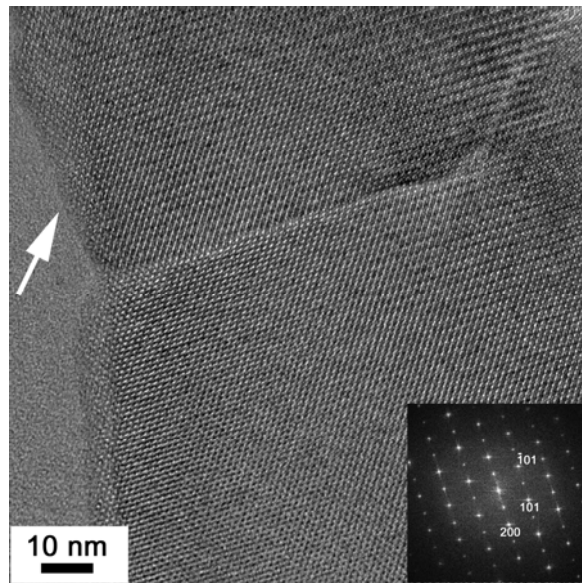


**Figure A.3:** A HRTEM image, with FFT inset, shows an interface with facets along (200) and (101).

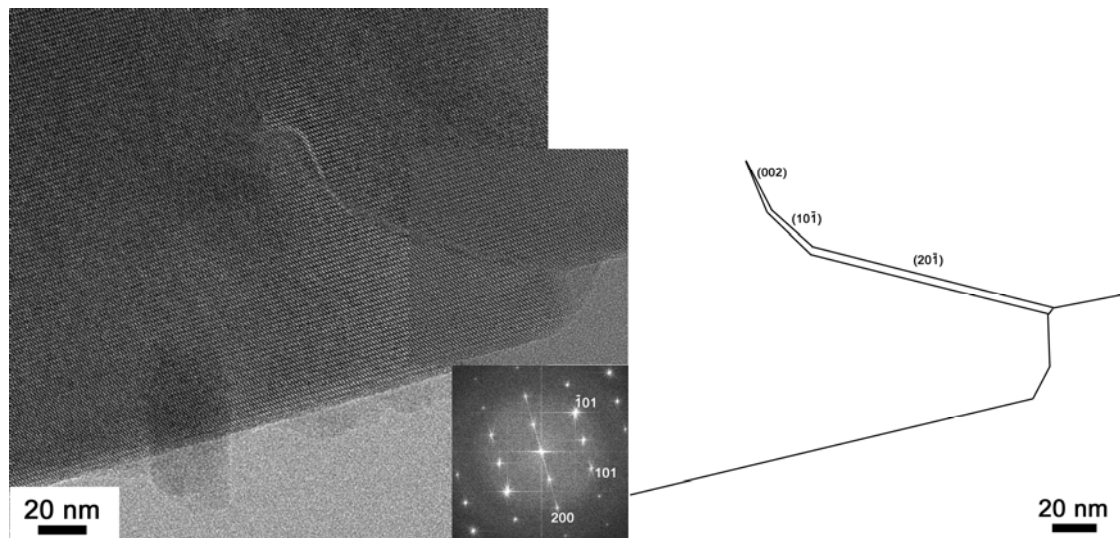


**Figure A.4:** A HRTEM image, with FFT inset, showing an interface. A probable schematic of the facets are shown at right.

in Figures A.2(a) and (b) can be explained by crystal-crystal aggregation. Although, FFT indicates that regions to either side of the defect boundary are in structural accord, there

are atomic level disruptions as suggested by the HRTEM images. Better resolution and image simulation are required to fully characterize these defects. Such deviation from the ideal crystal structure may occur due to the higher activity (unsatisfied chemical bonds) of approaching surfaces.

Another example of a dC5-MFI sheet with coherent interfaces (suggested by the FFT) is shown in Figure A.3. FFT is shown in the inset; the interface can be resolved into (200) and (101) planes. The FFT also contain spots at kinematically forbidden positions, such as (100) and (001). These forbidden reflections have their origins only in the top region of the crystal (indicated by an arrow). One more example with the presence of forbidden reflections is shown in Figure A.4. A representative TEM image shows a rough appearing boundary between the two regions of the single-crystalline sheet, which has vanished when going towards the central region of the crystal. This interface is made up of (002), (101), and (201) facets as depicted in the schematic shown in the right. The kinematically forbidden reflections have origins in both sides of the interface in Figure A.4.

#### A.4 Conclusions

dC5-MFI sheets were studied for the presence of a variety of planar defects using HRTEM.

#### ACKNOWLEDGEMENTS

dC5-MFI sample was provided by Dr Shubhajit Ghosh and Dr Jungkyu Choi.

## Appendix B: Other Work Done at the University of Minnesota

### B.1 Crystallization of Zeolite beta<sup>e</sup>

Nucleation and crystallization of zeolite beta was studied with a combination of total reflectance-Fourier transform spectroscopy, small angle scattering and cryogenic-transmission electron microscopy. The existence of structurally distributed population of precursor nanoparticles (<3 nm) was reported, fraction of which aggregated to form secondary particles. After prolonged heating (here at 6 days at 120 °C), secondary particles aggregate into tertiary particles that have the structure of zeolite beta. The main aspects of the mechanism were concluded to be similar to the results discussed in chapters 2-6.

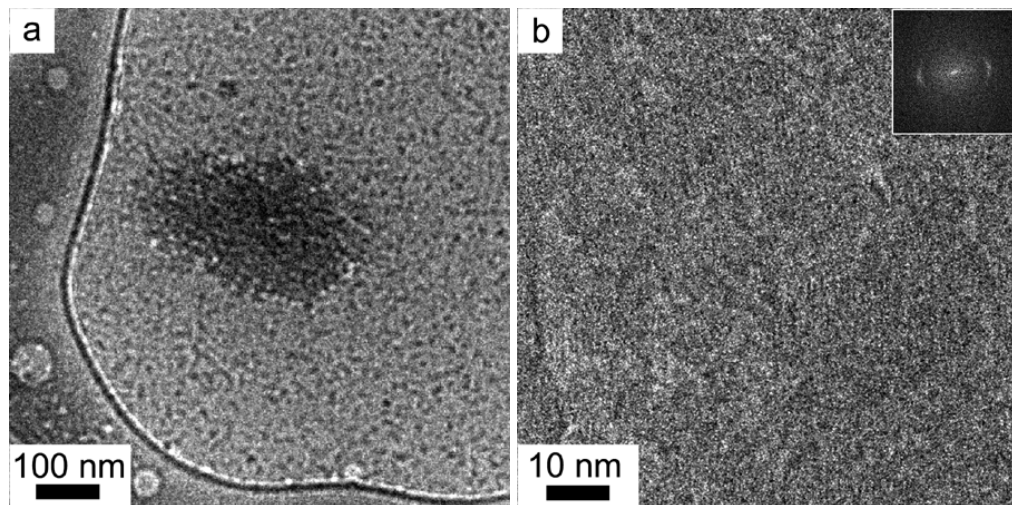


**Figure B.1. (a)** A representative cryo-TEM image showing a tertiary particle in solution after 8 days of heating. **(b)** A High-resolution cryo-TEM image showing crystalline order in the particle. The inset FFT shows spots with d-spacing of about 1.1 nm.

<sup>e</sup>N D Hould, S Kumar, M Tsapatsis, V Nikolakis and R F Lobo, *Langmuir*, **2010**, 26(2), 1260

## B.2 Microscopy Characterization of MCM-22

MCM-22, a type of zeolite, can crystallize in the form of a layered precursor, MCM-22(P), composed of 2.5 nm thick sheet stacked in registry. Upon calcination, the layers condense together to form MCM-22. The major interest stems from the fact that the layers can be swollen, pillared, and exfoliated to give a range of catalytically active materials. The study involved finding an approach to swell MCM-22(P) without disrupting the crystal structure. Reversibility of the swelling process was demonstrated, and the swollen material was successfully pillared to produce an MCM-36 analogue.

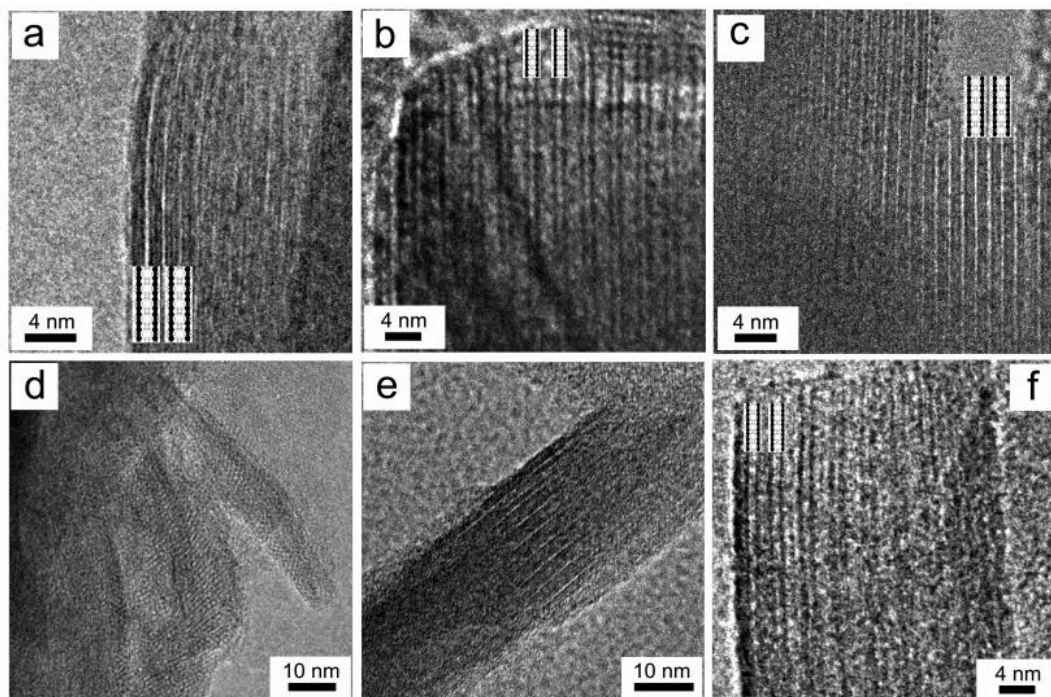


**Figure B.2:** HRTEM images of (a) MCM-22(P), (b) MCM-22(PS-RT), (c) deswollen MCM-22(P) obtained by acidification of MCM-22(PS-RT), and (d-f) MCM-22(PS-80). Room-temperature and 80 °C swollen precursors are noted as PS-RT and PS-80.

<sup>f</sup>S Maheshwari, E Jordan, S Kumar, F S Bates, R L Penn, D F Shantz and M Tsapatsis, *J. Amer. Chem. Soc.*, **2008**, 130 (4), 1507

### B.3 Confined Synthesis of Zeolites<sup>\$, ¥, §</sup>

The three-dimensionally ordered macroporous (3DOM)<sup>\$, ¥</sup> and mesoporous (3DOM)<sup>§</sup> carbon can act as reaction chambers for synthesis of zeolite particles with uniform sizes. It was demonstrated that confined crystal growth within these templates leads to size-tunable, zeolite particles (here, silicalite-1 which has MFI type framework) from sizes, 10-40 nm to more than 300 nm. In addition, novel crystal morphologies and faceted crystal outgrowths also provided new insight into crystal growth mechanisms underlying confined synthesis.

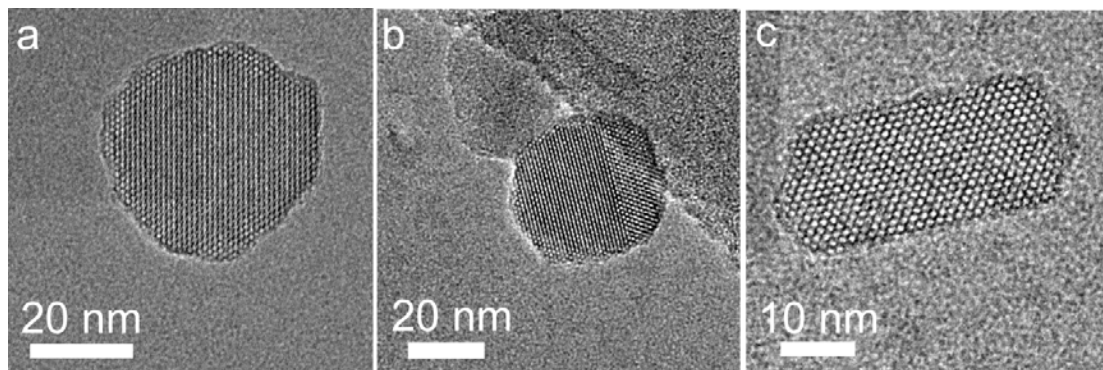


Figure B.3: TEM images showing MFI particles synthesized in 40 nm 3DOM carbon.

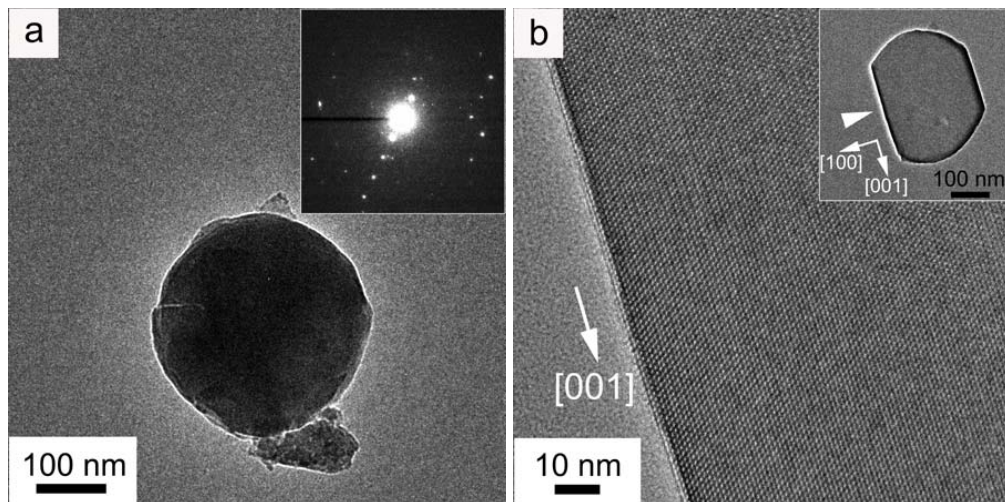


Figure B.4: (a) A spherical MFI crystal templated by one macropore. The inset shows the electron diffraction from the particle. (b) A MFI crystal showing the influence of confinement on the characteristic coffin-like MFI morphology. The a-facet marked by the arrowhead is enlarged.

<sup>§</sup>W C Yoo, S Kumar, A V McCormick, R L Penn, M Tsapatsis and A Stein, *J. Amer. Chem. Soc.*, **2009**, 131 (34), 12377

<sup>¶</sup>W C Yoo, S Kumar, Z Wang, N S Ergang, W Fan, G N Karanikulos, A V McCormick, R L Penn, M Tsapatsis and A Stein, *Angew. Chem. Int. Ed.*, **2008**, 47 (47), 9096

<sup>§</sup>W Fan, M Snyder, S Kumar, P Lee, W C Yoo, A V McCormick, R L Penn, A Stein and M Tsapatsis, *Nat. Mater.*, **2008**, 984